PROBING THE STRUCTURE OF THE PERICELLULAR MATRIX VIA NOVEL BIOPHYSICAL ASSAYS

A Dissertation
Presented to
The Academic Faculty

by

Louis T. McLane

In Partial Fulfillment
of the Requirements for the Degree
Doctor of Philosophy in the
School of Physics

Georgia Institute of Technology
December 2013

PROBING THE STRUCTURE OF THE PERICELLULAR MATRIX VIA NOVEL BIOPHYSICAL ASSAYS

Approved by:

Dr. Jennifer Curtis, Advisor
School of Physics
Georgia Institute of Technology

Dr. Paul Goldbart
School of Physics
Georgia Institute of Technology

Dr. Harold Kim
School of Physics
Georgia Institute of Technology

Dr. Alberto Fernandez-Nieves
School of Physics
Georgia Institute of Technology

Dr. Todd Sulchek
School of Mechanical Engineering
Georgia Institute of Technology

Date Approved: November 05, 2013

To Lindsay

ACKNOWLEDGEMENTS

First and foremost, I would like to thank my advisor, Jennifer Curtis, for helping me realize my dream of earning a PhD in physics. Without her none of this would be possible, and I am not sure that I know of any other scientist or person that would have put up with my idiosyncrasies as well as she did. She pushed me to be the best scientist that I could be, while also allowing me the room to learn how to become a researcher on my own. Thank you for being the ideal advisor and an even better person.

On a more personal note, I would like to thank my wife and life partner, Lindsay. Moving to Atlanta not only let me achieve my academic dreams, but also led me to find the love of my life. Graduate school would not have been nearly as manageable without your supportive presence. A man can only dream of achieving both professional and private fulfillment, but meeting you has allowed me to attain both.

I would also like to thank my classmates, labmates, teachers, and anyone else with whom I've had the pleasure of working for helping to teach me how to become a scientist, and for humbling me. Specifically I would like to thank Patrick Chang, as without him much of the work presented here would not exist. Constantly being surrounded by so many intelligent people has helped pushed me, and I would not be where I am today without them. In that vein I would also like to thank my committee members, as they played a final yet vital role in helping me step back and think about my thesis work, and how it fits in the context of science as a whole. Thank you for your guidance and input, and for exploring these subjects alongside me.

My friends, both new and old, have also been an important part of my life, and I would like to thank them for their support. Whether they knew it or not, the time I spent with them was instrumental in my development as a person.

Finally I would like to thank my family, as they have also been a great source of support. Watching my sister Anne become a lawyer has further pushed me to attain success while also keeping me grounded to who I am and where I come from. My mother has long been the rock of our small family, and her constant support and love has been essential. I would also like to thank my late father for teaching me how to be a kind and caring man. Professional achievements mean nothing if you do not have a good heart and my family and friends have instilled values in me that will last the rest of my life.

TABLE OF CONTENTS

CHAPTER

LIST OF TABLES

LIST OF FIGURES

LIST OF SYMBONS AND ABBREVIATIONS

PCM	pericellular matrix
PEA	particle exclusion assay
qPEA	quantitative particle exclusion assay
OT	optical trap
OFPA	optical force probe assay
AFM	atomic force microscope
HOT	holographic optical trap
SLM	spatial light modulator
HA	hyaluronan
RCJ-P	rat chondrocyte joint cells
GFPn	green fluorescent protein – neurocan link protein
hMSC	human mesenchymal stem cells
exg-aggrecan	exogenous aggrecan

SUMMARY

The pericellular matrix (PCM) is a voluminous polymer network adhered to and surrounding many different types of mammalian cells, and which extends out into the environment outside the cell for distances ranging up to twenty microns. It is comprised of very long flexible polymers (hyaluronan) which are tethered to the cell surface and which have binding sites for large, highly charged bottle brush proteoglycans (aggrecan). The PCM plays an important role in many cell functions such as cell proliferation, cell adhesion, cell migration, and cancer development, however the precise way it influences these processes remains unclear.

Three original biophysical tools are developed in this thesis in order to study the PCM: the quantitative particle exclusion assay (qPEA), optical force probe assay (OFPA), and exogenous fluorescent aggrecan mapping assays. These tools are used to measure the polymeric and biophysical properties of the matrix in order to make further advancements in the understanding the PCMs role in adhesion, transport to and from the cell surface, its purported function as a chemical micro-reservoir, as well as basic studies on the kinetics of its formation, turnover and maintenance.

The qPEAs measure the penetration and distribution of sub-micron particles after they diffuse into the cell coat, where their distribution maps the interior structure of the PCM. The qPEA assays reveal that the PCM acts a sieve, separating incoming particles by their size, preventing micron sized

particles from entering the PCM while allowing sub 100 nm particles to pass to the cell surface.

The OFPA uses an optically-trapped bead to study the force response of the matrix as it encounters the probe. The assay not only reveals new details about the PCM such as the fact that it is larger than initially thought, having a two layer structure, but when combined with a polymer physics model which relates the observed equilibrium forces to an existing osmotic pressure gradient within the PCM, the OFPA studies produce the first discovery and measurement of the correlation length distribution in the cell coat. The OFPA and qPEA assays are also performed on cells modified with exogenous aggrecan, resulting in a model for possible proteoglycan mediated cell coat transformations. The fluorescent exogenous aggrecan assays measure the dynamics of the exogenous aggrecan binding to and releasing from the coat, revealing that the PCM can be rapidly modified by a changing environment, and quantitatively measure how the exogenous aggrecan modifies the existing PCM. Together, these assays provide an unprecedented look into the interior structure of the PCM, and the mechanisms responsible both for this structure and its modification.

CHAPTER 1

INTRODUCTION

The pericellular matrix (PCM) lies at the nebulous interface of the extracellular matrix (ECM) and the cell surface, but unlike the ECM, the pericellular matrix is defined by its direct anchorage to the plasma membrane (3). This matrix, or cell coat, decorates the surface of a variety of cells *in vivo* and in tissue culture including fibroblasts (4), smooth muscle cells (5), prostate cancer cells (6), epithelial cells (7), chondrocytes (8), and mesothelial cells (9). Studies show that the cell coat extends outward anywhere from a few up to twenty microns (3, 10) (Figure 1.1a) depending on the cell type and cell state. The underlying scaffold of the pericellular matrix is comprised of hyaluronan (HA) (Figure 1.1b and Figure 1.2), a negatively-charged linear polysaccharide found *in situ* with contour lengths as long as 2-25 microns (11). Anchored to the cell surface via HA-binding receptors and HA synthase, hyaluronan densely assembles bottlebrush-shaped proteoglycans such as aggrecan and versican along its chain, the major constituent of the PCM. These proteoglycans are extremely large and negatively charged, with semi-rigid cylindrical geometries of ~80 x 350 nm (1) (Figure 1.3). Their attachment increases hyaluronan's persistence length dramatically (12) to form extended configurations that give rise to the cell coat (13-14).

The functions of the pericellular matrix are poorly defined but studies show that the matrix influences a diverse range of fundamental cell processes and disease states. These include cell adhesion (7, 15-18), proliferation (5, 19), migration (5, 20), embryonic development (21), wound healing (22-23), mechanotransduction (24-25), protection from viral infections (26), sequestration of growth factors (27), osteoarthritis (28), and various

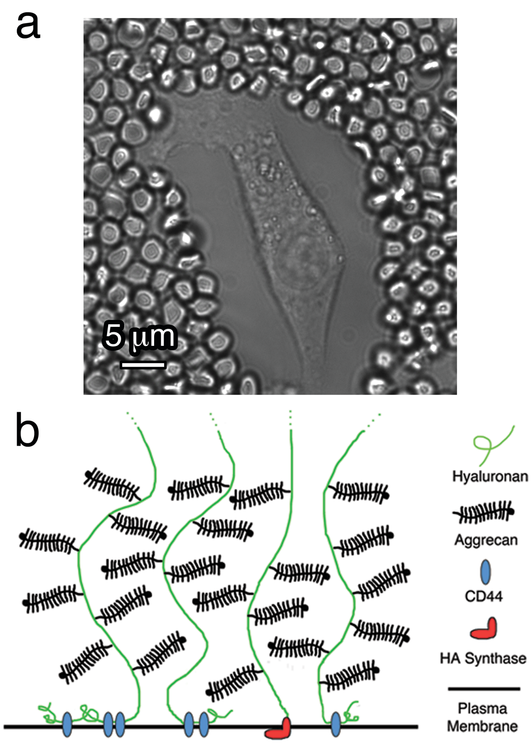

Figure 1.1 (a) Traditional particle exclusion assay of chondrocyte RCJ-P cells which uses fixed red blood cells to visualize the extent of the PCM. (b) Schematic of the pericellular matrix. Hyaluronan polymer chains decorated with proteoglycans (e.g. aggrecan) are bound to surface receptors.

forms of cancer (11, 29-32). An illustration depicting the cell coats importance for adhesion based events is shown in Figure 1.4. Recent work has also emphasized the importance of the PCM in drug delivery applications (33). Improved characterization methods are needed to clarify the mechanisms by which the pericellular matrix contributes to these cellular functions.

Traditional particle exclusion and biochemical assays of the PCM contents provide some clues, suggesting the supramolecular organization of the matrix is dynamically rearranged, especially when a cell’s adhesion to the surroundings is altered. For example during mitosis and migration, there are changes in the length of the cell coat’s constituent HA chains (20), the distribution and type of proteoglycans (15), and the

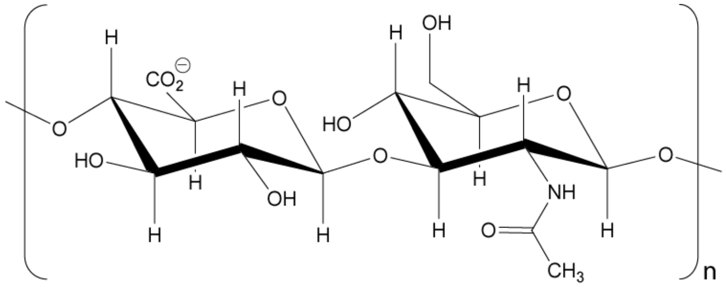

Figure 1.2 Chemical diagram of hyaluronan. Structurally, hyaluronan has a 7 nm persistence length can be formed with sizes up to 106-107 Da, which when stretched end-to-end would have a contour length of 25 um.

hyaluronan grafting density and spatial organization at the cell surface (34). In mitosis the pericellular matrix swells as the cell releases its attachments to the ECM (35). Similarly, in migrating cells, which rely on a delicate coordination of attachment and detachment of focal adhesions (36), the cell coat is reorganized into a distinct asymmetric distribution around the cell's exterior with little PCM at the leading edge and with an accumulation at the rear. Further, it has been shown that removal or reduction of the pericellular matrix significantly diminishes proliferation rates and migration speeds (5). Increasing the cell coat thickness by adding exogenous hyaluronan or proteoglycans increases the rate of migration (6, 23). Far more work is needed to explain the role of the pericellular matrix in these processes, in particular using methods capable of dynamically characterizing the state and macromolecular organization of the cell coat on living cells.

The cell coat has remained a somewhat obscure structure in part because of its invisibility to phase contrast and differential interference contrast (DIC) microscopy, and the difficulty in preparing samples for conventional histochemistry and electron microscopy without collapsing the matrix. This invisibility and fragility is due to the high water content resulting from the hydration of the highly-charged proteoglycans. Until now, the pericellular matrix's spacious swelling has most often studied using the classical

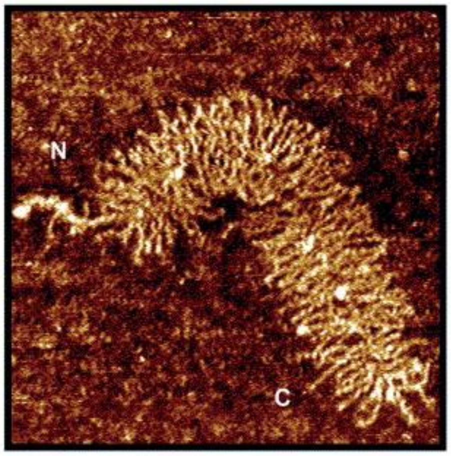

Figure 1.3 Atomic force microscope image of an aggrecan molecule. Adoped with permission from (1).

particle exclusion assay (PEA) (Figure 1.1a). In this approach, fixed red blood cells are added to the sample, where subsequent visualization of the empty space between the red blood cells and the adherent cell reveals the presence and extent of the pericellular matrix. A handful of studies have introduced strategies to characterize structural or mechanical properties of the cell coat (2, 9, 13, 37-41). Nevertheless, characterization of the ultrastructure and the physicochemical properties of this extensive cell matrix structure is still lacking.

Little is understood about the polymer physics of these supramolecular hyaluronan-proteoglycan assemblies or of their resultant collective properties when they are tethered at the cell surface (42-43). Even less is known about how they come to regulate cell function. The ability to monitor the ultrastructure of the pericellular matrix of a living single cell should help delineate the mechanistic roles of the PCM in the numerous physiological processes correlated with its presence. To meet this need, we present an optical trap based single cell measurement force assay and a novel quantitative particle exclusion assay, which together move beyond the traditional particle exclusion

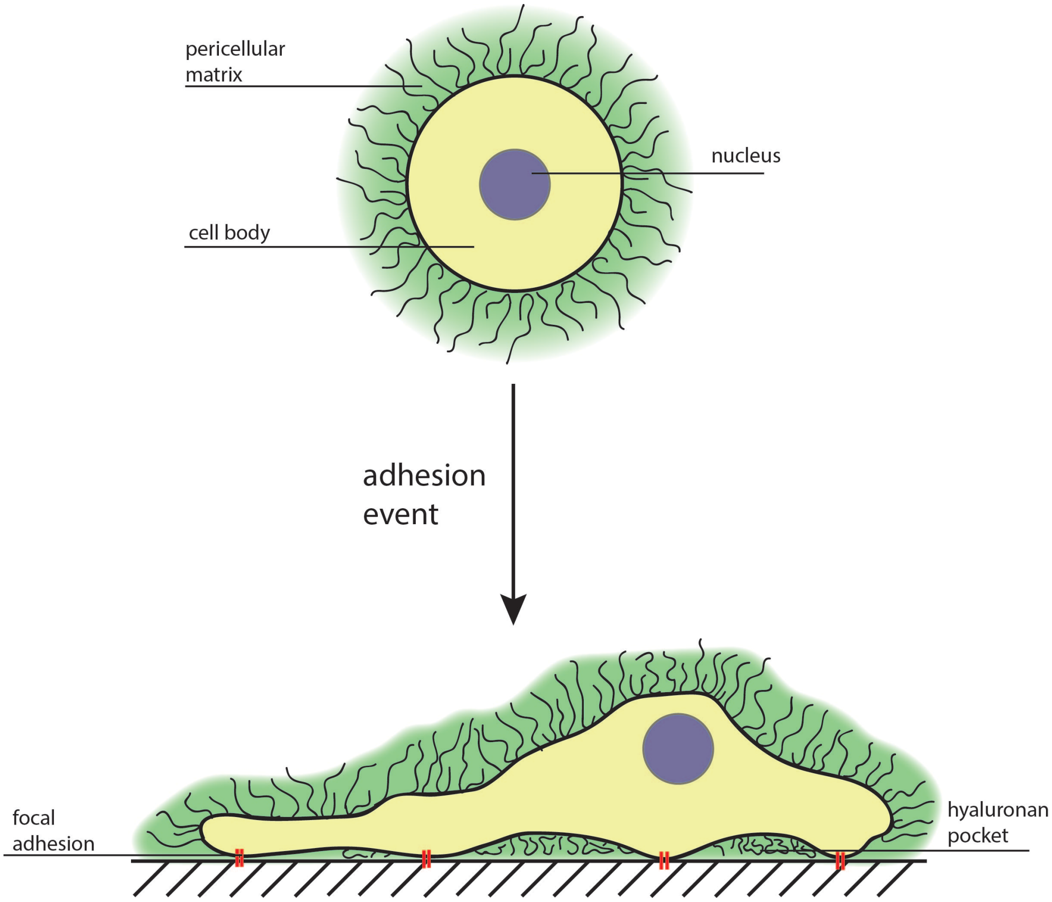

Figure 1.4 Illustration of the pericellular coat's importance during adhesion based cell processes. The cell coat surrounds many cells and has a thickness that is on the order of 10 microns large. In order for a cell to adhere to a surface it must form adhesion sites, such as focal adhesions. The PCM must rearrange to accommodate these focal adhesions, however the manner through which this occurs is completely unknown.

assay in determining the mechanics and spatial organization of the pericellular matrix. In addition, newly developed exogenous fluorescent aggrecan mapping assays are used to study the dynamics of changing coats, as treating the cell coats with fluorescent aggrecan is studied in real time. As it is difficult to label specific proteins in living cells, our development of the use of fluorescently labeled exg-aggrecan presents a technique by which we can study the real-time distribution of aggrecan in live cells.

Development of new tools is needed to study the mechanical and structural properties of the pericellular matrix, as while existing studies have greatly expanded the current understanding of the PCM and its structure, they still paint an incomplete picture of the pericellular matrix. Until recently, the primary technique used to study the PCM has been the traditional particle exclusion assay. PEAs are used in order to demonstrate the presence of the PCM, and are used to gain an estimate of the overall its size, but only give the roughest idea of how the PCM is structured. Biochemical assays have also been vital in understanding the multiple components of the PCM, yet are unable to relate the presence of these molecules to their role in creating and structuring the PCM. Recent efforts in microrheology (2, 39), strain apparatus (44-45), micropipette (28, 46), and atomic force microscopy (40-42, 47) studies have begun to move beyond the use of PEAs and biochemical studies as the main techniques used to study the PCM, and it is part of our goal to develop additional tools towards a complete understanding of the structure of the PCM and its relationship to its biological importance.

Atomic force microscopy, for example, is able to measure the total force response of the PCM, or PCM like structures, to a micron sized bead. However the AFM has a few features that are not entirely desirable for studying the structure of the PCM. Typically, an AFM is used in the nano-newton force range, and as the results in Chapter 3 will demonstrate, the PCM exerts force on a pico-newton range. To take advantage of the typical force range of the AFM, there have been studies that measured the force response of the combined PCM-chondrocyte structure (28, 40, 48). These structures are often called ‘chondrons’, and are of great interest. However our goals are to study the structure and mechanics purely of the PCM, and not the PCM when combined with the entire cell. Additionally, there is the consideration that the AFM has physical restraints, as the probe is physically attached to a cantilever on one side. Traditional AFMs are only able to measure forces that vertically displace the cantilever, and thus can only measure forces in one direction. This places a limitation for the use of an AFM on our system, as the PCM is a full three dimensional structure. Optical tweezers are used here in order study the PCM as they are both of the desirable force range, and they are able to non-invasively pass through the matrix. The ability for optical force probes to pass completely through objects will be used in the following work in understanding how the PCM responds to a penetrating particle.

Traditional passive microrheology has also been successfully applied to studying the viscoelastic properties of the PCM. Part of our goal is to expand upon these results, and to develop assays that allow us to probe aspects of the PCM that are unobtainable through preexisting techniques. Aside from tool development, our ultimate aspiration is to relate the physical measurements obtained from our techniques to the ultrastructure of the PCM, and it our belief that the assays developed and presented here will aid in this pursuit.

Our measurements establish the true perimeter of the pericellular matrix on RCJ-P cells, demonstrate its malleability and robustness, and for the first time illustrate and quantify the existence of a spatially varying mesh size throughout the cell coat. Comparative measurements of cell coats before and after their transformation by exogenous aggrecan show distinct changes in the extracted force curves, illustrating the optical force probe assay's sensitivity to proteoglycan distribution. Studying the real time modification of cell coats reveals that the coats can be changed at a rapid pace (less than ten minutes), and that the cell coat is easily penetrable by aggrecan, one of its main structural components. In addition, the fluorescent studies allow us to directly measure the concentration profile of bound exogenous aggrecan, yielding information about the way in which the aggrecan treatment specifically modifies the existing cell coat.

The remainder of this thesis is broken into five chapters. Chapter 2 discusses development and use of materials and methods introduced or referred to in the main text. Chapter 3 introduces the optical force probe assay (OFPA), discussing its development and use. The OFPA is also performed on treated and untreated cells, and when combined with scaling theory from polymer physics is able to calculate a correlation length profile through the cell coat. Chapter 4 introduces both traditional and quantitative particle exclusion assays, first on untreated PCMS, and later on cell coats which have been modified via exogenous aggrecan. Chapter 4 also includes comparison between the qPEA and OFPA results, yielding a consistent interpretation about the structure of the PCM. Chapter 5 discusses the fluorescent exogenous aggrecan experiments, and touches on possible mechanisms for the observed cell coat structural modification as well as demonstrating the usefulness of visualizing the cell coat via fluorescently labeled exogenous aggrecan. Finally, Chapter 6 concludes with a summary of results, as well as touches on the on-going and future work inspired by the assays and results presented in this thesis.

CHAPTER 2

MATERIALS AND METHODS

Methods or techniques used and developed for our studies of the pericellular matrix not described elsewhere in this manuscript are summarized here.

2.1 Cell Culture

Rat chondrocyte joint cells (RCJ-P, fetal calvaria, batch 15.01.98; Prochon Biotech, Rehovot, Israel) were cultured under 5% CO_2 with α-MEM, 15% FBS, 2% L-glutamine (Mediatech, Manassas, VA). The cells were plated for 18-24 hours at low density on 78.5 mm^2 ($6x10^4$ cells), and measured during passages 15-35. During optical force probe assays, a stage-top microscope incubator (LiveCell^{TM}, Pathology Devices, Inc., Westminster MD) maintained the cells at 37^o, 5% CO_2, 80% humidity in order to keep the cells viable for long-term experiments. Quantitative particle exclusion assays are held at 37^0 C and 5% CO_2 with a different stage-top incubator (N. E-MSI 07-3156, Okolab, Ottaviano, NA, Italy). The sample holder used for experimentation is made of nonstick Teflon and has a small well in the bottom that is covered with a glass coverslip (Figure 2.1). The size of this well, d, can be changed in order to add different sample volumes. To minimize volumes used, the typical well can hold a volume of 200 µl, where the well for exogenous aggrecan holds 100 µl. The media shown here is red, as we culture with phenol red, which is a sensitive pH indicator. After assembly the sample holders are exposed to a UV light on each side in order to insure sterility.

For production of neurocan-GFP. human embryonic kidney (HEK) cells were cultured in order to collect the media. HEK were cultured with a 1:1

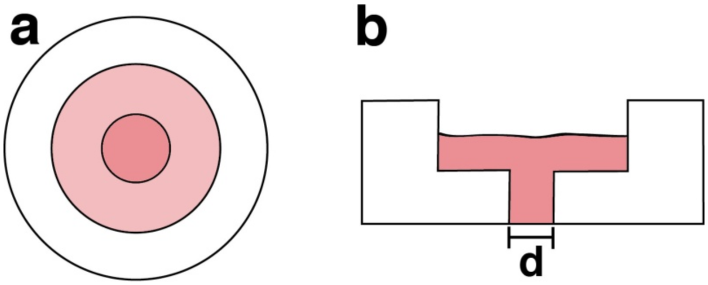

Figure 2.1 Schematic of custom sample holder from (a) top down and (b) side cross sectional side view.

mixed D-MEM/F12 (Mediatech), 10% FBS, 1% L-glutamine (Mediatech) and 0.01% puromycin solution (10mg/ml, Sigma). Puromycin was added after the first passage, as puromycin can be toxic to recently thawed cells.

2.2. Pericellular matrix modification via exogenous aggrecan

Exogenous aggrecan (exg-aggrecan) is purchased (Sigma-Aldrich) in powder form and stored at -20 ^{o}C. The aggrecan was then diluted in PBS at 2 mg/ml, and allowed to dissolve for at least an hour before use. To minimize the effect of bulk diffusion in the experiments where exg-aggrecan is used to swell the pericellular matrix the aggrecan is premixed before it is added to the sample. Premixing is achieved by combining a small quantity of the exg-aggrecan solution with premade cell media in order to achieve the desired final exg-aggrecan concentration. For the experiments shown here the exg-aggrecan was typically used at a range of values up to 333 μg/ml, and a total volume of 100 μl of the solution was used with the smaller sample holders.

For experiments, cells were plated in the sample holders for 18-24 hours before exposure to aggrecan. The cell media is then carefully removed with a micropipette, slowly enough not to destroy or disrupt the pericellular matrix. The aggrecan solution is then quickly added to the sample and allowed to incubate for 2 hours (unless otherwise noted). The exg-aggrecan solution is then removed and replaced with clean media in order to eliminate the effect background aggrecan concentration in the experimental results.

2.3 Fluorescent labeling of exogenous aggrecan

To study the dynamics of how exg-aggrecan modifies the cell coat, the exg-aggrecan is labeled with a fluorescent dye to study precisely where the exogenous aggrecan binds within the coat. 488 nm NHS (***N***-Hydroxysuccinimide) ester dyes (Sigma) were used to fluorescently label the exg-aggrecan. NHS esters are highly reactive and form bonds with amine groups, which are abundant in many proteins through their amino acids (particularly lysine). Here we incubate the NHS dye with exg-aggrecan for 1 hour in order to let the NHS groups bind to the available amine groups in the protein backbone of the aggrecan. With both the protein and NHS dye at the same concentration (2 mg/ml) the protein is stained at a 100:2 protein to dye ratio. After 1 hour of incubation, the excess dye is removed with a Zeba Desalting Column (Thermo) to replace the dye solution to that of pure PBS. The dyed aggrecan is then stored at 4 ^{o}C for up to one month. For experimentation, the fluorescently labeled dye is added to the samples in exactly the same manner as Chapter 2.2.

2.4 GFPn production and use

Rauch et al. (49) designed a cDNA strand that encodes for a protein where a green fluorescent protein (GFP) molecule is connected to a neurocan link protein (49-50).

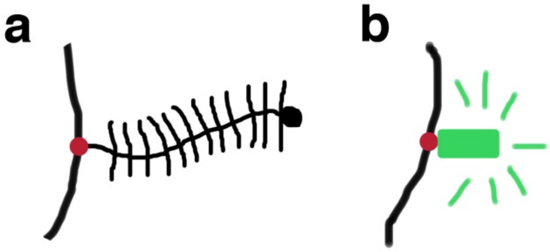

Figure 2.2 Schematic of the GFPn molecule. (a) A typical proteoglycan is shown binding to a hyaluronan strand, where its binding domain is highlighted in red. (b) Shows the GFPn molecule, where the link domain from neurocan is connected to a GFP molecule. Sizes shown are not to scale in order to be able to visualize the key components.

Neurocan is a proteoglycan similar to the aggrecan in our system, which has a similar structure where the first domain of the backbone is the link that binds specifically to hyaluronan. The resulting protein (called here GFPn) specifically labels hyaluronan with GFP, resulting in the ability to fluorescently image the cell coat (Figure 2.2). This plasmid was transected into HEK cells in order to produce the GFPn molecule. HEK cells were gifted by U. Rauch (Uppsala University, Uppsala, Sweden), and are cultured in conditions as outlined above.

After transfection, the HEK cells translate the cDNA into the GFPn molecule via the typical protein production cell machinery, and the GFPn is then released into the cell media. For GFPn production, the transfected HEK cells are plated into five 175 cm^2 flasks and allowed to reach confluency (~ 4 days). The media is then removed and replaced with FBS free media. Every 2 days the media is collected and replaced again with FBS free media. The collected media is a solution of media, dead cells, and molecules excreted by the cells, including the desired GFPn. The collected media is centrifuged at 2000 rpm for 20 minutes in order to separate the dead cells and large debris from the media. The supernatant is then removed and treated with protease inhibitor

(Thermo Scientific). This procedure is repeated for 2-3 collections, as after this point the cells no longer produce measurable GFPn. If more GFPn is required, another set of 5 flasks must be plated and the process restarted.

After the desired quantity of collected media is taken, it is then centrifuge filtered (Millipore Amicon Ultra: 15-30 k) which collects any molecules larger than 15-30 kDA and lets those smaller pass through the filter. After initial filtration, typically 20% of the total initial volume remains. The remaining media (which contains the GFPn molecule) is then filtered again, this time with a his-tagged protein purification column (Pierce, HisPur Cobalt). In short, these columns have a resin that has a high affinity for his-tagged proteins, which was included in the design of the GFPn. The remaining media is filtered through this column 400 μl at a time. Any non his-tagged proteins and media easily pass through the resin and column, leaving only the GFPn remaining. The column is then eluted with a buffer (as directed by the product sheet), which releases the GFPn from the resin, and is collected with a 200 μl volume of elution buffer. Releasing the GFPn with the elution buffer is performed twice as the first pass is not 100% efficient, resulting in two collections. The fluorescence signal of the GFPn solution is then checked with a UV Vis machine, in order to verify collection and to quantify the amount of protein.

In order for cell treatment, the GFPn solution is then run through a buffer exchange column (Thermo Zeba desalting) in order to suspend the GFPn in PBS. The elution buffer, while required for releasing the GFPn from the resin column, is not the correct pH or salt density for cell treatment. The buffer exchange protocol requires the desired buffer to be run through a column multiple times, followed by a run with the

GFPn media. This results in a GFPn solution in PBS and is now ready for cell experimentation.

In a technique matching that of the addition of exogenous aggrecan, GFPn is added to the samples by first mixing the GFPn solution with pre-warmed media, to achieve the desired concentration. Unless otherwise noted, 20 ul of the GFPn is mixed with 100 ul of media before it is added to the cell sample. The GFPn solution is then allowed to incubate with the cells for 2 hours in order to let the molecules fully incorporate themselves within the cell coat.

2.5 Microscopy

For optical tweezer and epi-fluorescence studies, samples were imaged in bright field using a Nikon TE-2000 microscope. The microscope was equipped with a high-speed camera for the optical force probe assays (Phantom v7.1, Vision Research, Wayne, New Jersey), and a Nikon DQC-FS camera (Nikon, Melvillem, NY) for epi-fluorescence imaging of the PCM. A Nikon 60X 1.4 NA was used for optical trapping, as well as traditional particle exclusion assay imaging. The optical trapping configuration used standard bright field microscopy, while the particle exclusion assays are done in DIC microscopy in order to better visualize the cell edge. A full schematic of the experimental setup is shown in Figure 4.2, including the microscopy path. All live cell imaging is performed with a stage top cell incubator (see Chapter 2.1) as this keeps the cells at physiological conditions for viability. For long term imaging (Chapter 5.1) the bright field lamp is turned off between imaging to prevent light damage to the cells.

Confocal microscopy was performed with an Olympus Fluoview FV1000 and an Olympus 60X objective. A portable stage-top incubator (Okolabs) was used to control the temperate and carbon dioxide conditions of the sample on the microscope stage. The microscope and incubator was turned on at least an hour before imaging in order to allow the system to stabilize, and to minimize drift. For most fluorescent studies the 488 laser was to image both our GFPn and fluorescently labeled aggrecan. Typical microscope settings using the 488 nm laser are 4% power, resolution of 12 bits/pixel, sampling speed of 4 us/pixel, and PMT voltage approximately 600 V. After adjusting the setting of the microscope for the dye in sample, imaging location was set at 3 μm above the glass slide in order to image the cell coats at a height similar to that used in the optical force probe studies.

For imaging, the fluorescent aggrecan is removed after incubation and is replaced with normal cell media for imaging. We have found that leaving the fluorescent aggrecan in solution makes it difficult to visualize the PCM with sufficient contrast. The sample is rinsed in order to remove any possible background signal from unbound exogenous aggrecan that arises due to the sudden change in chemical equilibrium associated with the change in the solution concentration of aggrecan.

CHAPTER 3

OPTICAL TWEEZER FORCE MEASUREMENTS OF THE PERICELLULAR MATRIX

Due to their versatility, precision, non-invasiveness, and ability to measure piconewton forces, optical tweezers have become a common device in the toolbox of the modern biophysicist. Here we take advantage of these features in order to probe the force response, and ultimately with the help of modeling, the structure of the pericellular matrix of mammalian cells. Optical tweezers are an ideal tool to study this extremely soft surface-bound polymer matrix, as other techniques are either not sensitive enough or are unable to probe the PCM without simultaneously probing the mechanics of the cell body. The optical force probe assay (OFPA) developed below probes the dynamic forces exerted by the cell coat on a moving bead as well as the equilibrium forces on a bead at rest inside the cell coat. These forces, and in particular the equilibrium force, are used to develop a model of the PCM, calculating for the first time a correlation length, or characteristic length scale, profile throughout the PCM.

3.1 Methodology

3.1.1 Traditional optical tweezers

First discovered by Arthur Ashkin and Steven Chu (51), optical tweezers use a highly focused laser beam to trap micron-sized particles with forces up to a few hundred piconewtons. To achieve stable trapping, the laser beam is tightly focused with a high numerical aperture objective lens. When a dielectric particle encounters the focus of the laser beam, it will scatter and diffract the light. If the particle has a dielectric constant

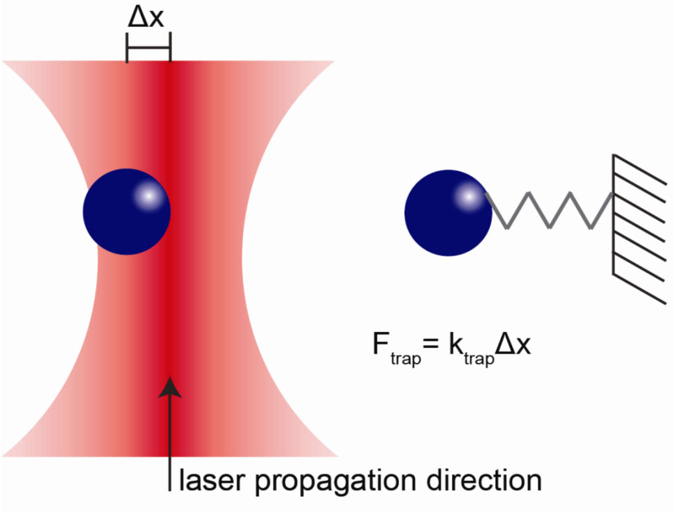

Figure 3.1 Schematic of an optical trap system. A dielectric particle trapped in a highly focused laser beam behaves analogously to a system of the particle attached to a spring.

larger than that of the surrounding media, the refraction of the light will be such that the force back on the particle (by conservation of momentum) will draw it towards the focus of the laser. This force is thus referred to as the gradient force, as it draws the particle in towards the point of highest gradient. In addition, the particle is pushed ‘downstream’ from the focus as it scatters some of the light back towards its origin. However in a stable optical trap this scattering force is countered by a larger gradient force, resulting in the particle only being slightly downstream from the focus but trapped both laterally and axially.

While the ability to trap and manipulate micron sized particles is an extremely powerful technique, we are primarily interested in the ability of optical tweezers to act as a precise force probe. For non-large displacements of the particle, the gradient force on the particle when it is pushed out of the center of the trap is linear with the displacement from the center of the trap. Thus for small displacements the optical trap behaves exactly as if it were a spring, where the trap has some stiffness, k_{trap}. This analogy is depicted in

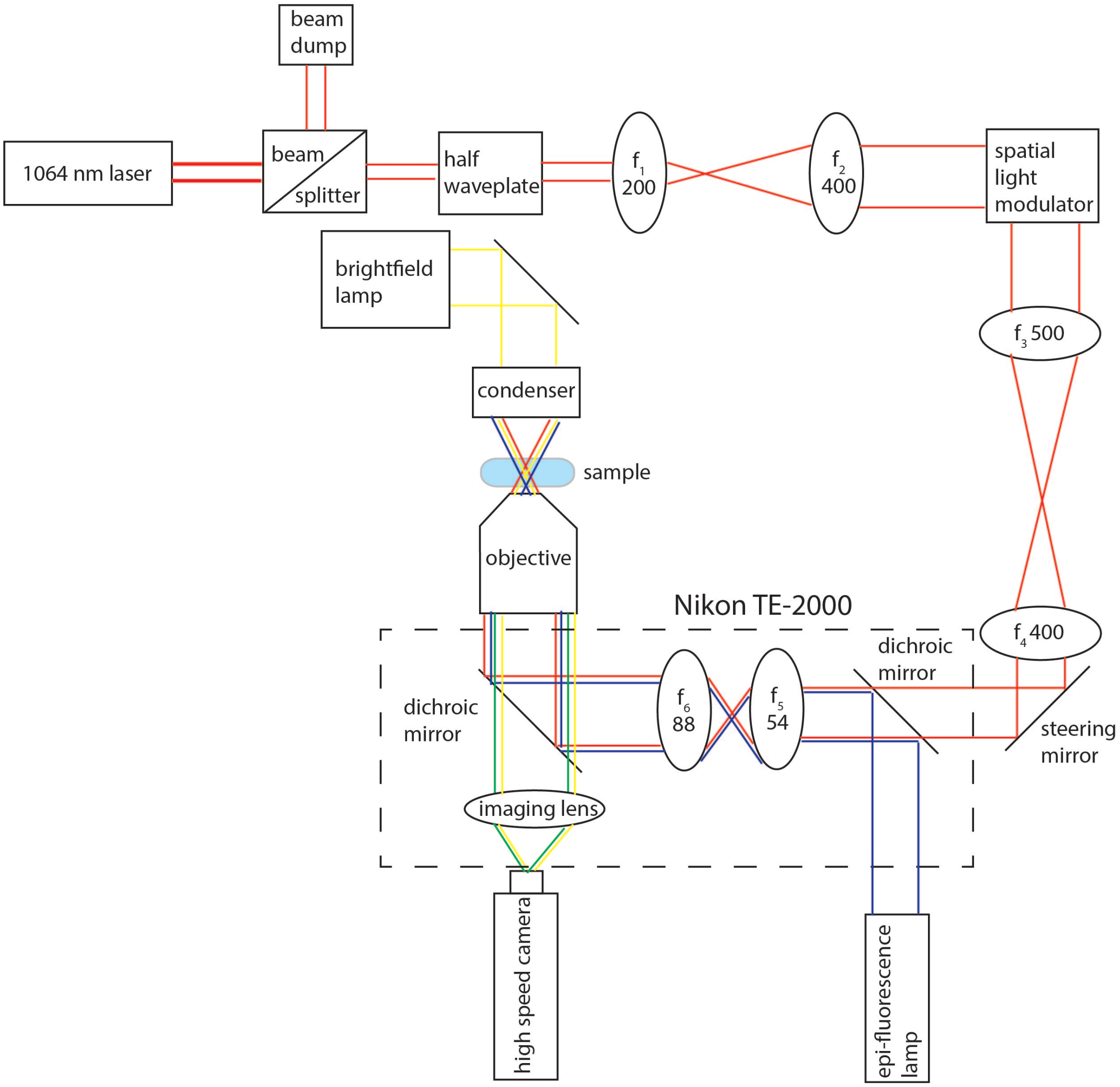

Figure 3.2 Schematic of the experimental system. 1064 nm IR laser (red), bright field transmission (yellow), epi-fluorescence (blue), and fluorescent emission (green) light is shown.

Figure 3.1. When in equilibrium, there is no net force on the particle when it is trapped, and thus the trapping force exactly balances the force from any external source. Once the trap stiffness is calibrated, the position of the particle is used as a direct measurement of the forces on that particle.

A full diagram of the system used for this thesis work is shown in Figure 3.2. Optical trapping was achieved with a 1064 nm laser (YLR-10-1064-LP, IPG, Oxford, MA). A pair of Keplerian relay telescopes, combined with steering mirrors, were used to deliver the beam (280 mW) to the back aperture of the microscope objective (60x, 1.4NA oil, Nikon, Melville, NY). A dichroic mirror coupled the beam into the microscope, enabling simultaneous imaging and trapping. Samples were imaged with bright field microscopy using a Nikon TE-2000 microscope equipped with a high-speed camera (Phantom v7.1, Vision Research, Wayne, New Jersey), or with fluorescence microscopy using a Nikon DQC-FS camera (Nikon, Melvillem, NY). Movies were taken at 500 fps during optical force probe assays and 2000 fps for calibration.

Optical traps, both conventional and holographic, were calibrated by evaluating the probability distribution of a trapped particle in the trap (52). The equipartition theorem states that for a particle in a harmonic well (such as the optical tweezer)

$$U(x) = \frac{1}{2} k_{trap} \langle \Delta x^2 \rangle = \frac{1}{2} k_B T. \qquad \text{Eq. 3.1}$$

Thus we can then define the probability distribution of the trapped particle as

$$P(x) \propto exp\left(\frac{-U(x)}{k_B T}\right) = \exp\left(\frac{-k_{trap}\Delta x^2}{2k_B T}\right). \qquad \text{Eq 3.2}$$

For a harmonic potential, this distribution is then a Gaussian. A non-linear least squares method was used to fit a Gaussian to the position histogram, and yields a value for the trap stiffness k_{trap} (typically ~50 pN/μm). It was verified that the optical trap is linear for the range of relevant forces using Stokes drag measurements.

Optical force probe assays were achieved using a static calibrated optical trap (OT) and a programmable stage (Prior ProScan H117, Rockland, MA). In a typical experiment, an OT holding a 3 μm probe was positioned approximately 20-30 μm from the edge of the cell surface, where it could be translated towards and away (orthogonally) to the cell surface at 8 μm/s. The optical trap was halted for 5 seconds at the edge of the cell (at least 3 μm from the membrane) and outside of the matrix. Forces on the probe were extracted by using a standard sub-pixel particle tracking algorithm (53) to find the bead displacement in the OT and hence the force. Bead height above coverslip was ~5 μm. For all data shown here error bars represent twice the standard error (or approximately the 95% confidence interval).

3.1.2 Holographic optical tweezers

Holographic optical trapping was implemented by replacing the first of the two mirrors with a reflective phase-only liquid crystal spatial light modulator (SLM, HoloEye HEO 1080P, Carlsbad, CA). The two holographic optical traps were created using kinoforms displayed on the SLM, which were calculated using a direct search optimization (54). During holographic trapping experiments, beads are moved into the PCM in 0.25 μm steps via a sequence of pre-calculated kinoforms. The average update

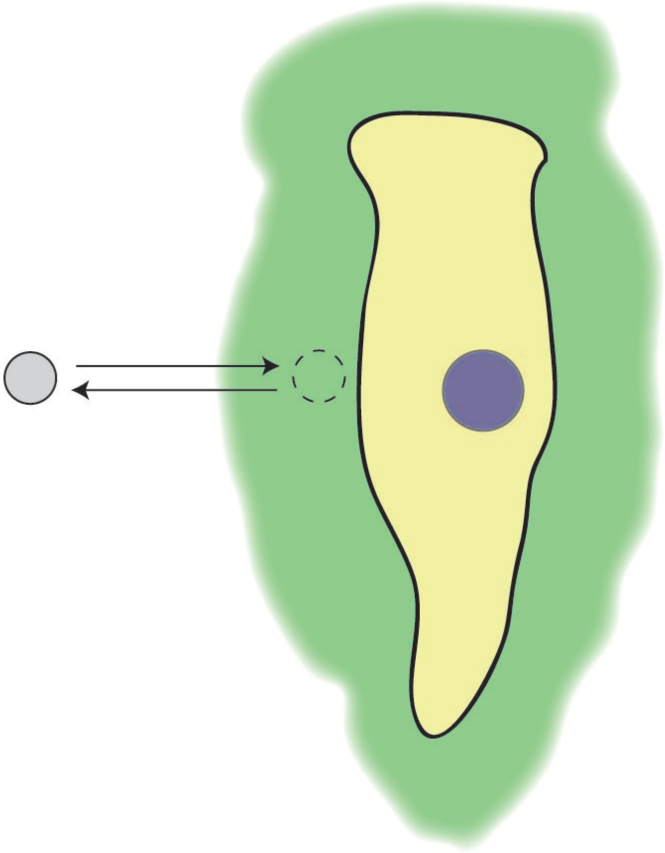

Figure 3.3 Top-down schematic of a typical optical tweezer force experiment. The 3 μm bead (grey) is trapped outside the coat (green) and then moves towards the cell (yellow) at a constant speed, and stops inside the coat before it reaches the cell membrane. The bead then reverses direction and heads back outward to its original position.

time between kinoforms is 0.07 s. The forces on the beads were calculated at each position by subtracting the theoretical position of the bead in a force free environment from its measured position (55). The stiffness of each trap is approximated to be constant with respect to different kinoforms, an assumption that we verified for distances shorter than 30 μm. Further discussion of extracting forces from the HOT measurements is found in Appendix B.

3.2 Results and discussion

The optical force probe assay introduced in this work investigates the dynamic and equilibrium properties of the pericellular matrix. A schematic of this assay is shown in Figure 3.3, while data from a typical assay is shown in Figure 3.4a. In stage I, a pegylated microsphere (described in Chapter 4.1.3) is carried orthogonally towards the cell surface at a fixed speed. The force on the probe increases once the edge of the pericellular matrix is encountered. At a distance a few microns from the cell surface to the bead, the movement is paused. This distance is maintained in order to avoid contact and possible tethering to the cell surface (56), which is often decorated by microvilli, in particular on cells with hyaluronan-rich cell coats (57). During this pause, as shown in stage II, the force on the probe decays due to rearrangement of the pericellular matrix around the microsphere. Remarkably, even after full matrix relaxation, a non-zero equilibrium force remains on the halted probe particle. The bead is then moved away from the cell surface, during which its deflection in the optical trap reveals a decreasing dynamic force (stage III). Outside of the pericellular matrix, at the original starting location, a pause is taken to allow possible matrix entanglement with the bead to relax (stage IV) before the assay is repeated.

The large pericellular matrix of rat chondrocyte cell line (RCJ-P) makes them ideal for refining the optical force probe assay measurements. Traditional particle exclusion assays shows the average thickness of these cells' PCM is $L_{o,PEA}$ = 7.0+/-0.5 μm (N=114 cells). The optical force studies should be optimized for specific cell types and possibly for changes in cell state, such as during the cell cycle. In the work reported here, the probe diameter is three microns, the probe speed is eight microns per second, and the duration of pauses inside and outside of the PCM is five seconds.

The optical force probe measurements typically yield a smooth force profile (stage I), indicating no detectable disruption of a network structure in the PCM even when recording at high frame rates (500 Hz). A sub-fraction of experiments (~10%) resulted in jagged force profiles, with apparent snapping events. These data corresponded with clear evidence of poor probe passivation (e.g., particles sticking to the sample substrate), and were not included in the final analyses. Comparison of the force profiles from consecutive measurements of the same cell reveals no change in the force signature (Figure 3.4b). This result was consistent for the more than fifty measurements made. The unchanged, smooth force profile suggests that the optical force probe assay is non-destructive, leaving the structure of the pericellular coat intact and undisturbed. The reproducibility also indicates that on these short experimental time scales (< 60 seconds), no transformation due to an active cell response is apparent.

3.2.1 Dynamic optical force probe measurements

The dynamic measurement made during the optical force probe studies (Figure 3.4a, stage I) is far more sensitive to the pericellular coat's extent than the traditional

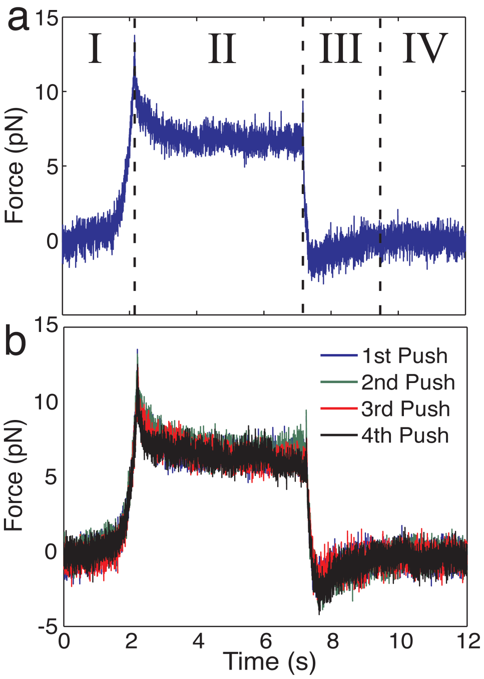

Figure 3.4 (a) A typical force curve from the optical force probe assay with the four stages of movement labeled as described in the text. (b) Comparison of consecutive optical force probe assays reveals no significant alteration in the force curves.

particle exclusion assays (PEA) used by researchers who study the PCM. Unlike traditional PEAs, which give the average position of red blood cells sitting in equilibrium with the pericellular matrix, the translating bead in the optical trap experiences a force arising from a combination of elastic and viscous components. The inset in Figure 3.5a illustrates how the sign of their relative contributions depends on the direction of motion. This observation explains in part, why the magnitude and spatial variation of the force depends on the direction of the motion. Figure 3.5a compares the inward and outward dynamic force curves acquired from the same cell. During the inward motion, the viscous and elastic forces are complementary, working together to push the optically-trapped bead away from the cell surface. During the reverse motion, the elastic force maintains the same directionality, while the viscous component reverses direction, reducing the overall force.

The inward dynamic measurements indicate that the pericellular matrix extends to distances much farther than normally appreciated (Figure 3.5a). The average distance at which a non-zero force is discernible on a 3 μm bead moving towards the cell surface is $L_{o,dyn}$ =11.5+/-1.1 μm, where the data is averaged from measurements of N=30 cells (see Table 2.1) and the subscript 'dyn' refers to the ingoing dynamic force measurement. The detectable width of the coat, $L_{o,dyn}$, is approximated by observing the location where the smoothed dynamic curve (20 point moving average) surpasses 0.5 pN, the noise level in the system. $L_{o,dyn}$ is nearly 40% larger than can be discerned with either a traditional particle exclusion assay, which yields an effective thickness of $L_{o,PEA}$ = 7.0+/-0.5 (N=114), or fluorescent staining with neurocan-GFP, which for RCJ-P cells, as we previously reported falls off exponentially so that it is barely visible beyond six microns from the surface (2). Interestingly, the range of the standard deviation of both $L_{o,dyn}$ and $L_{o,PEA}$ is similar reflecting consistency in our observation of a sizable heterogeneity in the cells' pericellular matrices.

Analysis of the dynamic force curve averaged from single cell measurements (v=8 μm/s, N=30) shows that the inward force increases towards the cell surface with an exponential dependence, F_{dyn}~exp(-bz), but where that dependence has two unique values in the cell coat (Figure 3.5b). For the outer regime of the coat, in the range 6 μm to 9 μm, the value is b= 0.35 +/- 0.07 μm^{-1}. In the inner region where measurements take place from 3 μm to 6 μm, the force increases more rapidly with b=0.42 +/- 0.04 μm^{-1}. Due to the naturally limited extent of the pericellular matrix, the fitting range is small; however,

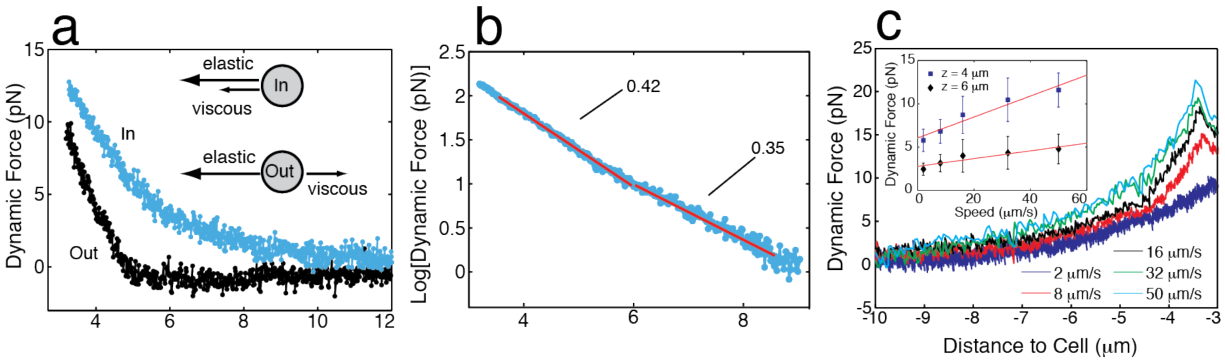

Figure 3.5 (a) Dynamic force curves measured from a single cell's pericellular matrix. The blue force curve represents the force on the bead as it moves inwards towards the cell surface (stage I). The black force curve is the dynamic force upon retraction (stage III). The difference in the value at a position z=3 μm arises from the time decay to the equilibrium force. Inset illustrates the direction of the elastic and viscous forces on a translating bead. (b) Semi-log plot of the average inward dynamic curve. Two distinct regions appear, each well fit by an exponential. (c) Investigation of the speed dependence of the dynamic force curves. The inset shows that the force is roughly linear with speed at the distances z=4 μm, 6 μm from the cell surface.

two separate exponentials were used in lieu of a single exponential, b=0.39 +/- 0.04 μm^{-1}, because the two exponentials provide a better fit to the data according to chi-square analysis. A separate analysis shows that the outward dynamic force is a single exponential that decays more rapidly with b=1.7 +/-0.1 μm^{-1} in the range 3 μm< z < 5 μm (although a fraction N=9/30 of the data was not fit well by any curve). Beyond 5 μm the outward dynamic force is negligible, likely due to the competition of elastic and viscous forces.

Next we investigated how changing the probe speed alters the dynamic response of the pericellular coat. In these measurements, the same cell was probed consecutively at five different speeds v=2, 8, 16, 32, 50 μm/s (N=7). We observed that the dynamic force relaxed to the same equilibrium value independent of the speed used during the probe. This suggests that probing at higher speeds does not damage or alter the cell coat, and justifies analysis of the scaling of the five speeds. Predictably, the higher-speed probes encounter more resistance as they are moved through the coat, as shown in Figure 3.5c. The inset in Figure 3.5c shows the variation in force with speed at two fixed positions in the cell coat (z=4 μm, 6 μm). Interestingly, the force is approximately linear with speed at both positions, and the drag on the bead, indicated by the slopes of the inset lines, is higher closer to the cell surface. While these dynamic experiments reveal interesting phenomenological measurements of the PCM, they are somewhat tricky to analyze given the lack of theoretical framework that matches the experimental procedure and results. However, the forces on the bead after relaxation inside the coat are able to be analyzed using theoretical framework, and are explored below.

3.2.2 Equilibrium optical force probe measurements

During probing, the PCM relaxes around a probe particle after it is translated into the matrix and stopped near the cell surface (region III, Figure 3.3). The typical relaxation time is on the order of ~300 ms. During relaxation, the dynamic force decays to an equilibrium force F_{eq} which is sufficient to eject the bead out of the PCM when the optical trap is turned off. F_{eq} is measured by averaging the last one second of data when the bead is paused inside the cell (out of a total of 5 seconds of pause). We investigated whether the equilibrium force persists at other locations throughout the pericellular matrix. To do this, the full optical force probe assay (stages I-IV) was repeated sequentially with the final position varying by steps of 0.3 μm. The equilibrium force is detectable in a range less than that of the dynamic force, where a typical equilibrium force curve from a single cell is shown in Figure 3.6a. Only the inner regions of the pericellular matrix, at distances less than $z<8$ μm exert a static equilibrium force on the probe particle. The equilibrium force data are reliably fit by a single exponential profile,

$$F_{eq}(z) = ae^{-cz} \qquad \text{Eq. 3.3}$$

where $c=0.50$ +/- 0.04 μm^{-1} and $a=27.3$ +/- 6.4 pN. From the fits ($N=30$), we determined the average distance at which we can detect the equilibrium force with an optical force probe assay to be $L_{o,eq}=8.0$+/-0.6 μm. The difference between $L_{0,dyn}$ and $L_{0,eq}$ of several microns (~3.5 μm) is expected given the absence of viscous forces for these stationary measurements. Interestingly, the observation that $L_{o,eq} > L_{o,PEA}$ provides evidence that the densely arranged erythrocytes used in the particle exclusion assays may exert an osmotic pressure that compresses the pericellular matrix. This result reinforces the observation that equilibrium measurements, including the traditional particle exclusion assay and passive microrheology (2, 39), are less sensitive to the full extent of the pericellular coat than dynamic measurements.

We determine, by process of elimination, that the equilibrium force in the PCM predominately arises from osmotic effects. Other possible sources for the observed force such as elastic compression of the PCM or binding to the matrix are unlikely given our reported experimental observations which indicate these effects are negligible (see section 4.2.3). However, a probe particle will experience an osmotic force if the osmotic pressure is unequal throughout the matrix, creating a pressure gradient across the particle probe. We show in a derivation (see Appendix A) that the approximate force on a bead of radius R generated by a pressure gradient is

$$\vec{F}_{osm}(z) = \frac{4}{3}\pi R^3 \frac{\partial P(z)}{\partial z}\hat{z} \qquad \text{Eq. 3.4}$$

where R is the bead radius, P is the pressure, and z is the perpendicular distance to the cell surface from the center of the bead (see Figure A.3). We hypothesize that molecular concentration gradients in the PCM give rise to the measured force, since osmotic pressure is linearly proportional to concentration. A spatially varying concentration in the PCM will arise from natural variations in hyaluronan length as well as the non-uniform decoration by proteoglycans of the hyaluronan strands (our comparative studies with exogenous aggrecan support this picture). Additionally, the basic physics of polymers bound to a surface dictates a varying concentration perpendicular to the attachment plane. Even for a monodisperse uniform layer of densely grafted polymer strands to a surface (a polymer brush), the concentration is predicted to decrease parabolically for linear neutral polymers in a good solvent (58). Similar theoretical approaches have been used to predict the spatial variation in concentration for different configurations of surface-bound polymers (59). We therefore surmise that large probe particles which penetrate (rather than compress) the PCM experience an inherent molecular gradient partially due to the configuration of the hyaluronan-proteoglycan strands as well as due to a non-uniform distribution of proteoglycans, molecules whose size and minimal spacing are one to two orders of magnitude smaller than that of the microsphere probe.

We can estimate the correlation length of the pericellular matrix, if the equilibrium force arises predominately from natural concentration variations in the PCM. The correlation length, more loosely defined as the mesh size of a polymer network, is a

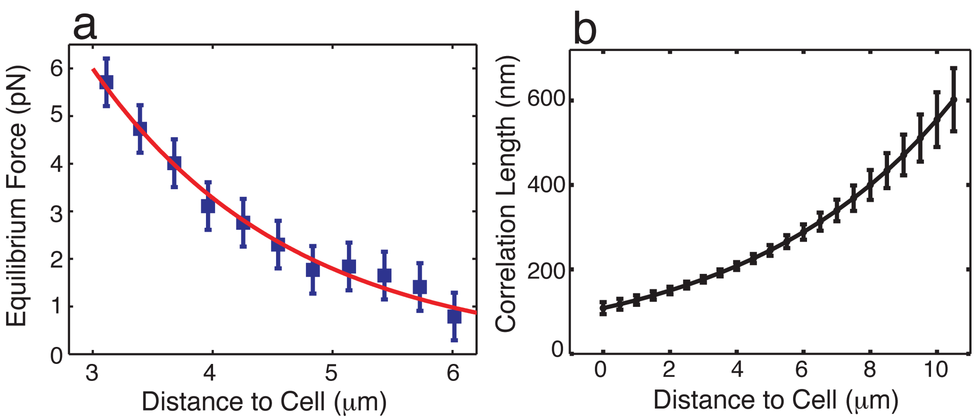

Figure 3.6 (a) The pericellular matrix exerts an exponentially varying equilibrium force on optically-trapped stationary beads. (b) The correlation length, or mesh size, in the pericellular matrix increases exponentially away from the cell surface (the prefactor is set to one).

statistical measure of the distance between segments on neighboring chains (60). Never before, to the best of our knowledge, has the magnitude and variation of the correlation length throughout the pericellular matrix been reported, and it should provide useful insight into the role of the PCM in mediating transport and the interactions of the cell with its surrounding environment.

To find the correlation length, ξ, we employ a useful result from polymer physics that gives the dependence of the osmotic pressure on the correlation length as $P \sim k_B T/\xi^3$ where k_b is the Boltzmann constant and T is the temperature (60). Our calculation of the osmotic pressure from the measured equilibrium force (see Appendix A and Figures A.3, A.4) shows that the pressure increases exponentially towards the cell surface and peaks at a value of a few Pascals:

$$P(z) = \frac{3a}{4\pi R^3 c} e^{-cz} \qquad \text{Eq. 3.5}$$

where a and c are the fitting parameters from Eq. 3.3. Equipped with this experimental result, we can estimate the correlation length up to a pre-factor of order unity and find that it is equal to

$$\xi(z) \propto e^{\frac{cz}{3}} \qquad \text{Eq. 3.5}$$

where c is the exponent from the fit to the equilibrium force curve. Figure 3.6b plots the outcome of this analysis, the mesh size prediction calculated from 30 independent cell measurements. Strikingly, the results indicate that the correlation length varies throughout the matrix, decreasing exponentially toward the cell surface, with a typical size on the scale of ~100 nm (assuming the prefactor is one). This value is consistent with the dimensions of the proteoglycans in the pericellular matrix such as aggrecan (~80 x 350 nm), whose size and distribution along the hyaluronan are likely to impact the minimum mesh size.

Examining the result in Eq. 3.5, the pressure can be rewritten as a function of the equilibrium force:

$$P(z) \propto \frac{a}{cR^3} e^{-cz} = \frac{1}{cR^3} F(z). \qquad \text{Eq. 3.7}$$

Then considering the relationship between pressure and correlation length, the latter can also be written as a function of the equilibrium force:

$$P(z) \propto \frac{k_B T}{\xi^3(z)} = \frac{1}{cR^3} F(z). \qquad \text{Eq. 3.8}$$

The correlation length is a property of the polymer network that is being measured, and should be independent of the measurement parameters. Thus examining Eq. 3.8 the correlation length should be independent of the bead size used for this probe. Alternatively, $F(z)/R^3$ should be independent of bead radius. This is indeed the case for our system, and is shown in Figure 3.7.

3.2.3 Holographic optical force probe measurements

The interaction of the probe particle with the PCM is critical in order to establish a model for the quantitative analysis of the force curves. Several complementary experiments provided evidence that the probe particle penetrates the pericellular matrix rather than compressing it. In one study, we combined imaging of the fluorescently labeled PCM (using neurocan-GFP which binds to hyaluronan) with optical manipulation of a probe bead into the matrix. We observed no deformation of the PCM as particles are moved towards and away from the cell surface (Figure 3.8). Rather it appears that the bead penetrates the PCM with the matrix recovering around the bead.

To test the validity of this qualitative observation, we examined the recovery of the PCM behind a probe bead using two holographic optical traps (see inset in Figure 3.9). To do this, we measured the force on a single bead translated to the cell surface with a holographic trap (55). Then the same bead was then translated parallel to the cell surface (five microns) to accommodate a second probe particle within the PCM. Lastly, we

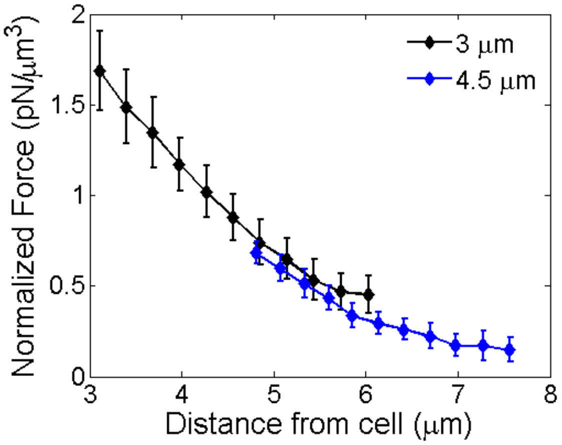

Figure 3.7 Normalized equilibrium force for two different bead sizes. The normalized force should be independent of bead size according to scaling theory analysis.

moved the second particle along the same path as the first, while monitoring the force on both probes. Nearly a dozen such measurements confirmed that the forces exerted on the second particle are similar to those on the first particle, with a typical force curves on both probes shown in Figure 3.9 (N=10). We interpret this observation as a clear indication that much of the PCM material responsible for the measured forces recovers behind the first probe bead as it is pushed inwards. Interestingly, we also observed that the final equilibrium force on the first bead remains constant when the second bead is translated into the matrix (see Figure A.1). This indicates that there is little mechanical coupling between the beads via the PCM despite their final separation from edge to edge of just two microns. This preliminary evidence that the RCJ-P cell coat is not a crosslinked network is in contradiction with the frequent depictions in the literature of the PCM as a gel-like network.

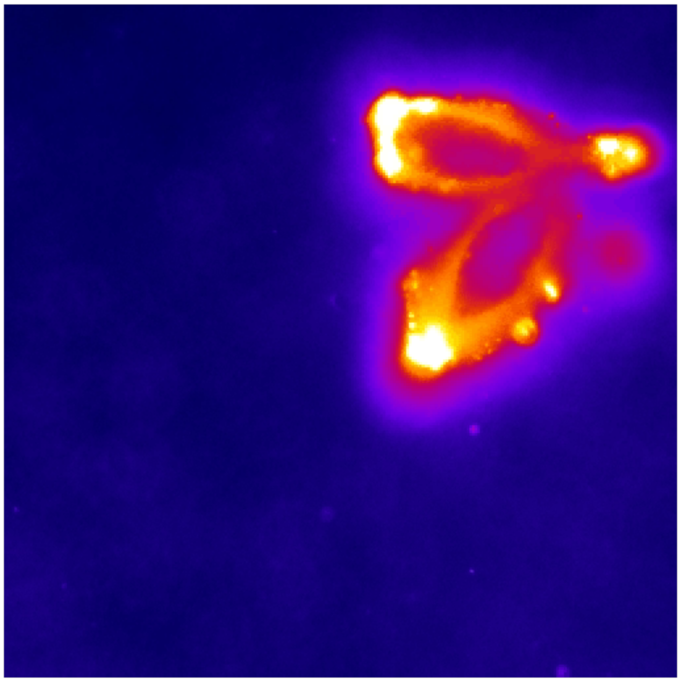

Figure 3.8 Results Visualization of a trapped particle penetrating through a PCM fluorescently labeled via GFPn. (mclane_louis_201311_phd_penetrate.avi, 17MB)

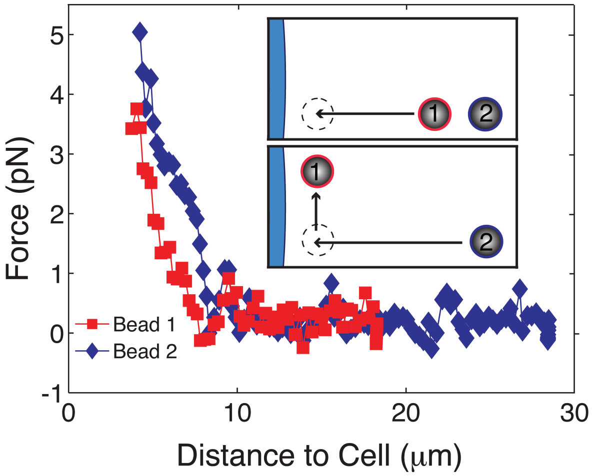

Figure 3.9 Probing the PCM with two probe particles reveals that particles penetrate rather than compress the matrix as they move towards the cell surface.

3.2.4 Exogenous aggrecan modified cell coats probed via optical force probe assays

The goal of our experimental procedures is not to only measure the physical and mechanical properties of rat chondrocyte cells, but to develop and use this technique as a tool to understand the PCM in general, and more specifically its role in many vital cell processes. To that end, the above results are also obtained for cells that are modified via exogenous aggrecan. This simple modification will allow us control how the cell coat is modified, and is used as a test for the usefulness of the techniques developed in this thesis to study the differences in cell coats. Briefly, we incubate our cells in high concentration of exogenous aggrecan, which results in substantially swollen cell coats as the added exogenous aggrecan binds within the PCM. The resulting modified structure of these coats is then probed using the methods detailed above in order to gain new understanding about the ways that cell coats can be modified, and more specifically how their structure changes from these modifications.

Dynamic force curve measurements are particularly useful to quickly register changes in the pericellular coat. The speed of their acquisition (~10 s) makes dynamic measurements a preferable readout in time-sensitive situations such as diagnostic applications or for example scenarios where the pericellular matrix is rapidly modified by the cell, like cell mitosis or migration. These processes where changes occur on the time scale of tens of minutes are particularly sensitive to longer timescale experiments. To demonstrate the sensitivity of this approach, we compare typical force signatures from cell coats before and after they have been incubated with exogenously-added aggrecan for two hours. This leads to a dramatic swelling of the PCM that is dependent on the proteoglycan concentration (Figure 3.6). When 333 μl/mg aggrecan is added, particle exclusion assays give an average thickness of $L_{o,PEA}$=17.6 +/- 1.3 μm (N=86), compared to 7.0 +/-0.5 μm (N=114) for the untreated RCJ-P cells (see Chapter 3.2.2).

Figure 3.10 compares the average dynamic force curve from measurements of the aggrecan-modified cells (N=17) with that of untreated control cells. The average inward dynamic force curve of the modified cell coats is well fit by a single exponential function with b=0.31+/0.10 μm^{-1}. The full extent of the coat is measured for each individual cell experiment at the location where the force first rises above the noise. Forces from the modified pericellular matrices are detected further from the cell surface $L_{o,dyn}$ =14.1+/-1.2μm as compared to the control cells, $L_{o,dyn}$ =11.5 +/- 1.1 μm. Despite this change in coat size, the peak dynamic force is similar between the control cells, 9.1 +/- 0.9 pN, and the aggrecan treated cells, 9.7 +/- 1.2 pN. This resemblance continues for the inner region of the coat (~3-4.5 microns) where the two curves agree to within 1 pN. The similarity of the curves suggests that the exogenous aggrecan is either not able to diffuse into the matrix due to steric and/or charge repulsion, or possibly that there are limited available binding sites along the HA chain. The increased forces beyond this region imply that aggrecan does find available binding sites at distances further out from the cell.

Further, the magnitude of the equilibrium force curves also changes in a very subtle manner (Figure 3.11). Again, the size of the coat swells significantly according to the classic PEA, while the differences in the equilibrium force curves are less immediately clear. While the curves have similar shapes, the only location in which the control equilibrium force curves deviate from the aggrecan swollen coats is in the outer regions of the coat. Here we see for the maximally swollen coat, that the forces in the outer edge go from 1.5 pN to 2.5 pN. We also find that the equilibrium force curve for

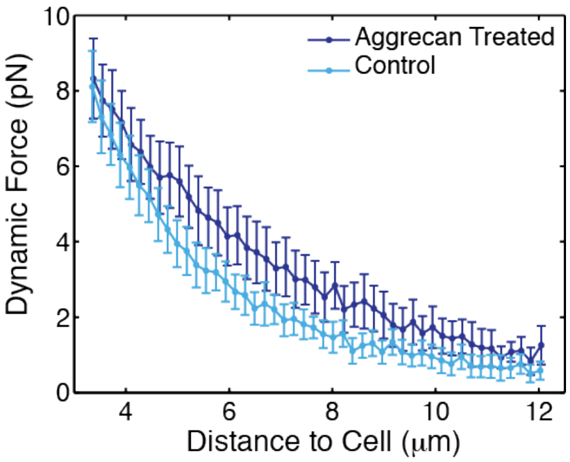

Figure 3.10 Dynamic force curve comparison between untreated, and cells treated with a high concentration of exogenous aggrecan (333 ug/ml).

the aggrecan treated cells actually dips below the control data in the inner most region of the coat, but this separation is not statistically significant. Additionally, the relaxation time once the probe reaches its final location inside the cell is hardly changed. For our sample at the higher concentration of exogenous aggrecan, fitting the first second of relaxation gives a relaxation time of 380+/- 150 ms, similar to the 320 +/- 200 ms observed for the control cells.

While much of the equilibrium force curves seem to overlap, the shapes of the curves are noticeably different. As shown above the correlation length profile is directly related to the exponent of these exponential varying force profiles. For the correlation length profiles of our aggrecan treated cells (Figure 3.12), we find a distinct separation between coats swollen with different quantities of aggrecan. As we incubate the cells with increasingly higher concentrations of aggrecan, the slope of the correlation length curves decreases. One possible interpretation of these results is that the added aggrecan finds empty binding sites within the coat, and fills up the space that was previously

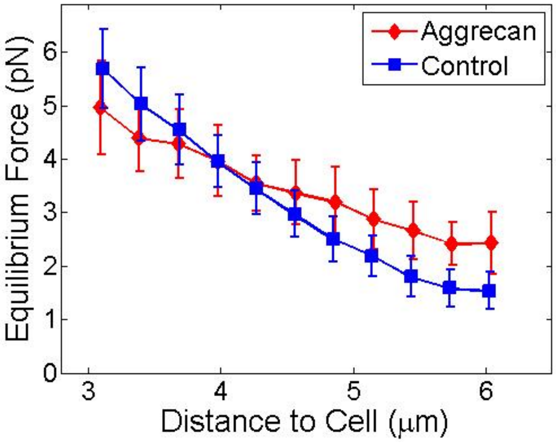

Figure 3.11 Equilibrium forces curve comparison between untreated, and cells treated with a high concentration of exogenous aggrecan (333 ug/ml)

unoccupied. Hence the coat will ‘tighten’ as the number of empty HA binding sites along the chain is reduced. As in the dynamic force studies, the positions closest to the cell membrane seem to be the least affected by the addition of exogenous aggrecan. Another possibility is that the exogenous aggrecan stimulates the cell to produce new hyaluronan, further altering the macromolecular structure of our coat. The mechanism by which the exogenous aggrecan alters the coat will be more fully investigated in Chapter 5. Regardless of the underlying mechanism responsible for the modification of the coat, both of these processes fit our previous interpretation that aggrecan is responsible for the main structural characteristics of the coat while the hyaluronan backbone acts more as an underlying collector of aggrecan and other proteoglycans.

Aside from showing proof of principal that our optical force probe assay techniques are valuable for distinguishing between modified and changing cell coats, the above results allow us to grasp further understanding about the intrinsic structure of the cell coat. We find that adding exogenous aggrecan alters the correlation length profile

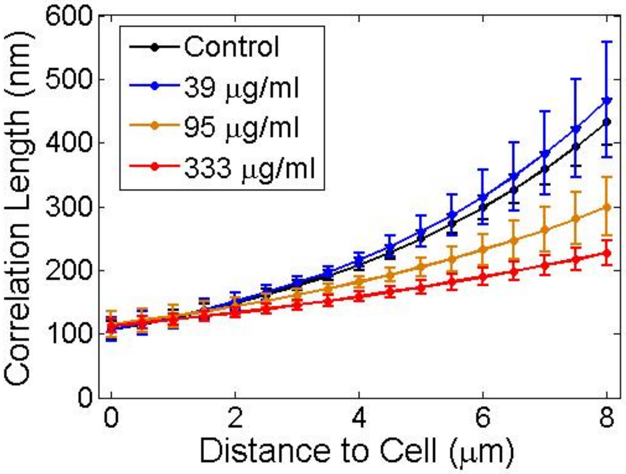

Figure 3.12: Correlation length profiles calculated for a range of exogenous aggrecan concentrations. The sample sizes are as follows: $N_{control} = 32$, $N_{39} = 8$, $N_{95} = 8$, $N_{333} = 11$.

within the coat, decreasing the mesh size throughout the coat, as is depicted in Figure 3.13. However this curve never completely reaches a constant value, implying that while the exogenous aggrecan is either occupying previously empty HA binding sites or the distribution of HA in the cell coat is uneven, or both.

Considering the size of our aggrecan (400 nm x 100 nm x 100 nm) and that it has an approximate molecular weight of 2.5 MDa (1), treating the aggrecan as hard packing objects results in a saturation concentration of 1000 μg/ml. The highest concentration (333 μg/ml) used is on the order of this value, meaning that it is highly likely that this is within the saturated situation. The fact that the correlation length profile is not flat, leads to the conclusion that in all likelihood the distribution of HA is not constant as a function of distance to the cell. If initially the correlation length profile was due completely to an unequal distribution of aggrecan rather than HA, adding more aggrecan would have filled in the empty spaces completely flattening the correlation length curve. The aggrecan concentration would now be equal everywhere, and would eliminate the equilibrium

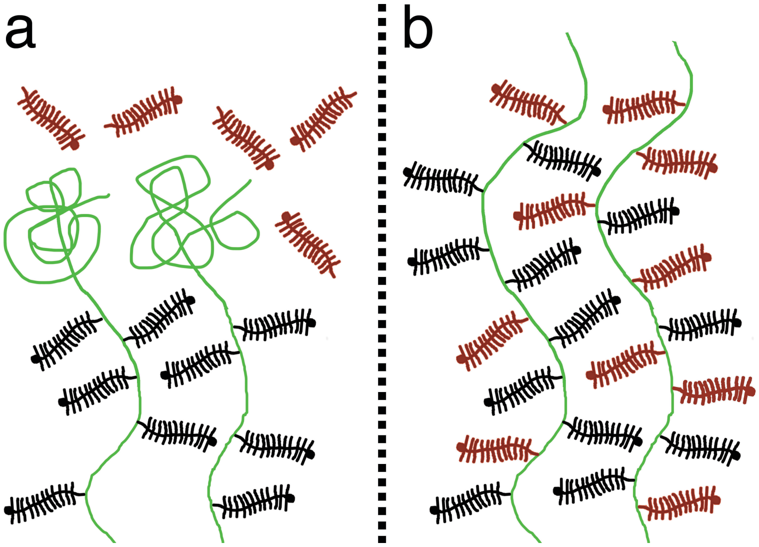

Figure 3.13: Proposed model of exogenous aggrecan incorporation into the PCM (a) The untreated coat is exposed to a high concentration of exogenous aggrecan in solution. The hyaluronan is green, the endogenous aggrecan is black, and the exogenous aggrecan is red. (b) After some incubation period, the exogenous aggrecan incorporates itself into the coat, both filling in the empty binding locations within the coat as well as stretching it outward.

force on our bead as it depends on a pressure gradient. Thus we observe that even the modified cell coats have some kind of underlying structure.

This structure is likely due to the fact that the distribution of HA length is not monodisperse. Hyaluronan is both attached to the HA synthase that produces it at the cell membrane, as well as the membrane protein CD44. While HA end grafted to the HA synthase, there is likely HA at many given stages of production (and thus length) at any given time. Further, the HA can attach to CD44 anywhere along its chain, making the final distribution of HA lengths in the cell coat extremely polydisperse.

3.3 Summary

The optical force probe assays presented in this chapter are an innovative technique developed to study the mechanical and structural properties of the pericellular matrix. This work was, to the best of our knowledge, the first measurement of the forces the cell coat can exert on micron sized particles. The assay considered both the dynamic forces of a particle moving through the coat at a constant speed, and the equilibrium forces that the coat can exert on a stationary bead buried within. The mere fact that the cell coat exerts a force on a stationary bead was an unexpected result, and lead to a connection to polymer physics. Scaling theory was used in order to get the first estimate of the correlation length (mesh size) profile within the coat. This correlation length can be interpreted as a characteristic length scale within the coat, and possibly the average opening within the coat at any distance from the cell.

The OFPA was also used to determine how the modification with exg-aggrecan changes the interior structure of the cell coat. The OFPA data suggests that addition of exg-aggrecan decreases the openings within the cell coat, decreasing the correlation length at every location within the coat. Given the fact that aggrecan is a main structural component of the PCM, an interpretation of how this newly introduced exg-aggrecan modifies the coat was developed with the help of the correlation length analysis. Further, this result suggests how additional aggrecan molecules binding to the cell coat can modify both its thickness and interior structure.

It is our belief that these OFPAs are an essential tool for studying malleable matrices such as the cell coat, and that their results will be useful for understanding the structure of similar systems. In addition we plan to perform the above assays on other modified cell coats, such as cells undergoing mitosis or migration, as well as completely new cell types. It is also possible to look at the forces the cell coat can exert while it is being modified, by measuring the forces exerted by a swelling coat in real time. Together with the qPEAs, the OFPA present a powerful tool that can be used to probe never before seen properties of soft materials. In the next chapter, we look to validate the interpretation that the cell coat has a varying mesh size via quantitative particle exclusion assays (qPEAs), as well as expand upon the quantitative results presented above.

CHAPTER 4

NOVEL PARTICLE EXCLUSION ASSAYS OF THE PERICELLULAR MATRIX

Traditionally, the pericellular matrix has been visualized and measured with what is called a particle exclusion assay (PEA). A particle exclusion assay is an indirect visualization of the pericellular matrix where fixed red blood cells are added to a cell sample. The RBCs are excluded from penetrating the area occupied by the cell coat, this exclusion area thus representing physical extent of the pericellular matrix. To perform a PEA, a layer of fixed red blood cells is added to cultured cells in order to visualize the PCM, as seen for our rat chondrocyte cells in Figure 4.1. If the cells are plated at a low enough density so that they are isolated from each other, the red blood cells will fill in the space between the cells.

When Clarris and Fraser (10) first added RBCs to human synovial cells, there appeared an excluded area where the red blood cells did not penetrate, and this was the first visualization of what we now call the pericellular matrix on mammalian cells. This observation of an exclusion zone around the individual cells was a surprise to researchers at the time. It was known that some cells in tissue or *in vivo* have a large space filling polymer layer that prevents direct cell-cell contact, but this was associated with the extracellular matrix, which is not cell associated and does not exist *in vitro*. This technique for visualizing and measuring the cell coat remains to this date the primary tool in labs all over the world (39, 61-62), and it is part of our objective to take this measurement to its next step, and to gain further quantitative information about not just the full extent of the pericellular matrix but also its interior structure.

As a nod to history and as a first approach we also perform these classical particle exclusion assays on our cells. These classical PEA studies are used along with newly developed quantitative particle exclusion assays (qPEA) to get a fuller understanding of the structure of the PCM. The quantitative particle exclusion assays use well-controlled monodisperse microspheres rather than red blood cells. Red blood cells can be polydisperse and have a biconcave disk shape, while the microspheres are spherical, have a well-controlled and modifiable size, and can be passivated via surface modification, resulting in greater experimental control. Further, these measurements can be directly compared to the results from the OFPA measurements (Chapter 3), verifying and elaborating upon the interpretations from those experiments. The results presented here demonstrate the power of these new quantitative particle exclusion assays, unraveling a structural view of the PCM to a degree never before seen.

4.1 Methodology

4.1.1 Traditional particle exclusion assays

Fixed sheep red blood cells (RBCs) (Sigma Aldrich, R3378, St. Louis, MO) were used for the particle exclusion assays (PEA). These RBCs (also called erythrocytes) were washed twice in order to remove any contaminants, and resuspended in PBS at a concentration of 100 mg/ml. 20 μl of this suspension was added to 300 μl of media and the RBCs were allowed to settle for 10 minutes before imaging. These concentrations are used in order to create a monolayer of RBCs on the surface of the sample so that the PEA can be visualized without any gaps between the cell coat and the erythrocytes. Classical

PEAs are imaged with differential interference contrast (DIC) microscopy when possible, and are otherwise imaged with bright field microscopy.

4.1.2 Quantitative particle exclusion assays

Carboxylated polystyrene microspheres were purchased from (Invitrogen, Grand Island NY). In the qPEAs, we used fluorescently labeled beads (Fluospheres, 580/605, 505/515 nm, Invitrogen, Grand Island NY). Passivation was achieved using two schemes. For larger particles (>200 nm), Pluronic F127 was absorbed to the surfaces and anchored to the particles through physical entanglement achieved by reversible swelling with toluene according to (63). Smaller microspheres were covalently modified with PEG (methoxypolyethylene glycol amine, Fluka, St. Louis MO) according to an existing protocol (64).

Passivated, fluorescent polystyrene spheres (Fluospheres, Invitrogen, Grand Island, NY) of varying size (40 - 3000 nm) were used to characterize the PCM. 50 μL of beads were added to 170 μL media (in Teflon ring) and allowed to settle for 10 minutes. To facilitate image analysis, the cell surface was fluorescently labeled using wheat germ agglutinin (WGA-Alexa Fluor 633 conjugate, Sigma, St. Louis, MO), which was added to the sample (125 μg/ml) five minutes before measurements. The samples were imaged with a confocal microscope (Olympus FV1000, Tokyo, Japan). The microsphere distribution perpendicular to the cell surface (at a location similar to where optical force probe assays were performed) was surveyed by measuring the intensity distribution (averaged over 2 μm). The effective thickness, d_{eff}, was extracted by identifying the plateau in the average bead intensity. Controls showed that using multiple bead sizes

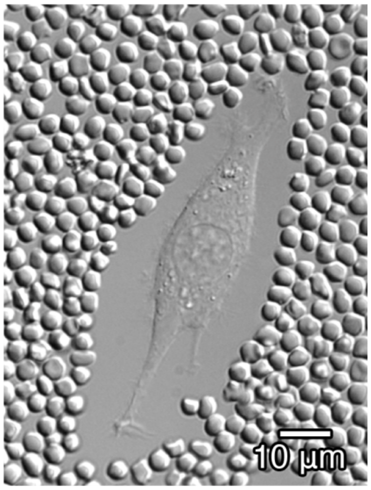

Figure 4.1 Rat chondrocyte imaged with a classical particle exclusion assay via DIC microscopy

simultaneously or exchanging the particles alters the observed particle distribution and d_{eff}. To avoid artifacts, qPEAs were therefore performed using a fixed bead size for a given cell sample.

4.2 Results and discussion

4.2.1 Traditional particle exclusion assays

Classically, particle exclusion assays were analyzed by finding the ratio between the area occupied by the red blood cells and that of the cell body. For our experiments we have chosen instead to measure the thickness of the coat perpendicular to the middle of the cell body. This was done in order to match the measurements of the coat thickness to the location on the cell where the optical tweezer work was performed (Chapter 3). Locally flat areas along the cell body are chosen for both of these studies in order to minimize the effect that cell curvature may have on the experiments. A typical PEA on control rat chondrocyte cells can be seen in Figure 4.1. For our control cells the thickness

Table 4.1 Summary of the physical parameters measured in optical force probe assays of the pericellular matrix on the RCJ-P cell line for both control cells and cells modified with exogenous aggrecan. The error reported is twice the standard error.

Average Values	**Control (N=30)**	**Aggrecan-treated (N=17)**
F_{dyn} peak (pN)	9.1 ± 0.9	9.7 ±1.2
F_{eq} (pN)	5.5 ± 0.7	3.9 ± 0.9
$L_{o,PEA}$ (μm)	7.0 ± 0.5 (N=114)	17.6 ± 1.3 (N=86)
$L_{o,dyn}$ (μm)	11.5±1.1	14.1 ± 1.2
$L_{o,eq}$(μm)	8.0 ± 0.6	13.1 ± 2.1 (N=11)

at this point in the cell is $L_{o,PEA}$ = 7.0+/-0.5 μm (N=114), which can be compared to the thickness observed via other techniques in Table 4.1. Interestingly, the traditional particle exclusion assay is less sensitive to the size of the coat than are the optical tweezers measurements, providing further evidence for the need of more sophisticated measurement techniques.

While these traditional PEAs are a good preliminary measurement of coat size, their discrete measurement technique reveals no information about the interior structure of the PCM. Because of the large size of the red blood cells, they are unable to pass through the coat and can only yield information about the full extent of the PCM. In order to probe the inner structure of the coat, we have developed quantitative particle exclusion assays. The qPEAs are able to penetrate the coat and reveal previously unknown information about its organization. The ability of the smaller sub-micron particles to penetrate through the cell coat can then be analyzed in junction with the results obtained

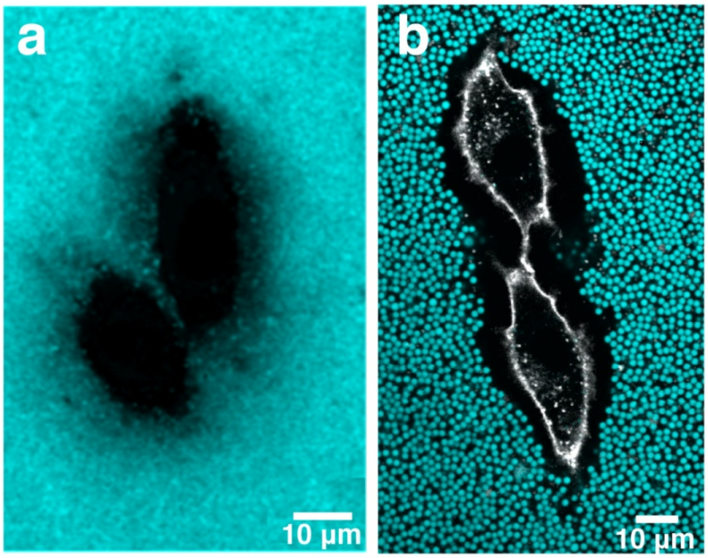

Figure 4.2 Rat chondrocytes visualized with blue (a) 100 nm and (b) 2 µm size particles. The cells visualized with 2 µm sized particles are also stained with WGA (white) in order to visualize the cell membrane.

from the optical force probe assays, as both reveal information about the interior structure of the cell coat.

4.2.2 Quantitative particle exclusion assays

In order to expand upon the results obtained by the classical PEA, a complementary assay referred to as the quantitative particle exclusion assay (qPEA) is developed. In this approach, we use passivated microspheres of well-defined sizes to probe the accessibility of the cell coat for objects of different sizes. These assays show that particles become non-uniformly distributed throughout the matrix in a size dependent fashion. Typical images of the cell coat being probed with two different bead sizes are shown in Figure 4.2. The 100 nm beads shown in Figure 4.2a are able to penetrate further into the cell coat, resulting in a concentration gradient within the coat. For the larger two

Table 4.2 The measured full width half max (FWHM) of the Gaussian oscillations measured in individual bead profiles, as compared to the expected size due to diffusion and imaging.

Particle Diameter	Measured FWHM	Convolved Size
100 nm	920 nm	860 nm
300 nm	760 nm	600 nm
500 nm	440 nm	570 nm

micron beads shown in Figure 4.2b they display a more binary behavior, where the particles reach the edge of coat and stop there, unable to penetrate through the coat.

The way that the smaller particles are able to penetrate within the coat, and the resulting profile of their distribution will reveal information about the interior structure of the PCM. To quantify how this profile variation depends on the bead size used to probe the coat, we measured the intensity profiles of fluorescent microspheres as a function of distance to the cell. Figure 4.3 shows typical intensity profiles associated with different particle sizes. The intensity profile for particle sizes less than 500 nm consists of non-zero intensity at the cell surface followed by a gradient of increasing intensity until it reaches a plateau. The change in concentration for beads 500 nm and larger is abrupt, with little to no transition zone.

The oscillations in the qPEA bead profiles are due to the diffusion of the finite size particles during confocal imaging. If the particles were completely stationary there would still be oscillations, as the profile would pick out the Gaussian shape of individual particles. However as the particles are diffusive these peaks become spread out, as confocal imaging is not instantaneous. The imaging process scans the image one pixel at a time (typically 8 μs per pixel); giving the beads time to diffuse between pixel scans. Convolving the Gaussian shape of the particles with their diffusion explains the feature

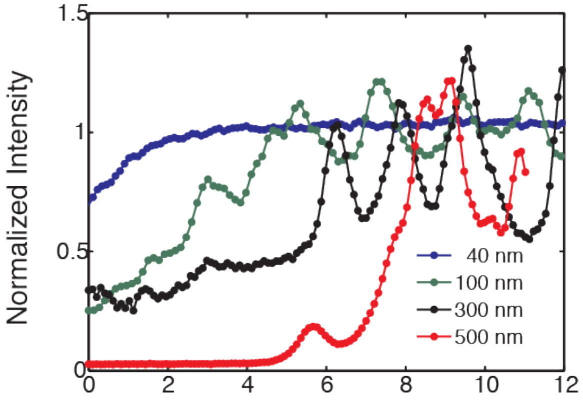

Figure 4.3 Quantitative particle exclusion assays (qPEA) using monodisperse passivated beads ranging from 40 nm to 500 in diameter.

size seen in the individual profiles (see Table 4.2). These oscillations can be removed by doing a time-averaged image, where 30 successive images are averaged in order to smooth the profile (Figure 4.5). This technique will be used for future experiments, as they are more amenable to modeling.

When the particles are introduced into the sample and encounter the PCM they diffuse into the PCM. As the beads diffuse into the coat their concentration decreases as they reach positions closer to the cell surface. The results presented here are concerned with the place in the profile where the concentration of beads first starts to decrease from its maximum value. We call this location inside the cell coat where the profile first plateaus the effective thickness, d_{eff}. A schematic of how different bead sizes result in different effective thickness of the coat is shown in Figure 4.4.

Analysis of the particle distribution as a function of bead diameter show that the PCM acts as a sieve for passivated particles of different sizes. The profiles show that the particle concentration roughly plateaus at a distance d_{eff} that depends on the particle size. Figure 4.6 shows how the average effective thickness of the coat increases with

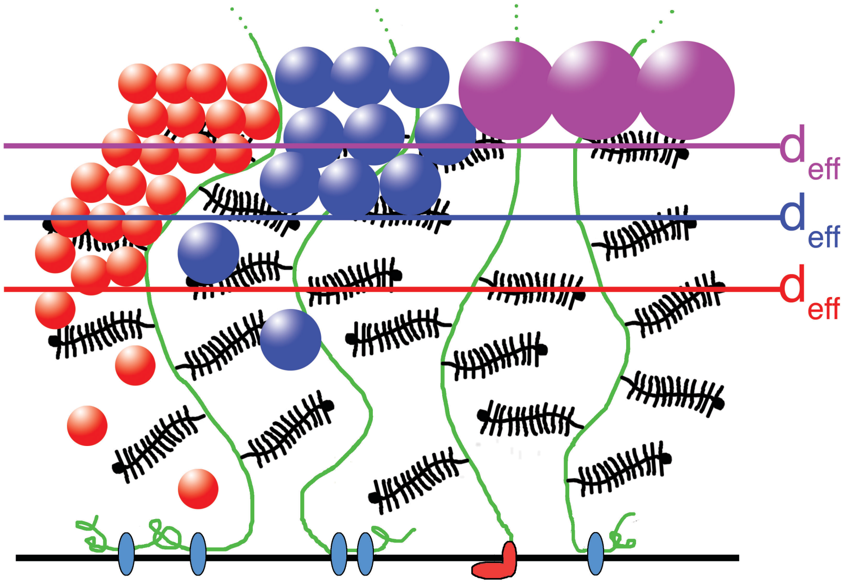

Figure 4.4 Schematic of the qPEA measurements showing the measurement of the effective thickness, d_{eff}, for different bead sizes. Experimentally only one bead size is added at a time, where here three bead sizes are shown on the same coat for clarity in understanding how d_{eff} changes with respect to bead size.

increasing particle diameter, with results given for bead sizes ranging from 40 nm to 3000 nm. The same data is also summarized in Table 4.3. This result that different sized particles penetrate different distances into the cell coat is consistent with the optical force measurements, suggesting that the ability of particles to penetrate the pericellular matrix decreases as the particle size increases, confirming that the mesh size is indeed spatially varying. Interestingly, particle sizes of 500 nm and greater have the same average effective thickness, $d_{eff,500}$= 8.5 +/- 0.8 μm, suggesting that this is the edge of an inner domain within the PCM. This measurement of the edge of the cell coat is also consistent with the equilibrium thickness measured by the optical force studies, $L_{o,eq}$=8.0+/-0.6 μm and is consistent with tradition red blood cell PEAs.

Table 4.3 Summary of results from the quantitative particle exclusion assay (qPEA). d_{eff} is an average number extracted from the analysis of intensity profiles of the bead distributions from N cells for each bead size.

Bead diameter (nm)	**Effective thickness, d_{eff} (μm)**	**N**
40	1.4 ± 0.3	31
100	3.3 ± 0.4	43
200	5.2 ± 0.6	40
300	6.7 ± 0.5	65
400	7.1 ± 0.7	38
500	8.5 ± 0.8	59
2000	8.1 ± 0.9	58
3000	8.6 ± 1.4	19

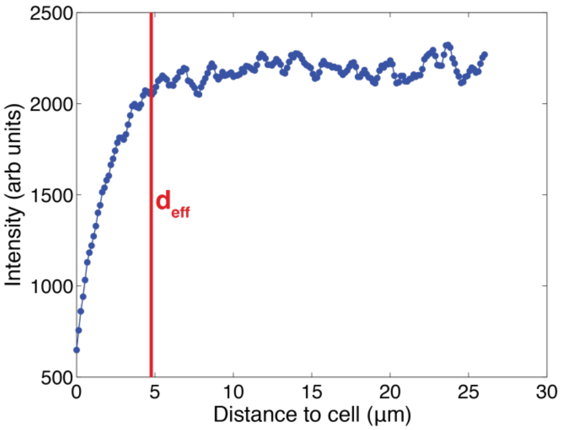

Figure 4.5 Time averaged profile of 100 nm beads, with an identification of d_{eff} for this particular cell.

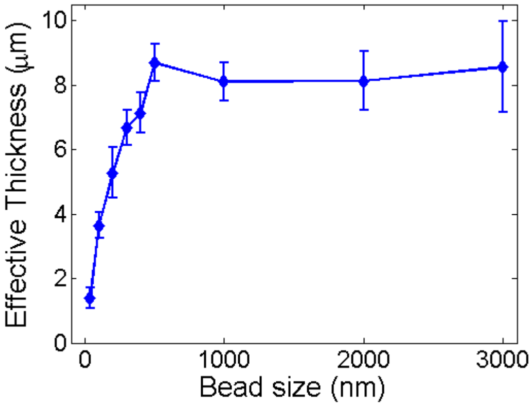

Figure 4.6 The effective thickness associated with probe size increases until it plateaus at ~8.5 μm where probes 500 nm in diameter and larger are excluded from the PCM completely. The change in d_{eff} indicates that the cell coat acts like a sieve.

4.2.3 Exogenous aggrecan treated cell coats probed via particle exclusion assays

4.2.3.1 Traditional particle exclusion assays

As was done in Chapter 3 for the newly developed OFPA technique, the traditional and quantitative PEAs explored above are also applied to cells modified via incubation with exg-aggrecan. In short, the cells are incubated with varying concentrations of exg-aggrecn in order to swell the PCM. We find that the size of the cell coat as measured by a classical PEA performed with red blood cells can be carefully controlled (Figure 4.7) by varying the concentration of exogenous aggrecan solution. Remarkably, the full extent of the cell coat can be more than doubled by the addition of exogenous aggrecan. The growth of the coat stops at concentrations above 200 μg/ml, as the size of the coat no longer increases for higher incubation concentrations. The coat swells from a size of 7.3 μm up to 17.6 μm.

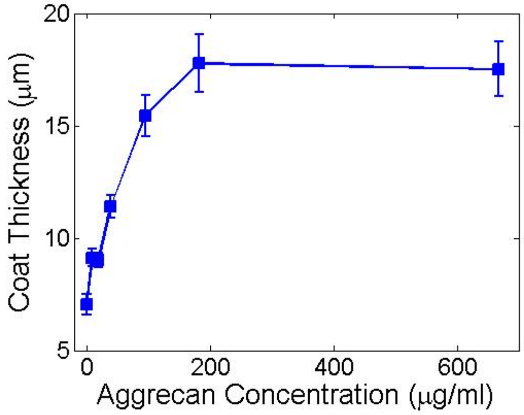

Figure 4.7 Swelling RCJP coats via exogenous aggrecan. For our RCJ-P cells the PCM more than doubles in size, starting at 7.3 μm and plateauing at 17.6 μm as measured by the classical PEA.

4.2.3.2 Quantitative particle exclusion assays

These exg-aggrecan modified cell coats can also be probed via the quantitative particle exclusion assays developed above Particles in sizes ranging from 40 nm to 3 μm are added as they were with the control cells. First, we explore how different concentrations of aggrecan change the profile of the coat as it is probed by a single bead size. Figure 4.8 shows the visualization two cells where the PCM is measured with a 100 nm qPEA, while Figure 4.8a shows representative profiles taken from two individual cells. The profiles are taken from time averaged images (N=30) of one cell. The effective thickness as it is probed by the 100 nm beads, more than doubles in size from 3.6 microns to 7.6 microns. Similar to the results from the traditional particle exclusion assays (Figure 4.5), the effective thickness of the coat plateaus at some ex-aggrecan concentration between 100 and 200 μg/ml.

Not only does the addition of aggrecan increase the effective thickness (measured with the 100 nm beads) of the coat by pushing the d_{eff} of the beads outward, but it also changes the gradient of the particles within the coat (Figure 4.9b), as this gradient is more

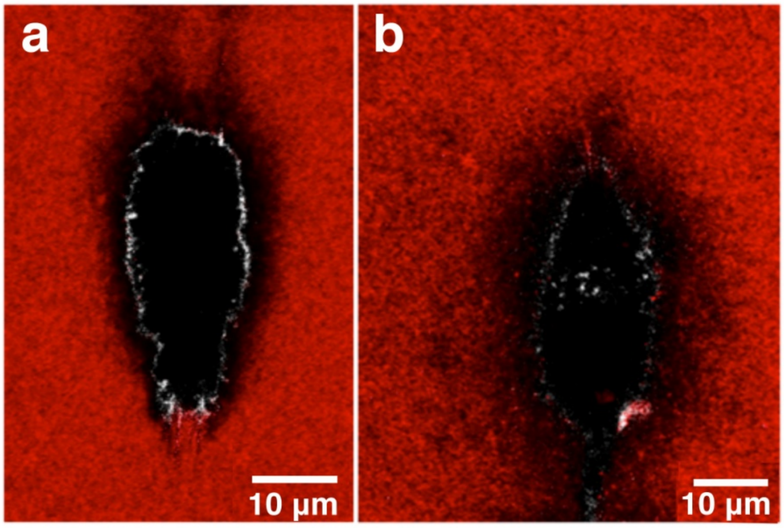

Figure 4.8 100 nm quantitative particle exclusion assays on both (a) control and (b) aggrecan treated cells. The cell membrane is also labeled with a WGA dye (white). Red 100 nm beads are added to control and aggrecan treated cells (different cells) and allowed to diffuse into the coat. The addition of aggrecan increases the full extent of the coat as well as changing the gradient inside the coat.

evident and gradual in the aggrecan treated cells. The nature of this gradient and how it changes with the addition of exogenous aggrecan or with other processes will be explored in future work.

The bead size dependence of the effective thickness, d_{eff}, of the PCM of exg-aggrecan treated cells is shown in Figure 4.10 and Table 4.4. Qualitatively, the PCM of the aggrecan modified cells are structured in a manner that is similar to the untreated cells, as the modified coats acts as a sieve separating the particles by their bead sizes. The smaller beads are able to penetrate through the coat, where they form a gradual profile as fewer beads are able to enter the inner regions of the coat.

In the case of the untreated cells, we found that beads smaller than 500 nm were able to penetrate the coat, resulting in a d_{eff} ranging from 1.4 to to 8.5 μm. For the exg-aggrecan treated cells, only beads 200 nm and smaller were able to penetrate the coat,

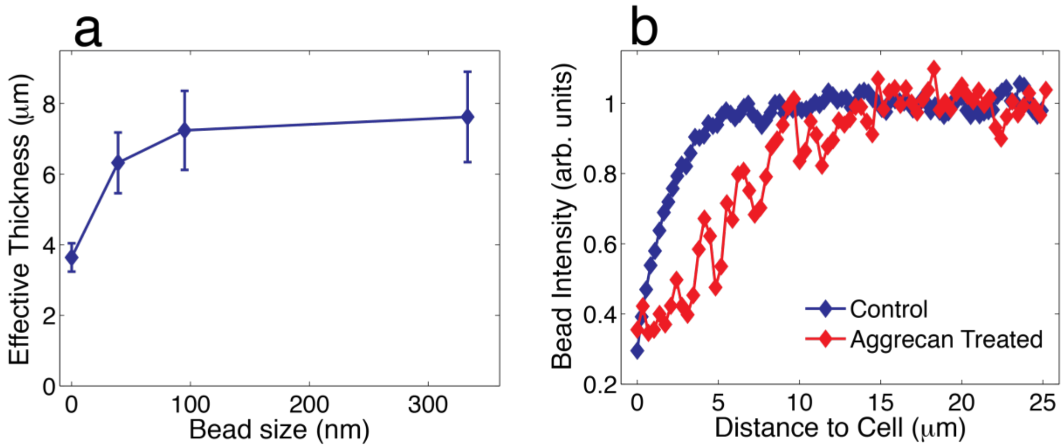

Figure 4.9 (a) Effective thickness of the cell coat as a function of aggrecan incubation concentration for 100 nm particles. (b) Comparison between representative qPEA profiles for 100 nm beads for both treated and untreated cell coats.

measuring a d_{eff} ranging from 2.4 to 13.4 μm. Bead sizes larger than 200 nm did not enter the PCM, and consistently plateaued at the same average location, independent of bead size. This particular distance where particles of all sizes above a certain threshold rest is considered to be the periphery of the cell coat, as defined by qPEA experiments. Further, for each bead size the effective thickness of the coat increased, as well as shifting the

Table 4.4 Full qPEA results for aggrecan treated cells

Bead diameter (nm)	**Effective thickness, d_{eff} (μm)**	**N**
40	2.4 ± 0.4	18
100	7.6 ± 1.3	27
200	11.4 ± 1.2	21
300	13.4 ± 0.7	23
500	12.6 ± 0.8	115
1000	12.7 ± 1.5	30
3000	12.0 ± 1.5	43

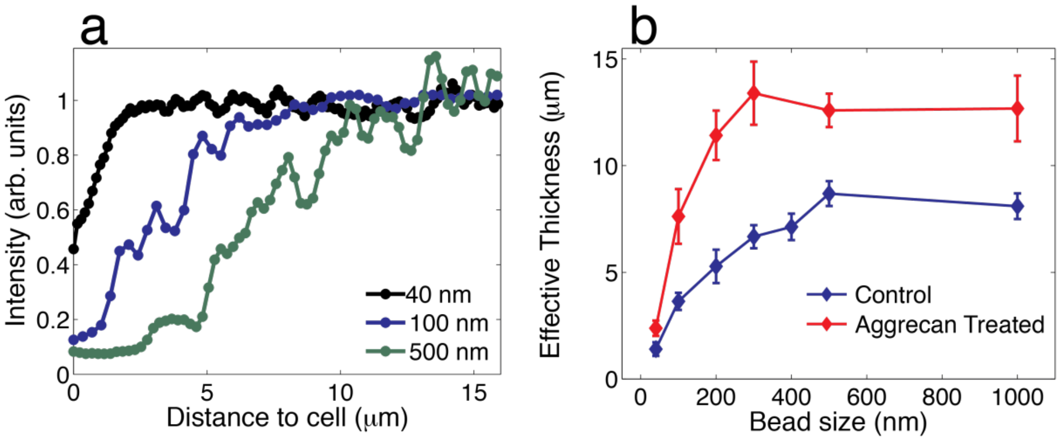

Figure 4.10 (a) Time averaged individual cell coat profiles for multiple bead sizes for the exogenous aggrecan treated cells. (b) Cell coat thickness for both control and aggrecan treated cells (333 μg/ml) as determined by qPEA.

overall curve to the left, as beads that were once able to penetrate the coat no longer are able to do so. It appears that treating the PCM with exg-aggrecan 'tightens' the spacing within the matrix, where the average opening at any particular position within the PCM decreases as aggrecan fills the previously available empty space.

4.3 Mesh size comparison between OFPA and qPEA results

The pericellular matrix has so far been probed with two newly developed experimental techniques, those being the optical force probe assay developed in Chapter 3 and the particle exclusion assays described here in Chapter 4. While they each reveal new and interesting information about the structure of the cell coat, comparison between the two assays strengthen the results and our interpretation of what these results reveal about the PCM. The OFPA results were used to extract a correlation length (mesh size) profile throughout the coat. Correlation length can also be thought of a 'mesh size', or an average opening within the polymer mesh. This non-constant correlation length profile is interpreted to mean that the average opening in the cell coat is not constant, and that the size of the openings within the coat increases at distances further away from the cell membrane. We take this concept, and use it to directly compare the OFPA results to the results from the quantitative particle exclusion assays. The qPEAs revealed that the cell coat acts like a sieve, separating particles by their size. Smaller beads were able to penetrate further, as their smaller sizes apparently permit them to fit inside the tighter spaces within the cell coat. This section directly compares these results in order to develop a cohesive understanding of the PCM structure.

4.3.1 Comparison for untreated cell coats

Conceptually, the results from the OFPA and qPEA studies are highly compatible, as a varying correlation length can be directly interpreted that that the coat acts like a sieve for the cell. With the mesh size, or average opening within the coat, being smaller closer to the cell surface larger particles will be stuck outside the cell while the smaller particles are allowed to penetrate through the cell coat. This would allow smaller molecules such as growth factors to reach the cell surface, while larger possibly undesirable matter is kept away from the cell surface. The qPEAs directly demonstrate that the cell coat behaves in this manner. The position to where a particle can easily penetrate, defined as the effective thickness (d_{eff}), correlates directly with bead size, where larger particles are held further away from the cell membrane.

Further, the qPEA results can be semi-quantitatively compared to the correlation length profile predicted by the OT work. Recall that the effective thickness, d_{eff}, for a particle is the distance to the cell surface at which the concentration of the particle

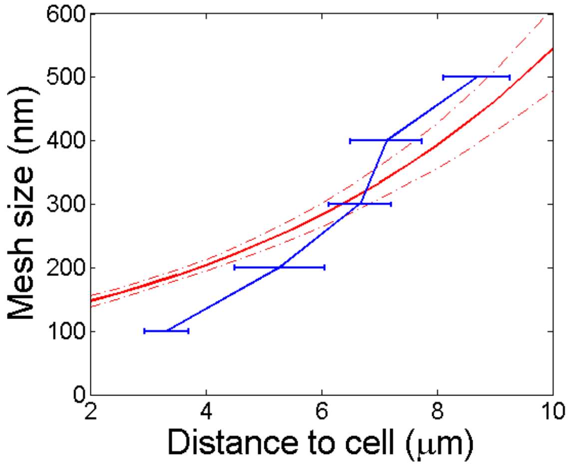

Figure 4.11 Comparison between the correlation length profile calculated from the optical force probe assay results and the quantitative particle exclusion assay data.

distribution reaches a plateau. At this location the mesh size of the coat is considered to be the same as the size of the particle. Thus particles can easily penetrate any regions of the coat where the mesh size is larger than their diameter. However when the particles reach a mesh size that is smaller than their diameter they are stopped by the PCM, as they can no longer easily diffuse past this point. Some of the particles do pass this point, but this is likely due to the fact that the coat is not a stiffly crosslinked network, as fluctuations in mesh size and particle position result in some of the particles passing this point. The qPEA profile can then be thought of as a probability distribution for the positions of a particle within the cell coat.

Thus for a quasi-quantitative comparison, we conjecture that the bead size corresponds roughly to the correlation length in the PCM at the effective thickness where that bead size shows constant concentration. In other words, the d_{eff} from the qPEA results corresponds to the distance to the cell, and the bead size corresponds directly to the correlation length at this position. We note that 40 nm bead data are excluded from this comparison because the plateau is at $d_{eff,40}$=1.4 +/- 0.3 μm, a distance where microvilli complicate the PCM structure on RCJ-P cells (2). With these assumptions, the qPEA data can be recast as correlation length versus position in the pericellular coat. Overlaying the optical force data with the *ad hoc* qPEA curve provides a visible comparison as shown in Figure 4.11. Overall they qualitatively agree, as both depict an increasing mesh size for increasing distances from the cell. Additionally, for beads larger than 200 nm the two agree within error. Although they do not fully agree quantitatively, the two assays are conceptually consistent as they both show an increasing mesh size at distances further from the cell membrane.

Quantitatively, the OFPA results yielded an exponentially varying correlation length, where the scaling of the exponential is 0.17+/- 0.02μm^{-1}. Assuming the qPEA data also behaves exponentially, fitting the qPEA data to an exponential function yields an exponent of 0.29 μm^{-1}. This value for the mesh size scaling that is almost twice that from the optical force measurements, revealing a weakness in the assumptions used for our comparison. In the future, optimizing experiments to perform both assays on the same cell to avoid averaging over measurements could greatly improve the comparison, or at least be used to identify the source of the weakness in our comparison. Our assumption that the effective thickness for a specific bead size is directly analogous to the correlation length could be further investigated by a full theoretical treatment of the qPEA results. We expect this analysis will provide guidance for a more precise comparison between the two techniques, and is currently underway.

The data extracted from the optical force probe and qPEA assays together provide strong evidence that the pericellular matrix has a spatially varying mesh size. The penetration of 40 nm particles to the surface and their uniform distribution at $d_{eff,40}$=1.4

μm suggests the mesh size ranges from a sub-100 nm length scale near the surface to ~500 nm at a distance of approximately eight microns from the cell surface. The comparison of the qPEA results to the correlation length profile refines our grasp of the true values for the mesh size of the cell coat, as the calculation of the correlation length is only semi-quantitative given the fact that there is an unknown scaling factor in its result.

4.3.2 Comparison for aggrecan treated cells

The optical force probe and quantitative particle exclusion assays outlined above have also been performed on the aggrecan modified cells, and these results can again be directly compared. Recall that the cell coats were modified by incubating the samples in a high concentration of aggrecan, the proteoglycan that help gives the cell coat its large thickness. Results shown in Chapters 3&4 illustrate that the addition of aggrecan not only greatly swells the full extent of the cell coat, but that it also modifies the internal structure of the cell coat by binding to empty binding sites along the hyaluronan backbones.

As with the untreated cells, the sub-micron particles used in the qPEAs are distributed within the coat in a manner that is highly compatible with the concept of the coat having a varying mesh size profile. The effective thickness of the coat increases for increasing bead size, however for the aggrecan treated cells only beads 300 nm and smaller are able to penetrate into the cell coat. The fact that so few of the bead sizes are able to penetrate the coat makes comparison to the OFPA data difficult. Qualitatively the qPEA data for our aggrecan treated cells lines up reasonably well with our correlation length curves obtained from the optical tweezer force data (Figure 4.12). Quantitatively, the exponential fit to the OFPA data yields an exponent of 0.08 +/- $0.02\mu m^{-1}$, while

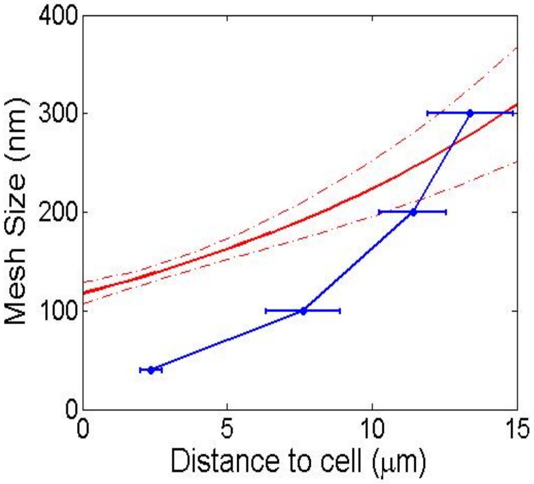

Figure 4.12 Comparison of qPEA effective thickness for multiple bead sizes with the correlation length profiles of aggrecan treated cells

fitting the qPEA with an exponential function yields an exponent of 0.19 μm^{-1}. Similar to the non-treated cells, these values agree to an order of magnitude, but the exponent of the qPEA fit is approximately 2 times larger than the OFPA fit. This disagreement may point to a limitation in our model, either with the correlation length calculation or with the qPEA simplification for the meaning of d_{eff}.

As with the control cells, the results for the aggrecan treated cells agree for beads 200 nm and larger. Unfortunately beads above 300 nm are unable to penetrate the treated coats, limiting the number of data points available for the qPEA analysis. The fact that beads 100 nm and smaller do not agree in either our treated or untreated cells may be a hint to the limitations of this comparison and analysis. It is our hope that future experiments will unravel the source of the breakdown in the comparison between these two different assays. However, the fact that the effective thickness 'seen' by the particles increases with the addition of exogenous aggrecan supports the proposed scheme that this treatment ‘tightens’ up the cell coat, restricting the access of foreign objects to the inner cell coat as well as the cell body.

4.4 Summary

This chapter presented work that studied the pericellular matrix with both traditional and quantitative particle exclusion assays. As is the standard in the field, the first approach to studying the cell coat of the RCJ-P cells (which are the subject of this work) was to measure them with a traditional PEA. The traditional PEA, which uses a layer of fixed red bloods to create an ‘exclusion zone’ around cells plated in vitro, determined the average thickness of the cell coat to be 7.0 μm. Once this baseline for coat thickness was measured, the cells were modified by incubation with exg-aggrecan. The exg-aggrecan binds to the hyaluronan in the cell coat, stretching it outward. The exg-aggrecan concentration dependent thickness of our cell coats was measured, showing proof of principle for a method to controllably modulate the thickness of cell coats.

In addition to using pre-existing techniques to measure the PCM, a completely novel quantitative particle exclusion assay was developed to probe the interior structure of the cell coat. The qPEA uses a technique similar to the traditional PEA, but where the red blood cells are replaced with monodisperse micron and smaller particles. When introduced to the cell coat, the particles are separated by bead size, as smaller beads are more able to penetrate the cell coat than are larger beads. To our knowledge, this is the first proof that the PCM acts like a sieve, separating incoming particles by size. The exg-aggrecan treated cell coats were also probed via qPEAs, resulting in the first measurement of how the interior structure of the PCM changes when modified via change in its structural components. During this modification, the cell coats not only became larger in full extent, but also tightened up as particles that were once able to penetrate the coat can no longer do so.

This interpretation is further validated by the results presented in Chapter 3 for the optical force probe assays. The two assays both establish that cell coat has a varying mesh size, and that quantitatively the spaces within the cell coat are sub-micron. We are optimistic that these newly developed qPEAs will unlock a multitude of future experiments, and that a theoretical model based upon these results will further refine our model of the pericellular matrix structure.

CHAPTER 5

QUANTITATIVE FLUORESCENT AND DYNAMIC STUDIES OF AGGRECAN SWOLLEN COATS

Insights into the nature and structure of the pericellular matrix presented here have thus far considered cell coats that are in approximate equilibrium with their surroundings. While these experiments result in a new and essential understanding of the PCM, a portion of future work will focus on cell coats that are undergoing dynamic processes such as cell migration or division. As a first step in studying dynamically changing cell coats, we study the direct way that exogenous aggrecan (exg-aggrecan) modifies the cell coat in real time. Recall that exogenous aggrecan is not aggrecan produced by the cells, but is purified aggrecan obtained from an external source. Both classical particle exclusion assays, as well as newly developed fluorescence microscopy studies are used in order to study the cell coats as they are actively being modified by the addition of exogenous aggrecan. The information gained from these studies can then be seen as a launching point to studying cells that are transforming during physiological processes.

The newly developed fluorescent studies allow for direct measurement the distribution of the incorporated exg-aggrecan, and in addition are essential for studying the dynamic changes of cell coats. The optical force probe and particle exclusion assays allowed us to gain more information about the structure of the PCM than ever before, however they are an indirect measurement of this structure. The fluorescently labeled aggrecan used in the experiments below will allow us to take our knowledge one step

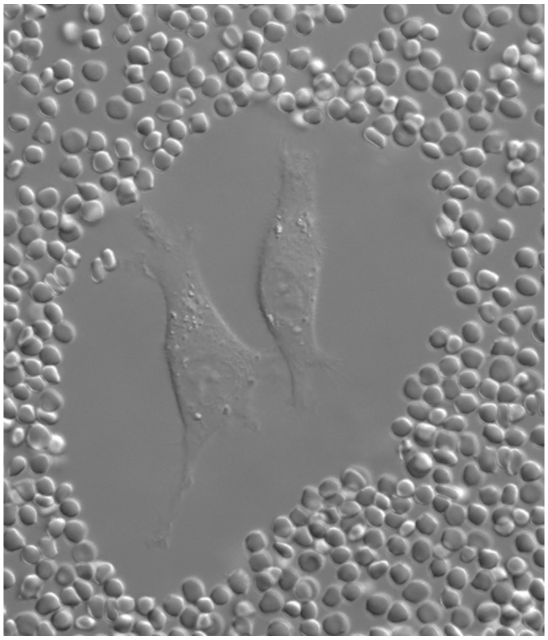

Figure 5.1 Visualization of the live growth of a cell incubated with exogenous aggrecan via bright field microscopy. (mclane_louis_201311_phd_growth.avi, 78 MB)

further, and to gain direct evidence as to how the cell coat is structured, and how this structure changes in a dynamic cell system.

5.1 Live growth studies of cell coats treated with exogenous aggrecan

For the studies where exg-aggrecan was used to swell the pericellular matrix, a two-hour incubation time was initially chosen in order to ensure that the exg-aggrecan is fully incorporated into the cell coat. The resulting studies (Chapters 3&4) were the first to quantitatively measure the transformed PCM, as well as compare the resulting structure to that of the untreated cells. However in order to understand the mechanism thought which the aggrecan is incorporated, and how this interaction results in the swollen coats, the temporal nature of this swelling must be considered.

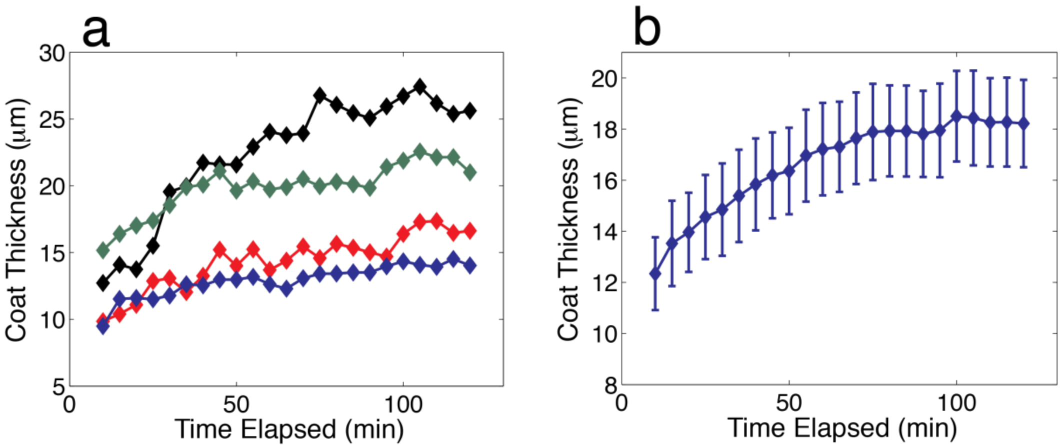

Figure 5.2 Time growth of (a) four individual and (b) the average (N=21) growth of cell coats exposed to exg-aggrecan.

To study the time-dependent swelling of the cell coats, the cell media is replaced with a high concentration of exg-aggrecan (333 μg/ml). Red blood cells are then immediately added to the system and allowed to settle and create a particle exclusion assay. Monitoring of the live growth of the cells starts at ten minutes after the exg-aggrecan is added. Unfortunately this technique does not allow measurement of the initial ten minutes of growth, as this is the time required for the RBCs to settle and highlight the exclusion zones. The sample is then imaged every five minutes for two hours to observe real time swelling of the PCM. The instrumentation further allows visualization of multiple cell coats for each time point as the stage was preprogrammed to image multiple positions in the sample. For these studies, each sample is imaged at ten distinct positions every five minutes. Figure 5.1 shows a still from a movie showing live growth of the cell coats for a pair of cells during this experiment, and Figure 5.2a displays four different individual cell growth curves, while Fig 5.2b reports the average coat size at each time point extracted from data acquired for N=21 cells.

The results indicate that the final extent of the cell coat is strongly dependent not only on exg-aggrecan incubation concentration (Figure 4.7) but also incubation time. The cell coat grows an average of four microns within the first ten minutes, and continues to grow another six microns until it plateaus at ~ 18 μm for the longer time points. For the longer growth it appears, on average, that the coat requires at least 100 minutes of incubation to equilibrate in size. This time growth of the cell coat hints towards a possible two stage growth, where the rate of growth is much higher in the first ten minutes of aggrecan incubation. Taking the rough estimate that the growth is approximately linear growth for the two time periods, the rate of PCM expansion in the first ten minutes is 400 nm/min, while the rate of growth for the remaining 110 minutes is 50 nm/min, approximately eight times slower than the first period. Possible mechanisms for this time dependent expansion of the PCM are explored in Chapter 5.6, after a description of other useful insights gained from novel quantitative experiments using fluorescent exg-aggrecan.

5.2 Profile measurements of bound fluorescent exogenous aggrecan

While both the traditional and quantitative particle exclusion assays provide a measurement of the full extent of the cell coats swollen with exg-aggrecan and in the case of the qPEA, possibly even an indirect measure of the interior structure of the modified coats, neither currently provides information about the way that the newly introduced aggrecan is incorporated within the coat. In order to observe the distribution of aggrecan within the coat directly, the added exg-aggrecan is fluorescently labeled and then is directly imaged via confocal microscopy. This newly developed assay will allow

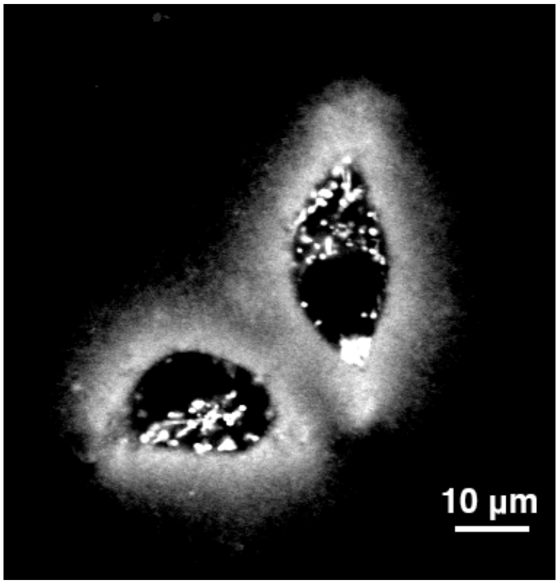

Figure 5.3 Representative image of cells incubated with fluorescent exg-aggrecan at 260 µg/ml. After incubation the fluorescent exg-aggrecan is bound to the coat, resulting in the halos seen above. The intensity observed inside the cell is due to ingestion of exg-aggrecan.

direct measurement of the location and relative concentration (which is proportional to the intensity) of the bound exg-aggrecan.

Prior to addition to the cell sample, the exg-aggrecan was fluorescently labeled as outlined in Chapter 2.3. As with the other exg-aggrecan experiments, these coats were then incubated with the fluorescent aggrecan for two hours. After rinsing away any unbound exg-aggrecan, the cell coats are imaged fluorescently, thus allowing direct measurement of the bound exg-aggrecan. A typical image for the coats labeled with fluorescent exg-aggrecan is shown in Figure 5.3, while the distribution of the fluorescent aggrecan within the cell coat is shown in Figure 5.4.

To extract a profile from a single cell, five images were taken in succession and then averaged in order to minimize any noise in the data. A two-micron wide profile

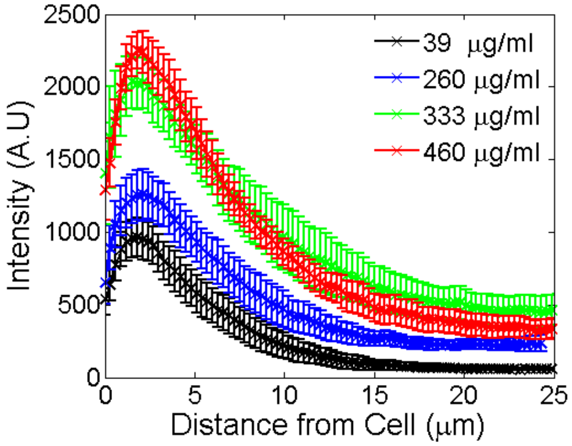

Figure 5.4 Distribution of fluorescently labeled exogenous aggrecan at four different solution concentrations. The curves are averages over the following sample sizes: N_{39} = 21, N_{260} = 24, N_{333} = 22, N_{460} =24.

was taken from this averaged image, resulting in a single intensity profile for each measured cell. As with the other studies, a locally flat region on the side of the cell was chosen in order to minimize the effect of cell curvature and for consistency. The data shown in Figure 5.4 represents the average exg-aggrecan intensity profile at four different solution concentrations.

For a single profile the intensity of fluorescent aggrecan, which corresponds directly to the concentration of bound exg-aggrecan, starts from a constant value outside the coat and increases at distances further inside the coat. At a few microns from the cell surface the concentration peaks, and then drops down, although not to its initial value, at the cell surface. Before saturation, at any location inside the cell coat the concentration of bound exg-aggrecan increases as the incubation concentration increases. This indicates that changing the incubation concentration of exg-aggrecan results in higher quantities of bound aggrecan. The fact that no difference can be distinguished between the cell coats

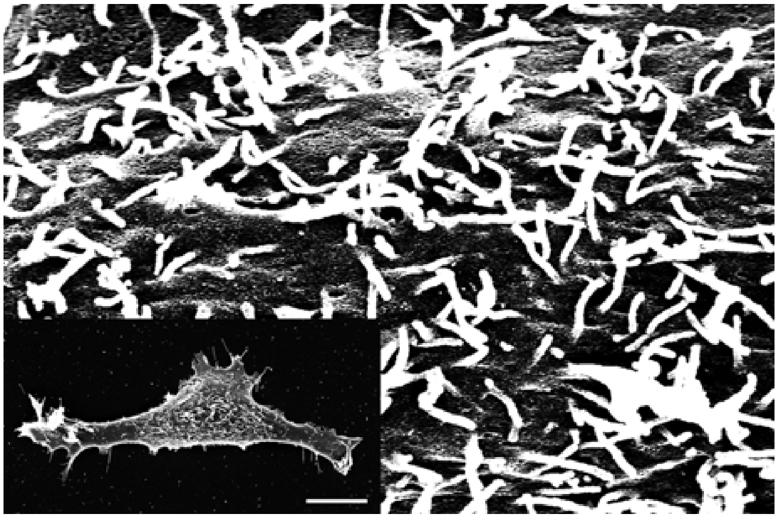

Figure 5.4 SEM image of critically point dried RCJ-P cells and a close-up of the cell surface, reprinted with permission from (2). The surface of an RCJ-P cell is covered with micron sized microvilli. Scale bar is ten microns.

incubated in 333 μg/ml and 460 μg/ml supports the conclusions gained from the traditional PEA aggrecan swelling results (Figure 4.6) and the correlation length studies addressed in Chapter 3. Here it was shown that incubation at 333 μg/ml of exg-aggrecan, the cell coats are saturated with exg-aggrecan and cannot be expanded or modified with higher incubation concentrations.

Strikingly, the aggrecan profile for each concentration measured does not peak at the cell surface, but at a few microns from the membrane. The position of the cell membrane is determined with wheat germ agglutinin (WGA) staining, where WGA labels the sialic acid found in the lipid bilayer. The observation that the highest aggrecan concentration peaks a few microns from the cell edge is likely due to the fact that the plasma membrane for the RCJ-P cells is not flat, but is decorated with microvilli (Figure 5.4). The highest density of hyaluronan which is available for aggrecan binding is then not directly outside the cell, but is in the region past the extension of the microvilli at a few microns from what is identified as the edge of the cell.

The fact that the fluorescent exg-aggrecan concentration peaks close to the cell membrane and decays as this distance increases also supports the results obtained from the OFPA and the qPEA studies. The correlation length result obtained via the OFPA data indicated that distances closer to the cell membrane had a smaller mesh size, a consequence of this region having an overall higher density of aggrecan. In the fluorescent aggrecan studies, the added exg-aggrecan finds free binding locations not only on the outer rim of the coat, but all throughout the coat. This profile peaks closer to the cell, indicating that the highest densities of available binding sites are the locations closest to the cell. Therefore, even though we have previously shown that this region contains the highest concentration of native aggrecan, this location still has an abundance of freely open binding locations.

Besides directly measuring the concentration and distribution profile of bound exg-aggrecan, this measurement is useful as it can be used to determine the density of available binding sites on the bound hyaluronan strands. Aggrecan native to the PCM is stabilized with link protein (65-67), and the HA-link-aggrecan complex is considered to be irreversible. Any pre-bound native aggrecan within the coat with remain bound even when the PCM is exposed to high levels of exg-aggrecan. Thus the exg-aggrecan can only bind to sections of hyaluronan that previously contained no native aggrecan, directly measuring the distribution of available binding sites. The data in Figure 5.4 indicates that the PCMs studied become saturated with exg-aggrecan when incubated at a concentration of at least 333 μg/ml. Because higher incubation concentrations are not able to alter the amount of bound exg-aggrecan, it is possible that the hyaluronan that was originally available is now completely filled. Thus in the case of saturation, the fluorescent aggrecan directly measures a spatially-averaged distribution of all previously available binding sites along the hyaluronan chains.

The above observation of possible hyaluronan saturation is consistent with the measurements of HA-aggrecan binding affinity (68). In that work, the disassociation constant, K_d, between HA and aggrecan was reported to be 86 nM. A common interpretation of K_d is that it is the concentration of ligand (here aggrecan) at which half of the receptor (HA) sites are filled. The observed K_d for HA and aggrecan can be converted to a mass concentration (assuming aggrecan has a molecular weight of 2.5×10^6), yielding a concentration of 220 μg/ml, independent of the HA concentration. In an ideal receptor/ligand model, HA will be half filled with aggrecan when incubated at a concentration of 220 μg/ml. This model does not take into consideration the natively bound aggrecan, which is assumed to be permanently bound (65), nor the physical restraints that may exist within our system. It is likely that in the native PCM the hyaluronan strands are not all completely stretched out. The strands may be folded over on themselves or even entangled, limiting the regions which are available for aggrecan binding as these effects might further reduce the effective number of binding sites. Considering these complications, it seems entirely probable that an incubation concentration of 333 μg/ml is able to completely saturate our cell coats.

The next stage of these experiments will be to use fluorescent aggrecan to study the distribution of all bound aggrecan within the PCM. This would allow direct comparison of these results to the results obtained by the biophysical methods outlined in previous chapters, and would lead to cohesive understanding of the structure of the PCM. It has been shown (65) that the presence of link protein makes the bond between HA and native aggrecan effectively irreversible. One way to determine the complete distribution of bound aggrecan, all previously bound endogenous aggrecan must be removed before treating the cell coats with the fluorescent exg-aggrecan. This could possibly be achieved by treating the cells with aggrecanase, which is an enzyme that specifically digests aggrecan. Digesting the protein leaves the protein binding domain intact, however this is not an issue as the minimum spacing between protein binding domains is a miniscule 12 nm (66). In the cell coat the minimum spacing between aggrecan binding sites is primarily determined by the physical space taken up by the large proteoglycans (100nm x 400nm), thus rendering the 12 nm restriction zone from the digested aggrecan inconsequential. Adding exg-aggrecan after endogenous digestion will then allow us to directly measure and modulate the quantity and distribution of all bound aggrecan within the cell coat.

Below, the usefulness of labeling the PCM with fluorescent exg-aggrecan is expanded upon, as it is used to study the dynamics of the fluorescently labeled aggrecan in order to determine the time scales involved for exg-aggrecan binding and releasing from the cell coat. To our knowledge this is the first study developed to study the way exg-aggrecan actively interacts with an existing cell coat *in vivo*.

5.3 Photobleaching does not occur over imaging conditions

Dynamically observing the coats treated with fluorescent exg-aggrecan requires successive imaging over the same cell at long timescales. A concern for these types of

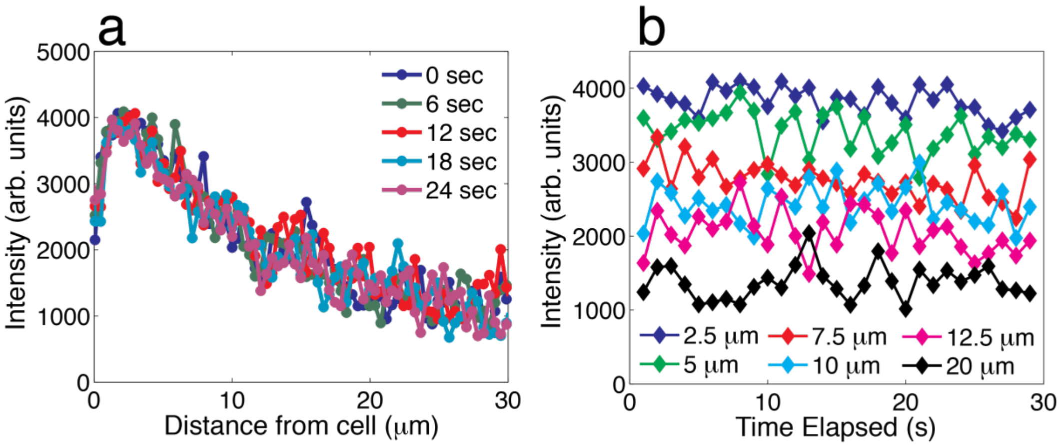

Figure 5.6 (a) Profile of a swollen cell coat shown over rapid imaging to display the minimal effect of photo bleaching. Profile is imaged once a second for 30 seconds. (b) Position slices of the full data show little to no signal loss after 30 exposures.

experiments stems from photobleaching of the fluorescent molecules. Photobleaching is the phenomenon that over time and exposure, fluorescent dyes will lose their ability to emit light. The main source of photobleaching is exposure to light, although contact with free radicals in solution can also lead to destruction of fluorescence. We performed controls to measure the rate of photobleaching due to light exposure. To do this, a sequence of images was taken of cells treated for 2 hours with fluorescent exg-aggrecan. Care was taken to use the same settings on the confocal microscope for this control experiment, as those used during typical experiments. As the data shown in Figures 5.6a and 5.6b show, the extracted intensity profile of the PCM on a single cell remains unchanged within the noise level after four exposure events. To evaluate the photobleaching over a greater number of exposures, the intensity corresponding to multiple positions within the cell coat is plotted versus time (or equivalently, the exposure number since the images are one second apart). Typical data for a cell exposed

30 consecutive times for imaging is reported in Fig. 5.6b. The data reveals no significant decrease in signal after thirty exposures.

We assume in this work, that photobleaching that occurs due to exposures separated by longer periods of time is similar to the photobleaching observed in these experiments, where the interval between images was short, lasting only six seconds. A control for longer intervals is difficult due to other factors that lead to a changing aggrecan distribution and integrated intensity. These considerations are discussed below.

5.4 Bound exogenous aggrecan erodes over time

In order for an aggrecan molecule to escape from the cell coat, it must not only unbind from a single hyaluronan strand, but must also diffuse past other objects in the cell coat such as other aggrecan, as well as other hyaluronan strands which can re-bind the diffusing aggrecan molecule. This phenomenon is most clearly observed when after incubation of the cell coats with exg-aggrecan, the excess unbound exg-aggrecan is removed from the system. The system is now out of chemical equilibrium, and exg-aggrecan will unbind and leave the PCM. In the below section we study how the equilibrium dynamics drives release of exg-aggrecan from the cell coat.

As before, the cells are incubated with the fluorescently labeled exogenous aggrecan for two hours. The exg-aggrecan is then replaced with normal cell media to image the bound fluorescent aggrecan. This sudden change in the reservoir concentration of aggrecan leads to a shift in the chemical equilibrium. We therefore expect the fraction of bound exogenous aggrecan to decrease until a new equilibrium is reached. The timescale of this change is critical to know for other experiments on aggrecan-treated

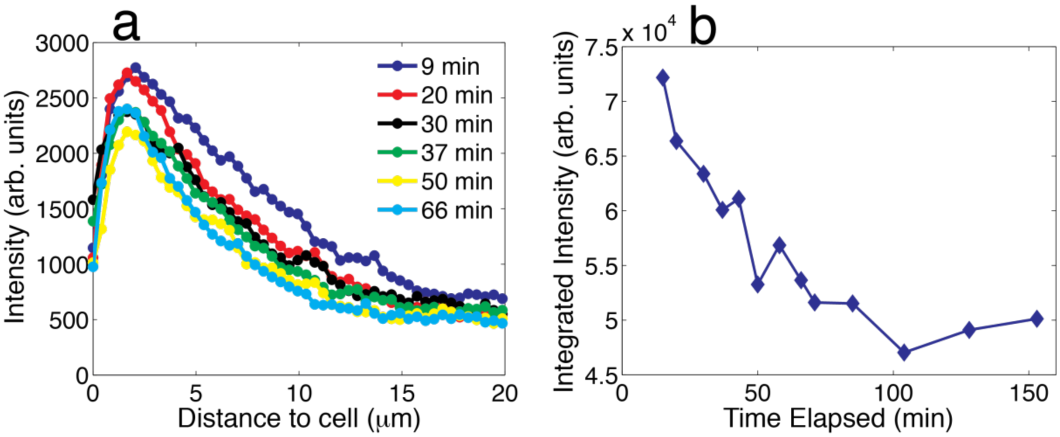

Figure 5.7 (a) Erosion of the swollen cell coat over time as it incubates in an exogenous aggrecan free environment. (b) The integrated intensity at each time point.

cells, since we prefer to measure a quasi-static structure. Hence, we study the dynamics of the bound aggrecan in this aggrecan sparse environment, by extracting the evolution of the exogenous aggrecan profile over time, as shown in Figure 5.7a.

A slow erosion of the bound exogenous aggrecan takes place over time throughout the coat. Each exg-aggrecan molecule has a binding affinity with hyaluronan that is smaller than the endogenous aggrecan (which is stabilized by link protein). Because the interaction between exg-aggrecan and HA is not permanent, this complex has some probability of disassociating, and over time the bound exg-aggrecan will release and either re-bind to the same HA strand or diffuse into the cell coat. As the exg-aggrecan molecule diffuses through the coat it can bind to any other HA strand it encounters, or it can diffuse into the surrounding media if it is near the edge of the coat. It is this diffusion of exg-aggrecan into the surrounding media that causes the apparent erosion of the cell extent of the cell coat as defined by the fluorescent exg-aggrecan.

To measure this erosion, the total intensity curve at any time point is integrated, as the integrated intensity is directly proportional to the quantity of the exogenous aggrecan. The time evolution of the integrated intensity shown in Figure 5.7b indicates that the swollen coat equilibrates in this representative experiment at some time between 60 and 100 minutes after removal of the exg-aggrecan.

Naively, one might expect for the cell coat to erode outside in, as the outer regions of the coat are closer to the cell media and are thinner, resulting in a higher probability that any aggrecan that unbinds from its hyaluronan strand is more quickly released into the surrounding media. Analysis of the data, however, suggests that the *relative* erosion rate is the same both in the inner and outer regions in the coat (Figure 5.8b). This uniform slow erosion is likely a result of the fact that erosion occurs not only at the surface of the PCM, but also everywhere inside its bulk. The exg-aggrecan in the interior of the PCM is just as likely to unbind and diffuse away from the cell coat as exg-aggrecan at the outer rim. After approximately an hour the aggrecan distribution within the coat plateaus, seemingly reaching equilibrium with the surrounding media.

Since the background unbound exg-aggrecan has been removed from the media, the dynamics of this system is initially determined by the unbinding of exg-aggrecan from HA. Surface plasmon resonance experiments have been previously used in order to determine the off-rate (k_{off}) of HA-aggrecan binding (68), yielding a value of $2.5x10^{-3}$ s^{-1}. The inverse of this value determines a characteristic bond lifetime τ_{off}, which is 6.67 minutes for the ideal HA-aggrecan system. A system where the dynamics are driven completely by the unbinding of the ligand (aggrecan) from a receptor (HA) should follow a decaying exponential function (69)

$$f_{bound} = f_0 e^{-t/\tau_{off}} \qquad \text{Eq. 5.1}$$

where f_0 is the initial concentration, and τ_{off} is a characteristic bond lifetime.

Our data seems to behave in a similar manner, although falling to a constant non-zero value, and fitting the data shown in Figure 5.7a to a decaying exponential:

$$f_{bound} = Ae^{-t/\tau_{off}} + c \qquad \text{Eq. 5.2}$$

yields an average characteristic time τ_{off} = 33 +/- 6 minutes. This value is approximately 5 times longer than the value reported for a pure HA-aggrecan system, and demonstrates that the structure of the PCM influences transport of molecules to and from the cell.

The disagreement between our system and the results reported for an ideal HA-aggrecan system can be explained from the complexity of the PCM as compared to the simpler system. As described at the top of this section, the structure of the PCM may result in multiple binding and unbinding events. This would lead to a considerable increase in the effective off rate for unbinding aggrecan, indicating that our observed escape of exg-aggrecan is due to roughly five unbinding events. Further, the fact that our system does not decay to zero for long time scales is likely a result of the fact that the reservoir around the PCM is not constantly being replenished. In surface plasmon resonance experiments there is a constant flow of ligand free media over the receptors. Any ligand that unbinds then gets washed away and will never again bind to the receptor.

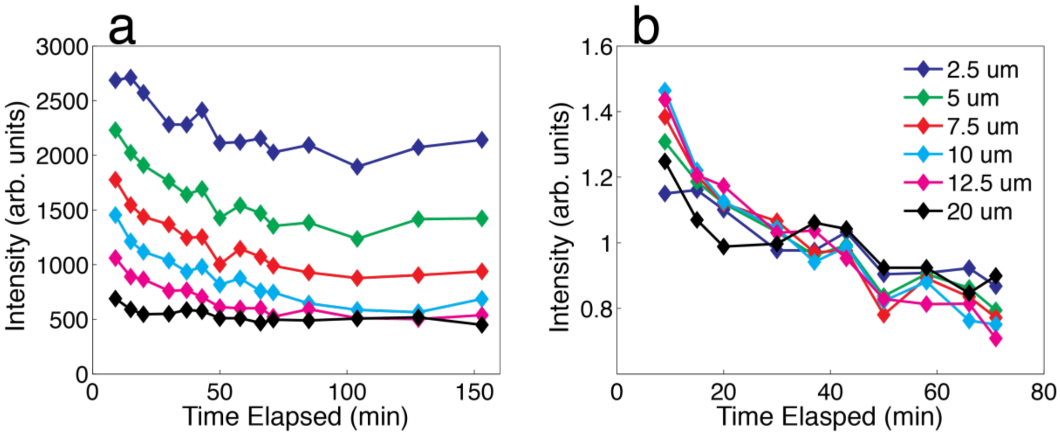

Figure 5.8 (a) Slices of the first plot showing the time dependence of the fluorescent aggrecan concentration at individual positions within the cell coat. (b) The curves in (a) are normalized by their average value and indicate that the relative erosion rate is the relatively constant as a function of position.

For the results presented above, the exg-aggrecan free media is never replaced, as the motion of exg-aggrecan that unbinds from the PCM is driven by diffusion. Over time the unbound exg-aggrecan then creates a new background concentration of exg-aggrecan, and results in the non-zero concentration of bound exg-aggrecan.

The ability to study the exg-aggrecan swollen coats in a static environment is brought into question by the fact that the cell coat erodes slowly over time in an aggrecan sparse environment. In order to image the fluorescently labeled coats, the background unbound fluorescent aggrecan must be removed from solution (which was also done in the OFPA and qPEA experiments for consistency). However as Figure 5.6 demonstrates, the newly introduced aggrecan from the coat unbinds, slowly eroding the coat. As the erosion seem to be slow (less than 1% per minute) it does not seem to compromise our results as this change is negligible over our imaging time scales (on the seconds time scale). In order measure the coat as closest as possible to its largest configuration in the

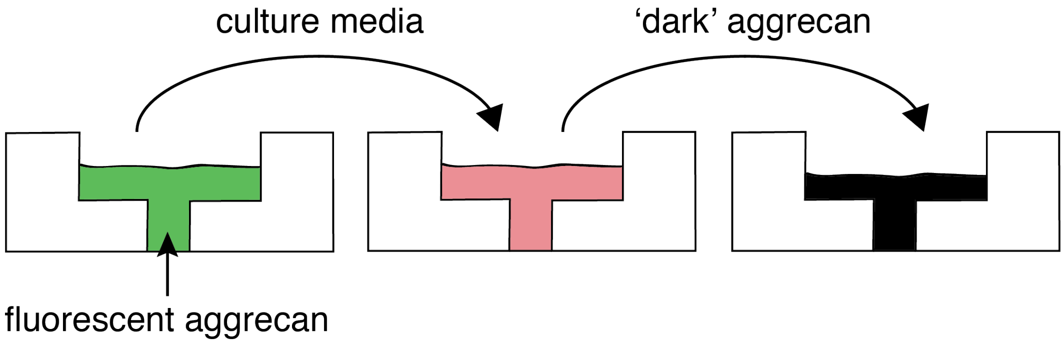

Figure 5.9 Schematic of the steps used to image the fluorescent aggrecan replacement experiments. The fluorescent aggrecan must be replaced in solution for imaging. The imaging media is then replaced by the non labeled 'dark' exg-aggrecan.

above experiments, cells were typically imaged 5 minutes after replacement of the fluorescent aggrecan with cell media.

Previous experiments have shown for a pure hyaluronan/aggrecan system the τ_{off} is 7 minuteszc. Fitting the data shown in Figure 5.7a exponentials like that in Eq. 5.1 gives an average τ_{off} = 148 minutes. Aside from the large disagreement in the characteristic time of decay of our data from the simple HA-aggrecan system, our system reaches a non-zero equilibrium value at longer time scales. A system of simple unbinding should reach zero concentration, as any ligand that unbinds from the system typically never rebinds.

5.5 Aggrecan replacement indicates fast penetration of exogenous aggrecan into the pericellular matrix

In addition to studying the erosion of pre-bound exg-aggrecan as the aggrecan is released from the cell coat into solution, the use of fluorescent exg-aggrecan reveal how quickly exg-aggrecan in solution penetrates into and binds to the PCM. The below

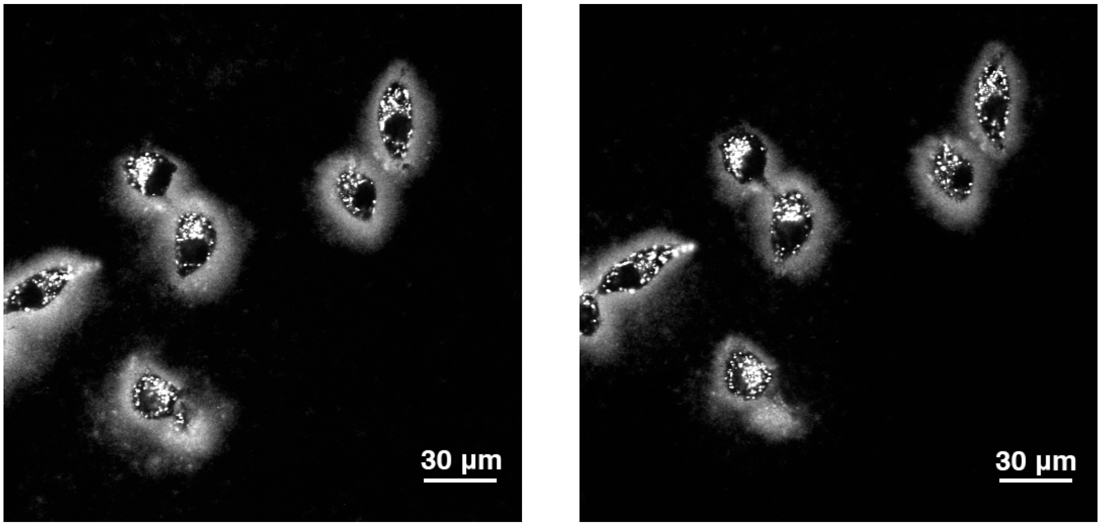

Figure 5.10 (a) Cells exposed to fluorescently labeled exogenous aggrecan are imaged immediately after replacing the fluorescent aggrecan solution with cell media (b) The same cells are shown ten minutes after replacing the media with non-labeled exogenous aggrecan at the same concentration.

experiments yield information about how quickly the exg-aggrecan incorporates itself within the cell coat, and demonstrates the accessibility of cell coats to external modifications. Further they illustrates how even though the cell coat has been shown to have a mesh size on the order of 100 nm (Chapters 3&4), molecules larger than this mesh size such as aggrecan can quickly penetrate and interact with the PCM.

Cells were once again incubated at a high concentration of fluorescent aggrecan (333 μg/ml) for two hours. As depicted in Figure 5.9, the fluorescent aggrecan solution is removed and replaced with media to image the distribution of bound fluorescent exg-aggrecan. The solution is then replaced with another exg-aggrecan solution at the same concentration as the initial media, but where the newly introduced aggrecan is not fluorescently labeled. Images of cells undergoing this procedure are shown in Figure 5.10. The fluorescence, and hence concentration, of the previously bound labeled exg-

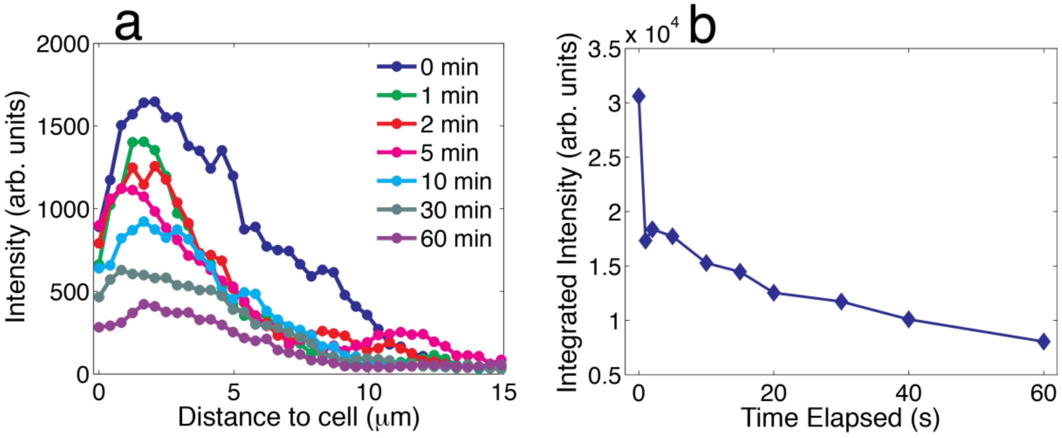

Figure 5.11 (a) Time dependent concentration profile of a cell treated with fluorescent exogenous aggrecan for 2 hours, followed by incubation with 'dark' aggrecan. (b) The integrated intensity of each time point shows that over 40% of the intensity drop occurs in the first minute.

aggrecan can then be measured over time (Figure 5.11) as the coats pre-bound with fluorescent exg-aggrecan interact with the surrounding solution of unlabeled exg-aggrecan.

Visually (Figure 5.10), we observe that the fluorescence of the cell coats partially fades soon after the replacement of fluorescently labeled exg-aggrecan with 'dark' exg-aggrecan, supporting our assertion that the exg-aggrecan, unlike the endogenous aggrecan, does not permanently bind to the cell coat. Quantitatively (Figures 5.11 & 5.12), 45 percent of the bound fluorescent aggrecan within the coat is replaced after just one minute. As the sample is allowed to further incubate in the solution of non-fluorescent aggrecan, we find that after one hour nearly all of the fluorescent aggrecan within the coat has been replaced.

Remarkably, the initial effective turnover rate of aggrecan into and out of the cell coat is on a minute time scale. While it takes over an hour for full equilibration, it is still

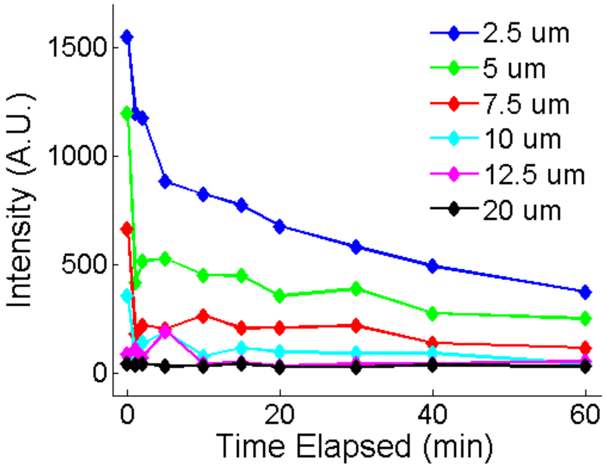

Figure 5.12 Position slices of the profiles shown in Figure 5.9. A large portion of the pre-bound exg-aggrecan is replaced within the first minute of exposure to unlabeled exg-aggrecan.

surprising that much of the replacement occurs at such a rapid pace. Thus even in swollen coats which contain a high, possible saturated (Chapter 3.2.3), concentration of aggrecan, newly introduced exg-aggrecan can quickly penetrate and start to modify the existing cell coat. This result is intriguing considering the mesh-size description of the PCM explored in Chapters 3 & 4. Analysis of the OFPAs and qPEAs revealed that the PCM has a varying mesh size (or correlation length), ranging from 100-500 nm. These fluorescent aggrecan studies demonstrate that these large (100 nm x 400 nm), highly charged molecules, can traverse the PCM without much difficulty. While the PCM acts like a sieve, preventing particles from fully penetrating through the coat, it is still passable to aggrecan, and hence possibly other desired molecules.

5.6 Possible mechanisms for cell coat expansion

With the results from the above fluorescent exg-aggrecan experiments in mind, we now return to the dynamic expansion of the PCM reported at the beginning of this chapter. Figure 5.13 summarizes the observation. When treated with exg-aggrecan at a concentration of 333 μg/ml, the PCM expands from an average of 7.9 μm before treatment (N=12) to an average 18.2 μm (N=21). Observation of this dynamic process using live cell microscopy and conventional particle exclusion assays revealed that the growth appears to have two distinct phases. A large amount of the growth occurs in the first ten minutes, as the coat grows from 7.9 μm to 12.3 μm, which is over 40% of the total growth. This fast growth, although not observed directly, is indicated by the dashed red line in Figure 5.13. This fast growth is followed by a slower expansion that requires one to two hours to finish, and is observed directly in the measurements outlined in Chapter 5.1.

The newly developed fluorescent aggrecan experiments presented in the above work are useful to clarify the possible mechanism responsible for the observed time dependent cell coat growth examined. The final PCM thickness at two hours is a function of concentration, as validated by both traditional and quantitative particle exclusion assays, as well as fluorescent aggrecan assays. Further, the maximum extension is achieved for concentrations of 333 μg/mL and higher according to the fluorescent aggrecan experiments, and at a slightly lower point (~182 ug/mL) according to PEA. This is consistent with rough estimates that the PCM should become saturated with aggrecan at concentrations above 1000 μg/mL (Chapter 3.2.4). The difference in these saturation points may arise from the fact that the HA may not require full saturation with aggrecan

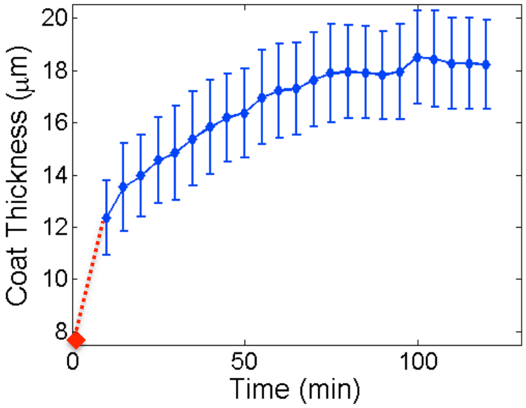

Figure 5.13 Averaged time dependent growth of the cell coat when exposed to exogenous aggrecan (N=21). The red point is the average size of the cell coat associated with RCJ-P cells before aggrecan treatment.

in order to stretch out to its max contour length, especially in a polymer brush like configuration like that found at the cell surface. Yet, in order for the aggrecan intensity to saturate, there must be no further binding sites. Hence it appears that at the concentrations used in the dynamic experiment, the matrix is fully stretched and completely saturated with aggrecan at the end of the two hour time period.

Furthermore, the fluorescent aggrecan experiments reveal that aggrecan can diffuse rapidly into the PCM and replace previously bound (exogenous) aggrecan on a time scale of minutes. This is slightly surprising given the difficulty small, passivated particles have diffusing into the same matrices. The qPEA results illustrate that 300 nm beads are unable to penetrate into the PCM of RCJ-P cells treated for 2 hours with 333 μg/mL aggrecan; yet rod-like semi-flexible aggrecan molecules are able to slip depp into the PCM and at high enough concentrations to rapidly replace 40% of the bright aggrecan within one minute, as detected by the reduction in intensity. After this first rapid turnover, the rest of the fluorescent aggrecan is replaced far more slowly, requiring a time scale of an hour.

The first stage of rapid PCM swelling occurs in at the most ten minutes, setting an upper bound on the process responsible for the observed rate of expansion. We have provided evidence that aggrecan diffuses into the PCM and binds to hyaluronan strands on the time scale of minutes.

The speed in which aggrecan initially becomes incorporated into the PCM should be similar, or possibly faster, when there is less aggrecan present in the PCM to begin with, as in the start of the reported dynamic swelling experiments. A lower density of aggrecan and a more open mesh in the PCM (as seen in both OFPA and qPEA experiments) should increase the rate of diffusion. The timescale to bind to the HA should also be increased since more binding sites will be available, increasing the probability of binding. The single process whose timescale has not been measured is the rate of extension of a HA polymer when it is suddenly bound by an aggrecan molecule (or several aggrecan molecules). We hypothesize that if the polymer strand is not entangled or hindered from extension, this rate should be almost instantaneous. In the early stages of the cell coat growth, especially at the edges of the PCM, we suspect that many binding sites on the PCM are available and that stretching is relatively unhindered in the dilute environment such that fast stretching can occur.

The slower regime of PCM swelling that follows the observed quick expansion could be a consequence of one or several different mechanisms. The data we have for the time scale of aggrecan diffusion into and binding to the PCM stems from the ‘bright to dark’ fluorescent aggrecan exchange experiments. Those experiments, however, occur in the context of a very different PCM, which has already been incubated in ex-aggrecan for two hours. We hypothesize that in the earlier stages when exogenous aggrecan initially encounters the PCM, at least three possible scenarios could lead to a slowed PCM expansion. First, if the HA strands are not fully stretched in the initial configuration it is possible that some binding sites along the strands are not easily accessible. The stretching of the HA strands as they are bound by the exg-aggrecan could lead to a feedback loop which stretches out the HA and makes more binding sites available. Then in turn additional aggrecan will bind, stretching the HA further, making more sites available. Via this mechanism, the HA strands that comprise the PCM would slowly stretch to reach their maximum contour length

A second possible scenario is also related to the inability of HA to fully stretch during its initial exposure to the additional aggrecan. If we imagine the PCM in the stage before exposure to exg-aggrecan, there will be numerous strands bound to the cell surface, stretching outwards to an average 8 μm. These strands, if they have the potential to be stretched further to an average 17 μm, will therefore possess another 9 um in slack distributed along the polymer chains. This slack would likely result in physical entanglements with neighboring chains. Therefore, if a sudden excess of ex-Ag were made available, after binding to the HA chains, a large stress could build up in the PCM, which would drive the slow unwinding of the entangled strands, where possible, and the eventual stretching towards a free energy minimum configuration. Depending on the degree of initial entanglements and the grafting density of the HA, the system may never fully reach its free energy minimum state.

The third possible mechanism for the slow PCM expansion accounts for the possibility that the added exg-aggrecan stimulates the cells to produce longer strands of hyaluronan. The hyaluronan synthase enzymes embedded in the cell's surface plasma membrane are capable of both producing new HA strands, and extending the currently bound HA. Although there have been no reports, to our knowledge, of proteoglycans like aggrecan stimulating hyaluronan synthesis, it is possible that addition exg-aggrecan initiates such a process. The maximum HA synthesis (from HAS2) has a synthesis rate estimated at 500 nm/min (70), well within the range of the expansion measured here. The fluorescent aggrecan replacement experiments combined with the fact that it takes at least two hours for our aggrecan swollen coats to fully grow indicate that it is possible that adding exg-aggrecan stimulates our cells to produce hyaluronan. Through some interaction, the exogenous aggrecan could further stimulates the HA synthase to produce more hyaluronan, growing the coat.

How aggrecan interacts with the cell on this level is not known. It's possible that the ability of aggrecan to sequester growth factors is responsible for this mechanism, and that the growth factors are responsible for this signaling pathway. It is also possible that the high charge density brought in by the exg-aggrecan stimulates synthesis of longer HA (71). Further, the turn-on time for HA synthase also unknown. The steady state growth has been measured at a maximum of 500 nm/min, but how long it would take the synthase to start this production is unknown. Future work is currently being developed to possibly measure the production of hyaluronan in the presence of exogenous aggrecan. It is possible to measure the mass, and thus length, of hyaluronan via gel electrophoresis. In these experiments one would compare the distribution of lengths of HA on control cells to the distribution on cells that have been treated with exogenous aggrecan.

Another experiment currently underway to investigate the possibility of hyaluronan growth measures the real-time distribution of HA when exposed to exg-aggrecan. Here, GFPn (which fluorescently labels HA) is added to the cells and allowed to incubate for 2 hours, resulting in an intensity profile that is representative of the overall hyaluronan distribution. Exogenous aggrecan is then added while the distribution of GFPn is measured over time. Simple stretching of the individual hyaluronan strands that comprise the cell coat would cause the GFPn profile to flatten and be stretched outward as the bound GFPn molecules would be spaced further apart and move with the HA to positions further away from the cell. In addition, growth of HA would shift the peak and distribution of the GFPn as the newly produced HA would be unlabeled and would push the labeled HA outward. These experiments could therefore play an integral role in determining how exogenous aggrecan stimulates the enlargement of the PCM.

5.7 Summary

The results presented in Chapters 3&4 led to a proposal for the specific way the addition of exg-aggrecan modifies the underlying structure of the PCM. The results presented in this chapter take the next step towards understanding how this process actively modifies the pericellular matrix. The dynamics of cell coat growth and modification were examined both with traditional PEAs, as well as with innovative fluorescent exg-aggrecan studies in order to examine this mechanism.

The time dependence of the cell coat enlargement was studied with the use of traditional PEAs. An extended exclusion zone around the cells was created almost immediately after the cell coats were exposed to exg-aggrecan, and their thickness was measured continuously for two hours. Interestingly, a large portion of the swelling occurred within the first ten minutes of exposure, suggesting that their environment can rapidly change the coats. After this time, the coats continued to grow for approximately the next hour, although at a much slower rate.

Labeling the exg-aggrecan fluorescently allowed us to examine where the newly introduced aggrecan bound itself within the PCM. It was observed that the exg-aggrecan is able to bind everywhere within the cell coat, and does so at a higher concentration just outside the cell membrane. The coat appeared to be saturated when incubated at a concentration of 333 μg/ml, a value lower than would be expected from previous studies of HA-aggrecan systems. These results pave the way for future experiments where the native aggrecan can be completely removed, followed by incubation with exg-aggrecan. This would allow for measuring the distribution of the full amount of aggrecan within the coat, being the first study of its kind.

The profiles of bound exg-aggrecan were also observed in dynamic systems. After the cell coat reaches equilibrium during exposure to exg-aggrecan, we observed that replacement of the exg-aggrecan solution with aggrecan free media caused the bound exg-aggrecan within cell coat to slowly erode. The erosion is slower than would be expected for an ideal system, and is not as significant. Further, it was observed that replacing a solution of labeled exg-aggrecan with that of unlabeled exg-aggrecan caused a quick reduction in the quantity of the pre-bound exg-aggrecan. The unlabeled exg-aggrecan in solution is able to quickly replace much of the fluorescent aggrecan, corroborating the result observed above that the PCM is able to be rapidly modified by a changing environment, specifically by different aggrecan concentrations.

Developing methods to study the length and distribution of the bound hyaluronan are currently being investigated, and will help determine the method by which the addition of exg-aggrecan dynamically modifies the PCM. Our belief is that the above results combined with a full measurement of hyaluronan production, as well as observations from the qPEA and OFPA assays, will bring about a complete understanding of the ways in which the cell can regulate the PCM.

CHAPTER 6

CONCLUSIONS AND OUTLOOK

The pericellular matrix is a neglected but important construct of single cells. A growing body of evidence suggests that the mechanical and structural properties of this cell associated matrix influence numerous physiological processes. Meanwhile, researchers working in bioengineering (27) and drug delivery (33) are increasingly concerned with the influence of and possible opportunities to manipulate the PCM to realize their applications. Similar to other passive and active microrheology approaches used to interrogate the viscoelastic properties of cells (39, 72-76), in this work we introduce several complementary assays in order to non-destructively interrogate the mechanics and organization of the pericellular matrix. Optical force probe measurements show that pericellular matrix is a robust yet malleable structure. The PCM tolerates repeated probing with a three-micron particle without any measurable changes. Fluorescence imaging of the PCM during optical-manipulation of probe particles shows that the PCM appears to rearrange around entrant particles. This is further supported by dual holographic optical tweezers experiments that verify that matrix recovers behind a particle such that it exerts similar forces on a secondary bead. Observation of the rearrangement of matrix around the second probe particle as well as the observation that the first probe does not feel a force as the second moves inward is evidence in support of the ultrastructural insight that the PCM of this chondrocyte cell line is *not* crosslinked.

The speed of experimentation enabled by dynamic force assays allows for real-time measurements of PCM changes during quick processes, such as cell migration and cell mitosis where the PCM is rapidly modified. The dynamic force probe measurements of PCMs altered with exogenous aggrecan illustrate how the optical force probe approach will be useful for future time-dependent studies of PCM transformation. Although study of an individual PCM probed both before and after exogenous aggrecan treatment will provide the most precise understanding of the nature of these changes, the averaged data presented here already provide useful information on how aggrecan modifies the PCM and yields clues concerning the availability of binding sites along the HA chains.

Combined analysis of the dynamic and equilibrium OFPA measurements suggests that the PCM on RCJ-P cells has two distinct spatial regimes, consistent with other studies of the same cell line (7). There is an inner region capable of exerting an equilibrium force on external objects and a more diffuse outer region that is easily penetrated by objects with three microns and smaller. The inner region is delimited by an edge located at ~6-8 μm, as detected by both the dynamic and equilibrium force experiments. Quantitative particle exclusion assays (qPEA) also indicate this distance (~8.5 μm) as a unique position in the PCM, a position that particles (diffusing in solution) with diameters of 500 nm or greater do not penetrate. The outer region of the PCM is detectable only by dynamic optical force probe measurements, where our measurements consistently confirmed its presence. Indeed, the dynamic force measurements reveal that the pericellular matrix extends much farther (40%) from the cell surface of RCJ-P cells than previously detectable. The ultra-sensitivity of dynamic force probe measurements stems from the viscous component that is not present in equilibrium measurements.

Analysis of the equilibrium force measurements led to the original proposition that the PCM must possess a spatially varying correlation length. We further investigated this prediction by developing a novel quantitative particle exclusion assay to look at the size dependent distribution of (passivated) particles into the PCM. Those measurements corroborated the optical force probe data, roughly confirming that the length scale and exponential increase of the mesh size is accurate. Hence, to the best of our knowledge our assays provide the first quantitative evidence that the mesh size of the pericellular matrix varies with distance to the cell surface. The spatial and chemical variations in the cell coat will greatly influence the transport of objects and molecules to and from the cell surface. In these studies, we have minimized the role of chemical interactions to focus on steric exclusion. The outcome demonstrates that that even without chemical interactions or electrostatic repulsion expected to occur in the highly negatively charged matrix due to proteoglycans, access to the cell surface is affected by cell coat ultrastructure. This has direct implications for cell defense against viral and bacterial infections (3), drug delivery applications (33), and the signaling between cells with proteins such as growth factors (27).

In addition, modified cell coats were studied in order to understand regulation of cell coats by changes in their environment. The PCMs were modified by addition of exogenous aggrecan, as the added aggrecan binds to the available hyaluronan in the cell coat, modifying the PCMs size and interior structure. The above OFPA and qPEA experiments were brought to these modified coats, determining that the aggrecan filled up the empty spaces within the cell coat, ‘tightening’ the average spacing or mesh size within the coat. Further, fluorescent microscopy studies were developed in order to study the quantitative changes in bound exg-aggrecan in the modified coats. The profile of bound exg-aggrecan was measured from the fluorescent images, providing for the first time a direct measurement of exactly how the addition of exg-aggrecan modifies the interior structure of the PCM. As for the dynamics of these modified coats, traditional PEA studies as well as results obtained from the fluorescent labeling of exogenous aggrecan determined that the majority of this modification occurs on a ten minute time scale, providing evidence for the potential of cell coats to be rapidly modified by their environments. In the future, the full battery of experiments and analysis developed in this work can be applied to cells undergoing natural pericellular matrix transformations in order to determine how the cell coats are modified during these possesses, and why this modification is crucial for these mechanisms.

The work presented in this thesis can be seen as a launching point to investigate many properties of the pericellular matrix that are currently either ignored or completely unknown. While the present work focused mainly on the static coats of rat chondrocyte cells, as is outlined in the introduction the PCM is known to be important for a bevy of different cell types and for different cell processes. It is our vision that the methods and insights presented in this thesis will provide concrete routes forward to studying how the physical properties of the PCM influence and possibly direct processes such as cell division, migration, cancer metastasis, and embryogenesis.

While the work presented here was performed exclusively on rat chondrocyte cells, our interest in not limited to these cells in particular. They were chosen due to the fairly large size of their coat, making them a useful cell model with which to develop new tools and methods. However as outlined above, the pericellular matrix is present on a wide range of cells, and is important for many different processes in which its role has so far been ignored. To that end, we have started preliminary studies investigating the

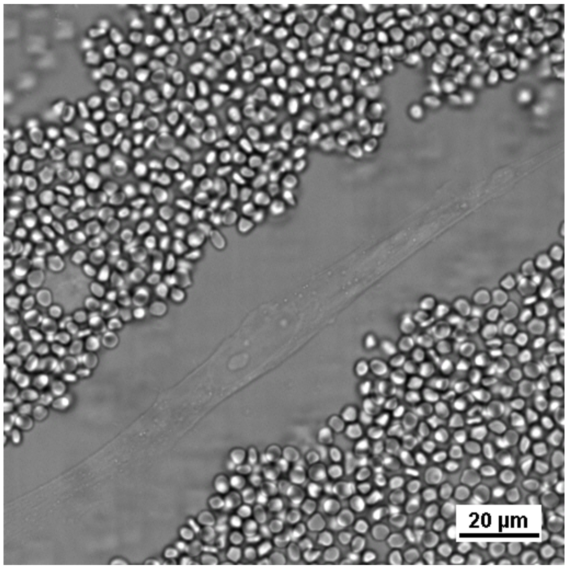

Figure 6.1 Human mesenchymal stem cell visualized via bright field microscopy. A standard particle exclusion assay is used to show the existence of a large pericellular matrix.

structure of the pericellular matrix on human primary mesenchymal stem cells (MSCs). Mesenchymal stem cells are multipotent connective tissue cells, meaning they can differentiate into a range of different cell types which here include chondrocytes, osteoblasts (bone cells), and adipocytes (fat cells). Since these MSCs are a progenitor to chondrocytes, the cells studied in this thesis, it is perhaps not surprising that they themselves have a large natural pericellular matrix. For the MSCs obtained for our study, they had coat size of 6.6 +/- 0.4 μm as measured with a traditional PEA, which is comparable to the size of the rat chondrocytes (7.0 +/- 0.5 μm).

Further we were able to swell the size of these mesenchymal stem cells, just as in the case of the rat chondrocytes (Figure 6.2). While the coats started out at a similar size, the chondrocytes were able to be swollen to a much larger degree than are the MSCs. However it is still possible that the coat of the mesenchymal stem cells can be swollen

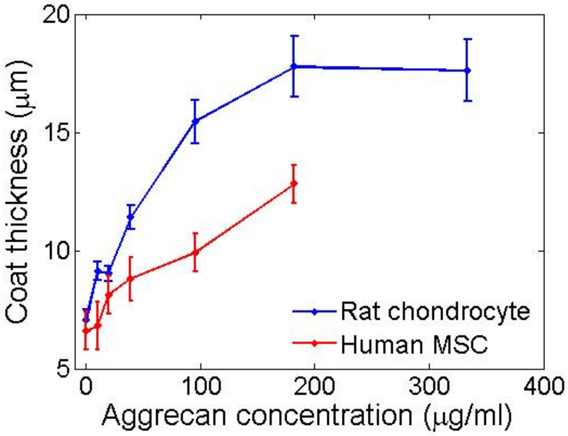

Figure 6.2 Exogenous aggrecan is able to swell human mesenchymal stem cells in addition to the rat chondrocytes. For the concentrations used the MSCs were not swollen to the same degree as the RCJ-Ps, however the growth is still substantial.

futher with the addition of higher concentrations of exogenous aggrecan, given that the preliminary data does not clearly plateau.

The ability of aggrecan to bind and sequester growth factors, and the fact that the pericellular matrix could act as a reservoir for these growth factors hint at a possible mechanism for the PCM being an important regulator of stem cell differentiation. Modification of the cell coat, and thus the growth factors found within that coat, could be a vital tool for controlling and regulating stem cell differentiation.

Further, many of the studies presented in this thesis have direct follow-up studies that will lead to a greater understanding of the pericellular matrix Both the developed optical force probe and quantitative particle exclusion assays can be used on other cell types, and on cells undergoing physiological changes in order to study how cell coats change during these processes. The fluorescent exogenous aggrecan studies present a novel way in order to directly study the distribution of aggrecan within the coat provide an illuminating comparison to the OFPA and qPEA studies which have measured this same distribution. Expanding on the current studies will also result in an understanding of how the cell coat swells and is modified by the addition of exogenous aggrecan, as well as coats that are modified directly by the cells in other processes. Further development and use of biological tools will allow us to directly measure the concentration and length of hyaluronan produced by the cells, and will be useful to reveal the method by which cell coats are modified both when exposed to exogenous aggrecan, and in physiological processes.

The goal of this work was to study the structure, form, and mechanics of the pericellular matrix through a variety of biophysical tools. This work produced discoveries about the pericellular matrix that have never before been seen, and resulted in knowledge that is vital to anyone studying the pericellular matrix or any of the multitudes of processes in which it is important. A sharper focus on an often ignored structure (the PCM) provided not only direct and novel insight into this structure, but also new tools to begin to address longstanding questions about the cell coat. In addition to the development of biophysical tools this work led to a rare connection between polymer physics and a known biological system, as well as to nascent research projects which will further advance the study of the PCM. We hope that the efforts put forth here will both raise awareness about the importance of the pericellular matrix, and to lead to further discoveries that will prove to be vital to the burgeoning field of biophysics.

APPENDIX A

DERIVATION OF CORRELATION LENGTH CALCULATION

The relationship between the equilibrium force and the local pressure on the bead is represent by

$$\vec{F}_{osm}(z) = \int P(z')\, d\vec{A} \qquad \text{Eq A.1}$$

where P is the pressure, z is the distance from the cell membrane to the center of the bead, and z' is the distance to the outside of the bead, as illustrated in Figure A.1.

Since the pressure acts in the inward radial direction on the bead, we rewrite Eq. A.1 as

$$\vec{F}_{osm}(z) = -\int P(z')\, dA\hat{R} \qquad \text{Eq. A.2}$$

Considering that the experiment is symmetric in every direction but z, we rewrite the above as

$$\vec{F}_{osm}(z) = -\int P(z') \cos\theta\, dA\hat{z} \qquad \text{Eq. A.3}$$

Replacing z' with $z' = z - R\cos\theta$, where θ is the standard spherical coordinate, gives

$$\vec{F}_{osm}(z) = -\int P(z - R\cos\theta) \cos\theta\, dA\hat{z} \qquad \text{Eq. A.4}$$

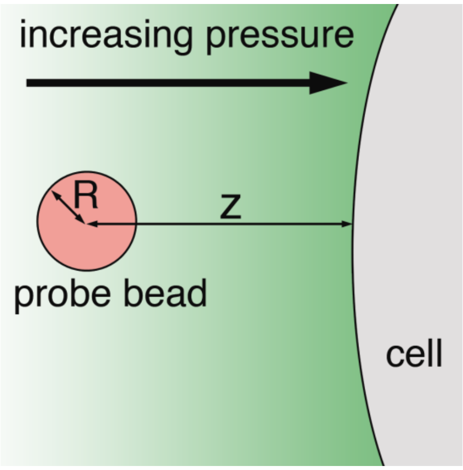

Figure A.1 Schematic of osmotic pressure gradient on a bead as a result of a varying concentration (green) in the cell coat.

where R is the bead radius. Integrating the surface element dA over r and φ gives $dA=2\pi R^2\sin\theta d\theta$, since their contributions are constant and independent of θ. This results in

$$\vec{F}_{osm}(z) = -\int_0^{\pi} P(z - R\cos\theta)\, 2\pi R^2 \sin\theta\cos\theta\,\hat{z} \qquad \text{Eq. A.5}$$

Setting x = R$\cos\theta$, the force becomes

$$\vec{F}_{osm}(z) = -2\pi \int_{-R}^{R} P(z-x)\, x dx \hat{z} \qquad \text{Eq. A.6}$$

Now, Taylor expanding $P(z\text{-}x)$ around z

$$P(z-x) = P(z) - \frac{\partial P(z)}{\partial(z-x)}x + \frac{1}{2}\frac{\partial^2 P(z)}{\partial(z-x)^2}x^2 - \frac{1}{6}\frac{\partial^3 (P(z)}{\partial(z-x)^3}x^3 + \frac{1}{24}\frac{\partial^4 P(z)}{\partial(z-x)^4} + \cdots$$

Eq. A.7

and using $z' = z - x$ and the chain rule which gives $\frac{\partial P(z)}{\partial z'} = \frac{\partial P(z)}{\partial z}\frac{\partial z}{\partial z'}$ where $\frac{\partial z}{\partial z'} = 1$,

the integral for the force becomes:

$$\vec{F}_{osm}(z) = -2\pi \int_{-R}^{R} \left(P(z) - \frac{\partial P(z)}{\partial (z-x)}x + \frac{1}{2}\frac{\partial^2 P(z)}{\partial (z-x)^2}x^2 - \frac{1}{6}\frac{\partial^3 (P(z)}{\partial (z-x)^3}x^3 + \frac{1}{24}\frac{\partial^4 P(z)}{\partial (z-x)^4}\right) x dx \hat{z} \quad \text{Eq. A.8}$$

Due to the limits of integration, the terms odd in x above drop out yielding

$$\vec{F}_{osm}(z) = \frac{4}{3}\pi R^2 \left(\frac{\partial P(z)}{\partial z}R + \frac{\partial^3}{\partial z^3}\frac{1}{10}R^3 + \cdots\right)\hat{z} \quad \text{Eq. A.9}$$

Assuming that the solution for the pressure has an exponential dependence

$$P(z) = he^{-dz} \quad \text{Eq. A.10}$$

and using the experimental observation that the equilibrium force has an exponential dependence with known parameters a and c,

$$F_{osm}(z) = ae^{-cz} \quad \text{Eq. A.11}$$

we can solve Eq. A.9 to find an approximate solution for the pressure. It is apparent that d=c, while the relation between a and c is found to be

$$a = \frac{4}{3}\pi R^2 h \left(cR + \frac{1}{10}(cR)^3 + \cdots \right) \qquad \text{Eq. A.12}$$

Since we know that c=0.5 and that R=1.5, we have cR = 0.75. This gives $0.1(cR)^3$=.04 and therefore we can neglect the 3rd and higher order terms. The final approximate expression for the pressure profile is

$$P(z) \sim \frac{3a}{4\pi R^3 c} e^{-cz} \qquad \text{Eq. A.13}$$

To check the approximations made above, we can take a slightly different approach starting from

$$\vec{F}_{osm}(z) = -2\pi \int_{-R}^{R} P(z-x)\, x dx \hat{z} \qquad \text{Eq. A.14}$$

If we assume that the pressure has an exponential form (Eq. A.10), we can solve for the exact expression for the pressure:

$$F_{osm}(z) = \frac{2\pi h}{d^2} \left(e^{dR}(dR-1) + e^{-dR}(dR+1) \right) e^{-dz}. \qquad \text{Eq. A.15}$$

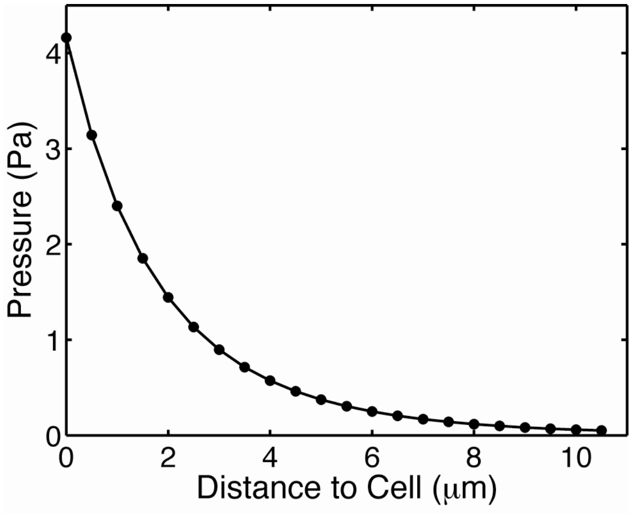

Figure A.2 Pressure profile of the coat using the approximate solution in Eq. A.13 and the parameters (a,c) acquired from optical force probe assays.

Considering that from the data the equilibrium force has an exponential dependence with known parameters a and c, we can solve for the parameters d and h to find the pressure:

$$ae^{-cz} = \frac{2\pi h}{d^2}\left(e^{dR}(dR-1) + e^{-dR}(dR+1)\right)e^{-dz}. \qquad \text{Eq. A.16}$$

Again we find that d=c. Solving for h yields the an exact expression for the pressure profile throughout the pericellular matrix,

$$P(z) = \frac{ac^2}{2\pi\left(e^{dR}(dR-1)+e^{-dR}(dR+1)\right)}e^{-cz} \qquad \text{Eq. A.17}$$

This exact solution can be compared with the first order solution (Fig. A.3), verifying that it is sufficient to use the first order approximation (Eq. A.13) for the pressure profile.

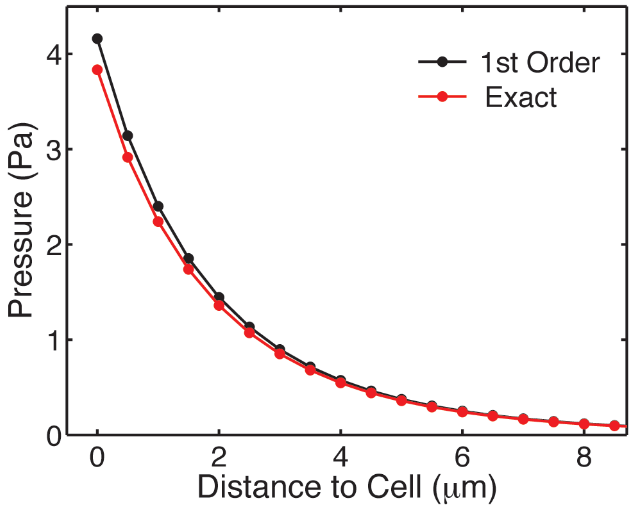

Figure A.3 Comparison of the first order solution (Eq. A.13) to the exact solution (Eq. A.17) for the pressure profile in the pericellular matrix, where to find Eq. A.17 it was assumed that the pressure has an exponential profile.

This expression can then be used to relate the pressure profile to the correlation length versus distance to the cell surface throughout the pericellular matrix:

$$P(z)\sim\frac{k_BT}{\xi^3(z)} \qquad \text{Eq. A.18}$$

giving a correlation length profile with an exponential variation in space,

$$\xi(z) \propto e^{\frac{cz}{3}} \qquad \text{Eq. A.19}$$

In order to determine the error in the calculation of the correlation length, the uncertainty in the equilibrium force measurement must be propagated. Since the error in the pressure profile is not known, we must first put the correlation length as a function of the equilibrium force

$$\xi(z) = \left(\frac{k_B T}{P(z)}\right)^{1/3} = \left(\frac{k_B T 4\pi R^3 c}{3F(z)}\right)^{1/3}. \qquad \text{Eq. A.20}$$

Then in order to calculate the uncertainty in correlation length, δξ, we take the derivative of the correlation length as a function of the equilibrium force, and multiply this value by the uncertainty in the measurement of the equilibrium force

$$\delta\xi(z) = \left|\frac{d\xi(z)}{dF(z)}\right| \delta F(z) = \frac{1}{3}\left(\frac{k_B T 4\pi R^3 c}{3}\right)^{\frac{1}{3}} F^{-4/3}(z)\delta F(z), \qquad \text{Eq. A.21}$$

assuming that the error in the bead position, z, is negligible. This calculation gives us the uncertainty shown in Figures 4.6 and 4.12. For the data shown, the values for the equilibrium force as a function of position, *F(z)*, was determined from an exponential fit of the experimental data for F_{eq}. The error in F_{eq} was then calculated as twice the standard error from the fit of each individual data set. This procedure allows us to calculate the correlation length at every position inside the PCM, rather than just where the equilibrium forces were measured.

APPENDIX B

EXTRACTING FORCE CURVES FROM HOT EXPERIMENTS

Optical tweezers (OT) are widely appreciated for their applications in micromanipulation (77-79), as well as for their ability to make sensitive force measurements (80). When used for force sensing applications, the trap is typically used in the harmonic regime where small displacements from equilibrium of a trap-bound particle are linearly proportional to the external force, scaled by the trap's stiffness. Force measurements have been realized both with a device-steered optical trap (81) as well as with a fixed optical trap coupled with a stage that translates the sample (82). In other applications, a fixed optical trap coupled with another micromanipulation device such as a micropipette (83), has been implemented. In all three of these standard measurements, the trap's intensity distribution and hence its optical potential energy landscape is nearly constant, where one can ignore or compensate for minor changes during displacement.

An alternative, increasingly popular method to effectively steer an optical trap and its cargo, is to use a computer-addressable diffractive optical element such as a spatial light modulator (SLM) (84-85) or a micromirror array (86). Displacement of a trapped particle from one position to the next is achieved by altering a phase mask (kinoform), which results in the disappearance of the trap holding the particle at position **r**, and the appearance of a new trap at a distance **r**+Δ**r** (87). The discrete translation of a holographic optical trap (HOT) leads to time- and spatially-dependent intensity variations of the translating trap (Figure B.1a) (88). This can significantly affect the dynamics of the accompanying particle, which moves from one HOT to the next as it relaxes into the new potential energy minimum (Figure B.1b, Figure B.2). Nevertheless, HOT has proven a useful tool, particularly in the area of micromanipulation (89-92) since it can easily produce and move dozens of optical traps in arbitrary configurations in 2D and with significant flexibility in 3D, where each trap can be independently programmed with a non-conventional mode structure (79, 85, 93).

Less work has focused on using HOTs for force measurements. It is apparent, however, that the flexibility and complexity allowed for by a HOT setup could facilitate force measurements, particularly in biological studies (94-102). Measuring forces with a fixed HOT is similar to working with a conventional OT, where particle displacements are related to force using the calibrated trap stiffness (103). It is more difficult to use a discretely translating HOT to both exert force and measure the reaction forces of the system. Mejean and co-workers interactively updated the positions of multiple HOTs to study mechanical coupling of a particle to the F-actin cytoskeleton in a neuronal growth cone (101). In those closed-loop measurements, the HOT position was fine-tuned every 0.1-0.3s to maintain a constant position or force on a bead anchored to the growth cone, successfully realizing both a HOT-based position clamp and a force clamp. In another ground breaking experiment, Farré and co-workers (104) used two dynamic HOTs (one translating, one fixed but updated) to stretch DNA and accurately measure DNA's well-known force versus extension curve. During measurement, the DNA remains in equilibrium because the molecule's relaxation dynamics are much faster than the stretching speed of the HOTs. This made it possible to measure a purely elastic, rather than viscoelastic response.

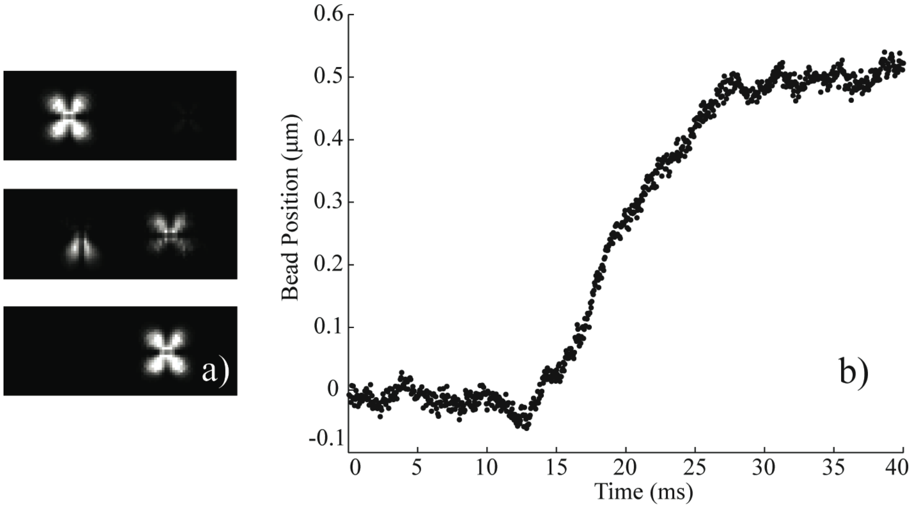

Figure B.1 (a) Intensity modulation arises during the update of the position of a HOT. The transition from projecting one kinoform to the next on the spatial light modulator (SLM) leads to a spatially-dependent fading-out of the original HOT and the concurrent fading-in of the updated HOT, both from top to bottom. Analysis of the integrated intensity reveals that an updated HOT blossoms into its full intensity distribution in approximately ~30 +/- 5 ms. (b) Typical trajectory of a 3μm diameter microsphere as it is transferred from one HOT to another 500 nm away.

These experiments set the stage for the future of HOT-based force measurements. Yet, it is notable that not all external forces can be measured using discretely translating HOTs. For example, consider using an OT to measure the hydrodynamic drag on a spherical particle. Stokes drag is such a commonplace force, that it is often used to calibrate the stiffness of optical traps. However, if one tries to measure it with a discretely translating HOT, no force is detectable (Figure B.3) despite the visible motion of the particle through the fluid. Clearly, this result depends on the approach: the most manageable and only established analysis (104) avoids the difficulties associated with time-dependent force fields. Within that framework, the Stokes drag cannot be observed because at the moment of the measurement, the drag force has already decayed to zero. This highlights a significant difference between standard OT and discretely translating HOT force measurements: standard OT measurements are performed when the particle is traveling at a well-defined speed. Translating HOT force measurements take place when the particle is not moving.

The observation that viscous forces are immeasurable by a translating HOT, while purely elastic forces in an equilibrium system are accurately extracted, raises questions about measurements of viscoelastic materials. The frequency-dependent responses of these systems will complicate interpretation of experiments. In this work, we explore what forces a translating HOT is capable of measuring in a viscoelastic biomaterial by comparing the force curves generated by standard OT-stage versus a translating HOT.

B.1 Particle dynamics in a translating HOT: Extracting a force curve

This section describes the simplest approach to extracting a force curve from the dynamics of a particle hopping along with a translating HOT. A typical trajectory for a particle as it is carried through a Newtonian fluid by a discretely translating HOT executing 500 nm steps is illustrated in Figure B.1.2. The particle's position at each time point cannot simply be related to the external forces, as it can be for a standard OT measurement (105) (Figures B.1.3a, B.1.4a). However, in the plateau regions, when the trap intensity is constant, the particle's position can be used to estimate external forces. More precisely, to extract a force curve from a translating HOT, a high speed video sequence is recorded of the particle as it is shifted in position by a series of kinoforms projected to the SLM. The position of the particle is then evaluated and plotted versus time, giving rise to a staircase-shaped plot like the one in Figure B.1.2. The extent of each plateau is identified with an automated MATLAB program. A single data point for the position, x_i, of the particle associated with each HOT (kinoform) is extracted for every

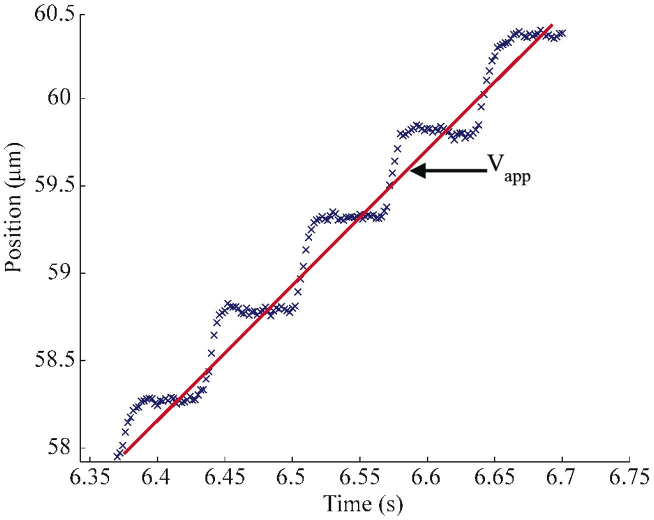

Figure B.1 Dynamics of a particle carried by a translating HOT through a Newtonian fluid, phosphate buffer solution (PBS). The flight of the particle from one position to the next occurs during the update of the new optical trap. The kinoforms were updated once every ~0.07s to adjust the apparent speed of the translating particle to v_{app}~7.1 μm/s, indicated by the slope of the line.

plateau by averaging over the data. The result is a series of equilibrium positions (or out-of-equilibrium positions, if it the material has not relaxed) of the particle in the translating HOT at designated positions throughout the material.

To calculate the force on the particle at each point, the standard $F = -k_i((x_i-x_{0i})$ is used where, k_i and x_{0i} are predetermined in control experiments for each kinoform ranging from $1<i<N$, where N is the total number of steps. The magnitude of the particle's displacement at each position can be illustrated by plotting the control displacement curve (from the control measurement) versus the data taken in the medium of interest (Figure B.1.4b). For this particular material (described in detail below), the shifts in the plateaus are apparent and they increase as the probe is carried through the medium, indicating increasing force.

B.2. Particle speed in a translating HOT

Using a translating HOT to extract a force curve is complicated by the desire to make measurements at a well-defined velocity. This requirement may be especially critical for viscoelastic materials, which can have a velocity-dependent response. Yet, the speed of a particle in a translating HOT varies with time and is difficult to control during the transition from one kinoform to another. Here we introduce two definitions of the average speed of a particle in a translating HOT. A simple approximation of the apparent particle speed, v_{app}, can be determined by extracting the slope of the particle position versus time (Figure B.2). This is approximately the step size divided by the update time of the kinoforms, giving an apparent speed of $v_{app}= \Delta x/\Delta t_{update}$. While this appears to be a reasonable estimate of the speed since the position of a translating particle in water is accurately predicted using this speed, it is in fact not a good representation of the speed at which the material is probed. This probing speed can be estimated more accurately by counting the number of frames recorded during the transition from one trap to the next (i.e. between the plateaus) to get an average transit velocity of $v_{transit}= \Delta x/(N_{frame}*t_{frame})$, where $t_{frame}= 1/fps$, is the duration of one frame and fps is the frame rate of the camera.

In the experiments presented in this work, the translating HOT step size and update time were selected to produce particle speeds similar to those in the standard stage measurements reported (all OT-stage experiments were performed at ~ 8.3 μm/s). Measurements were made using both 500 nm and 250 nm step sizes. Choosing a kinoform update rate of ~14.3 Hz (i.e. Δt_{update}~0.07 s between kinoforms), the apparent speed is v_{app} ~ 0.5 μm/0.07 s ~ 7.1 μm/s and the transit speed is $v_{transit}$ ~ 0.5 μm /(12*1/500 s) ~ 20.9 μm/s for the 500nm steps. For the 250nm steps, v_{app} ~3.57 μm/s and

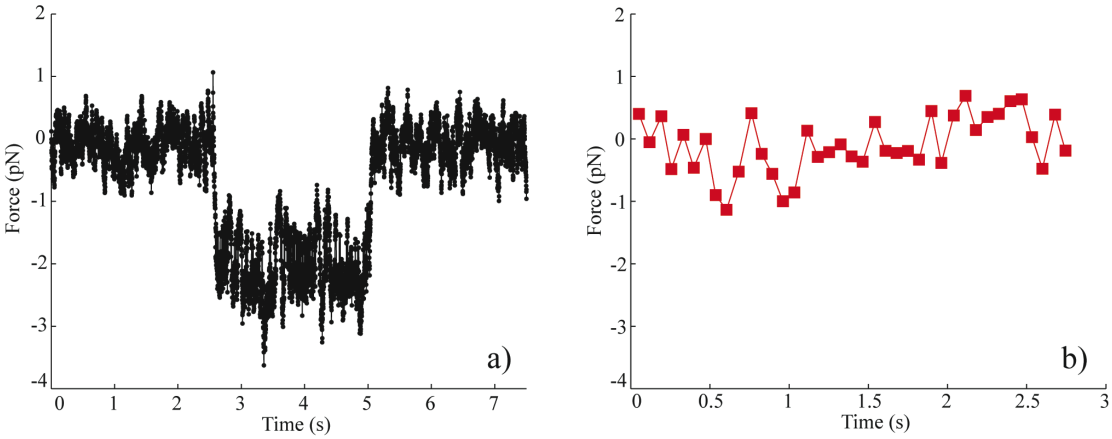

Figure B.3 (a) A non-zero hydrodynamic drag force is measured on a particle in a fixed OT when a stage moves during the time period of ~2.5-5 seconds at 8.3 μm/s. (b) Force measured on a particle in a translating HOT moving at a speed of v_{app}~ 7.1 μm/s. The average force is zero.

$v_{transit}$ ~ 10.4 μm /s (since N_{frames} ~ 12 for Δx=250nm and 500nm). As discussed below, careful study of the particle dynamics in our experiments reveals that such approximations are inappropriate in spatially inhomogeneous media or any scenario where the material's resistance changes with position. In such cases, the transit time, N_{frame}*t_{frame}, from one HOT to the next varies with position, giving rise to a position-dependent speed.

B.3 Measuring hydrodynamic drag force: Standard OT versus translating HOT measurements

Here we apply the above protocol to compare a measurement of hydrodynamic drag on a particle in a fixed OT-stage experiment, with the force data extracted from a translating HOT. Measuring the Stokes drag on a microsphere in a Newtonian fluid is straightforward with a standard optical trap. The hydrodynamic drag of a simple, infinite fluid on a spherical particle of radius, a, in a Newtonian fluid of viscosity, η, scales linearly with the speed, v, with which the fluid flows past the particle, $F_{drag}=6\pi\eta va$. In a calibrated OT, moving the fluid past the confined bead with a stage or equivalently, smoothly translating the standard OT at a given speed displaced the particle from the trap's equilibrium position. The particle's final position depends on the balance between the trap's restoring force with the Stokes drag (105). Figure B.1.3a shows the force on an optically-trapped 3 μm particle before and after the sample (50% glycerol/water vol.) is moved past the microsphere by the stage at ~8.3 μm/s. The stage motion begins at approximately after 2.5s has passed, and the hydrodynamic drag force on the particle almost instantaneously shifts the particle to a new equilibrium position in the trap.

Figure B.1.3b shows the extracted force versus time of a HOT-translated particle in the same fluid. Each new HOT was updated at a position 500 nm away from the last, where the kinoforms were updated every 0.07s. Some fluctuation of the measured force about zero is visible, but it is similar to the magnitude of fluctuations seen in the fixed OT-stage experiment before the stage begins to move. At first glance this result seems odd, since the particle is detectably being translated at an apparent velocity of 7.1 μm/s. Yet, as the HOT intensity stabilizes, viscous dissipation slows the particle to a stop in the absence of an external force field. Hence, during the actual measurement time, the particle is no longer in motion and the measured Stokes drag is zero.

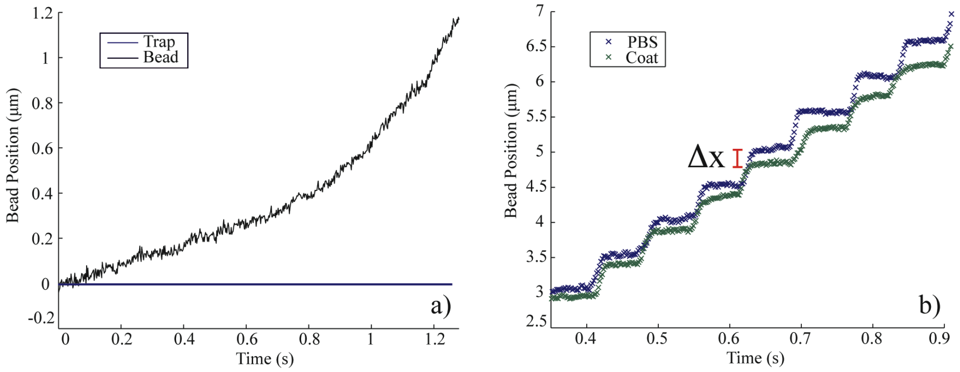

Figure B.1.4 (a) Bead position in a fixed OT as the stage translates the cell coat towards the trapped bead. The bead experiences a displacement from the trap's fixed position indicated by the theoretical solid line. (b) Particle dynamics in a translating HOT in pure media (top) versus a section of the cell coat (bottom). The observed displacement of the particle from the HOTs' equilibrium positions (represented by plateaus in PBS) indicates a growing force on the particle as it is carried into the cell coat.

B.4 Force measurements in viscoelastic media

B.4.1 Experimental protocol for probing the cell coat

Our viscoelastic system is the pericellular coat (Figure B.5a). This thick polymer matrix is attached to the surface of many cell types (3), and its physicochemical properties (2) are important in numerous physiological processes including cell migration, proliferation, metastasis, and embryogenesis. The force curve displayed in Figure B.5b was produced by a standard mechanical measurement of the pericellular coat using a fixed OT and a moving stage. The force on the bead clearly increases as the particle is pushed into the cell coat. In a typical experiment, a 3μm bead is trapped outside of the cell coat. The stage then smoothly translates the cell sample at 8.3 μm/s towards the trapped bead, normal to the cell's surface. Probing the cell coat consecutively with the same bead produces similar force curves (with small differences), suggesting that

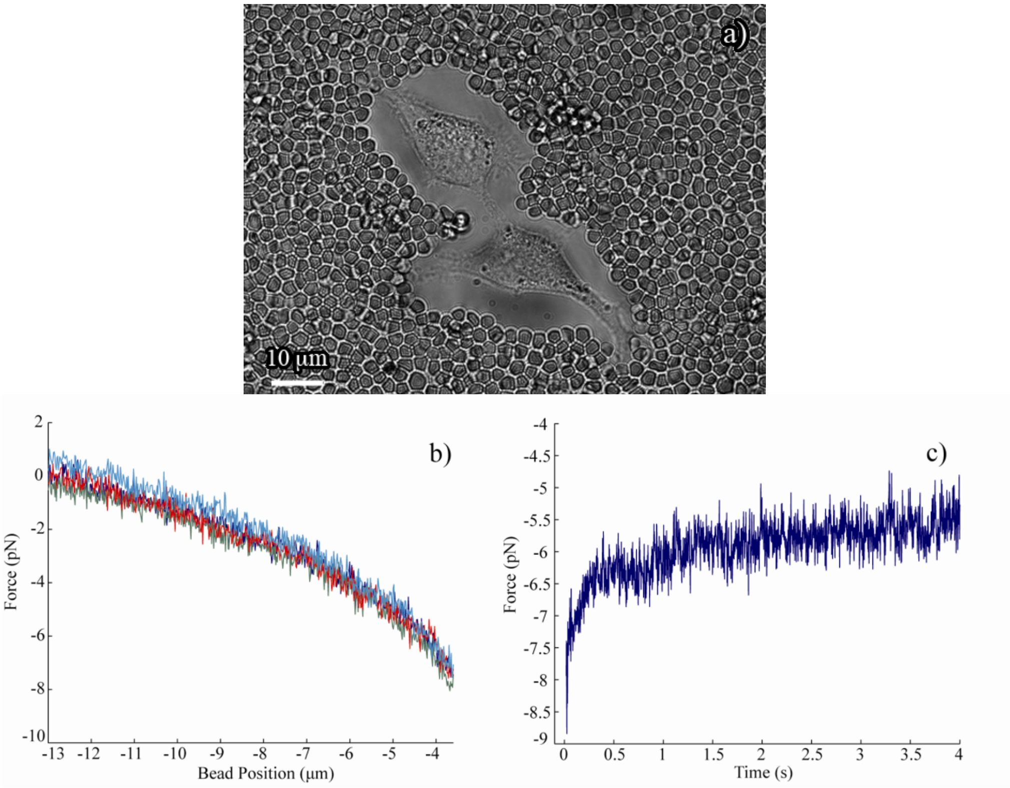

Figure B.5 (a) A particle exclusion assay (PEA) visually illustrates the physical extent of the pericellular coat. (b) Force versus position in the cell coat experienced by a microsphere trapped in a fixed OT while the microscope stage smoothly translates the cell towards the bead. Position reflects the distance to the cell surface. In this experiment, the bead was translated from a distance of 22 μm to 4 μm from the cell surface at ~8.3 μm/s. The colors designate different advances of the bead into the cell coat, in the order of dark blue, red, green and teal blue. (c) The force measured at the point closest to the cell surface relaxes after the stage stops moving during a 5 second pause. This plot corresponds to the relaxation of the first illustrated probing event (dark blue) shown in b).

the probing does not significantly change the coat. It also indicates that one probing event can be conveniently compared with the next, for a given cell. After moving through the 10-20 μm thick cell coat, the stationary OT is stopped 3 μm from the cell surface to avoid contact with microvilli. Our extensive investigations with a standard OT-stage setup have demonstrated that this polymer matrix is viscoelastic. This is evident in the velocity dependence of the force curves generated with a fixed OT-stage setup. Viscoelasticity and its frequency-dependent response is also the source of the relaxation seen in the position of a trapped bead after the stage has pushed it through the coat and positioned it at rest near the cell surface.

Force measurements were performed consecutively on a given cell with the same bead to allow direct comparison of the data produced using a translating HOT. A typical experiment involved probing the cell three times using a fixed (but holographic) optical trap using a pre-programmed stage, followed by three more probing events with a dynamic HOT programmed using a series of kinoforms. At the start of each probe, there was a five second pause. Likewise, at the point closest to the cell, the stage or moving HOT paused for five seconds before retreating backwards through the cell coat along the same line of entry.

B.4.2 Standard OT-stage versus translating HOT measurements

Figure B.4a shows a particle's dynamics as it is pushed into the cell coat in by the OT-stage setup at $v_{stage} \sim 8.3$ μm/s. While the OT position remains fixed, the particle's displacement from the trap's equilibrium position grows. For comparison, Figure B.4b shows a particle's dynamics while moving through the same cell coat as it is carried by a discrete translating HOT taking 500nm steps with 0.07s between kinoforms, which gives $v_{app} \sim 7.1$ μm/s, $v_{transit} \sim 20.9$ μm/s. The upper curve indicates the position of the bead in solution without the cell coat. The lower curve indicates the position versus time of the bead as it is carried into the cell coat. Unlike the Stokes drag measurement, a distinct difference between the two curves is observed with a growing gap between the plateaus that is consistent with increased displacement with position in the cell coat. Having noted this growing gap, it is interesting to ask what kind of force information is encoded

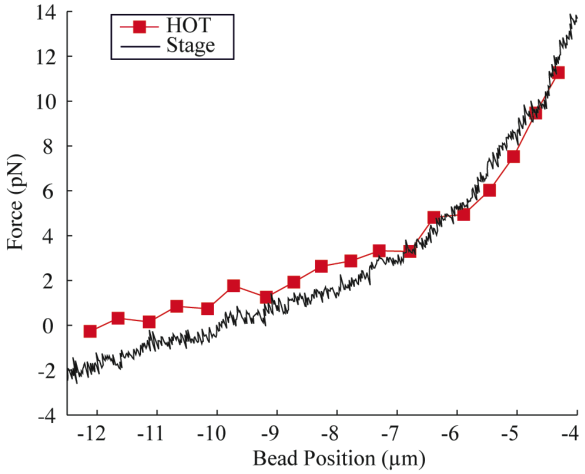

Figure B.6 Comparison of force curves produced by successive probes of a cell coat, first with a fixed OT-stage experiment followed by a measurement conducted with a translating HOT. The force data was calculated using the particle dynamics data shown in Figure B.4.

in the displacement from the center of the trap. It is not obvious that the extracted forces will agree with the force curve obtained by the OT-stage experiment, since the HOT measurement may only be sensitive to elastic but not viscous forces. Further, measurements of the cell coat are performed in non-equilibrium as reflected by the clear relaxation in the measured force in the OT-stage experiments. In attempting to imitate an OT-stage force measurement with a translating HOT, one must consider whether at the instant and position a force is measured, a comparable amount of relaxation has taken place.

Comparison of the force data generated by the two unique approaches is shown in Figure B.6. The solid line represents the standard measurement made with the stage. The two measurements overlap surprisingly well. Their slight deviation from one another in the outliers of the cell coat most likely arises from the 'tethering' of the probe particle to the cell coat. A similar variation between two consecutive force curves gathered from the same coat is evident in the 250nm step data shown in Figure B.7b. Although we passivated the particles with PEG to prevent them from sticking to the cell coat, tethering to a point near the edge of the cell coat almost always occurs. In a second series of experiments, we investigated how the dynamics of the particle motion during the HOT experiment influences the measured force curve. The discrete step size was reduced from 500nm to 250nm, while the time between kinoform updates (0.07s) remained fixed, resulting in estimated speeds of $v_{app} \sim 3.57$ μm/s and $v_{transit} \sim 10.4$ μm /s. The data are shown in Figure B.7. Despite the reduction in speed by a factor of two, the final force curves extracted from multiple probes of the same cell coat (stage, 250nm, and 500nm steps) are again very similar to one another. The result was reproducible, in five different measurements on five different cells.

To consider whether the surprising agreement of these three measurements is fortuitous, we examine the non-trivial process of generating a HOT force curve from the particle dynamics in the viscoelastic cell coat. In a purely elastic material, the final particle displacement in a given HOT is fixed once the average HOT intensity is constant. In the cell coat, the particle displacement is non-constant, relaxing with time. This leads to a quasi-plateau rather than a plateau in the particle's position at each HOT. How to self-consistently extract a well-defined force at each HOT position is not clear. A further complication arises from the spatial variation in the coat stiffness. The coat's increasing resistance to particle translation results in a decreasing transit speed, as well as a decrease in the duration of the quasi-plateaus. As a result, it is questionable whether the force measured at each HOT can be assembled into a meaningful force curve; and whether the resultant force curve can be compared with other curves generated by different means (i.e. varying step size, using a stage).

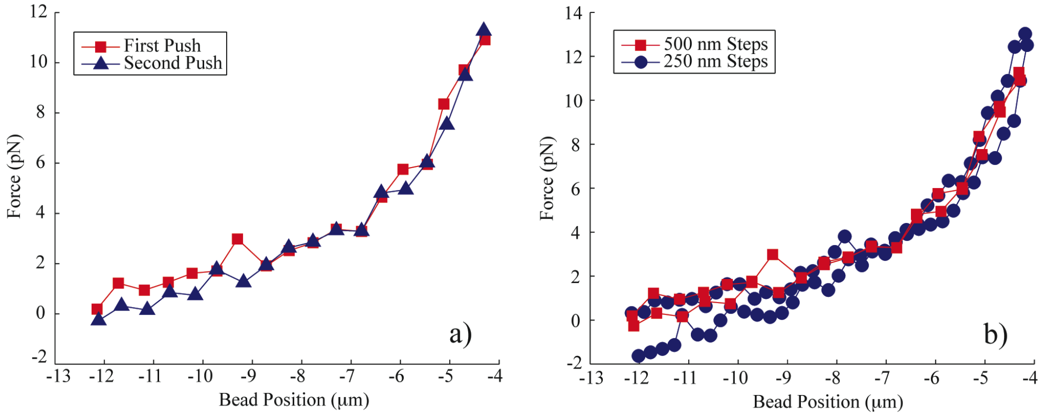

Figure B.7 (a) Repeatedly probing the cell coat with translating HOT (Δx=500nm) yields reproducible force curves. (b) Comparison of force curves generated by four successive translating HOT probes, two using Δx=500nm steps and two using Δx=250nm steps.

To generate the force curves in Figures B.6 and B.7, we employ the crudest approach, averaging over the time-dependent position of the particle. The agreement of these curves demonstrates a considerable insensitivity of the resultant force curve to (i) the estimated probe speed, (ii) spatial variations of the probe speed, and to (iii) the average estimate of the particle displacement, which ignores the relaxation of the coat. A possible explanation can be found by considering the relaxation dynamics of the cell coat shown in Figure B.5c. Two relaxation processes are apparent, a slow decay in the force over a period over a period of seconds and a faster decay in the force in a period of 0.25-0.5 seconds. We hypothesize that the distinct separation of time scales for the experimental methods versus the cell coat makes the force curve agreement possible. The maximum duration of a plateau is ~0.05s and it decreases at positions closer to the cell surface, leaving little time for the coat to relax – just 10-20% of the cell coat's shortest relaxation time. Relative to any relaxation dynamics in the cell coat, all three measurements are fast, suggesting that the extracted force is still close to the peak force associated with that particle probing speed.

B.5 CONCLUSIONS

In this work, we have considered what type of forces a translating HOT is capable of measuring. We have shown that in purely viscous media, Stokes drag cannot be measured with the simplest analysis approach. We have discussed how best to define the speed of a particle transported by a translating HOT since in some viscoelastic media, the probing speed will influence the measured forces. In our viscoelastic system, the pericellular coat, we found that the standard force curves generated by fixed OT-stage measurements could be reliably reproduced by translating HOT experiments with comparable estimated particle speeds. Our experiments hint that the extraction of force curves for non-equilibrium systems from translating HOT data is generally quite complex. It is unlikely that standard OT experiments will agree with translating HOT measurements, for an arbitrary viscoelastic system. However, the viscoelastic cell coat provides an example where slow relaxation dynamics makes force measurements relatively insensitive to differences in the types of measurements. These preliminary studies suggest that in at least one arena, translating HOTs can be reliably used to make force measurements on a viscoelastic, non-equilibrium system.

REFERENCES

1. Ng, L., A. J. Grodzinsky, P. Patwari, J. Sandy, A. Plaas, and C. Ortiz. 2003. Individual cartilage aggrecan macromolecules and their constituent glycosaminoglycans visualized via atomic force microscopy. J. Struct. Biol. 143:242-257.
2. Boehm, H., T. A. Mundinger, C. H. J. Boehm, V. Hagel, U. Rauch, J. P. Spatz, and J. E. Curtis. 2009. Mapping the mechanics and macromolecular organization of hyaluronan-rich cell coats. Soft Matter 5:4331-4337.
3. Evanko, S. P., M. I. Tammi, R. H. Tammi, and T. N. Wight. 2007. Hyaluronan-dependent pericellular matrix. Adv. Drug Delivery Rev. 59:1351-1365.
4. Hedman, K., M. Kurkinen, K. Alitalo, A. Vaheri, S. Johansson, and M. Höök. 1979. Isolation of the pericellular matrix of human fibroblast cultures. J. Cell Biol. 81:83-91.
5. Evanko, S. P., J. C. Angello, and T. N. Wight. 1999. Formation of hyaluronan- and versican-rich pericellular matrix Is required for proliferation and migration of vascular smooth muscle cells. Arterioscler., Thromb., Vasc. Biol. 19:1004-1013.
6. Ricciardelli, C., D. L. Russell, M. P. Ween, K. Mayne, S. Suwiwat, S. Byers, V. R. Marshall, W. D. Tilley, and D. J. Horsfall. 2007. Formation of Hyaluronan- and Versican-rich Pericellular Matrix by Prostate Cancer Cells Promotes Cell Motility. J. Biol. Chem. 282:10814-10825.
7. Cohen, M., E. Klein, B. Geiger, and L. Addadi. 2003. Organization and adhesive properties of the hyaluronan pericellular coat of chondrocytes and epithelial cells. Biophys. J. 85:1996-2005.
8. Knudson, C. B. 1993. Hyaluronan receptor-directed assembly of chondrocyte pericellular matrix. J. Cell Biol. 120:825-834.
9. Heldin, P., M. Suzuki, P. Teder, and H. Pertoft. 1995. Chondroitin sulfate proteoglycan modulates the permeability of hyaluronan-containing coats around normal human mesothelial cells. J. Cell. Physiol. 165:54-61.
10. Clarris, B. J., and J. R. E. Fraser. 1968. On the pericellular zone of some mammalian cells in vitro. Exp. Cell Res. 49:181-193.
11. Toole, B. P. 2004. Hyaluronan: from extracellular glue to pericellular cue. Nat Rev Cancer 4:528-539.
12. Hellmann, M., M. Weiss, and D. W. Heermann. 2007. Monte Carlo simulations reveal the straightening of an end-grafted flexible chain with a rigid side chain. Phys. Rev. E: Stat., Nonlinear, Soft Matter Phys. 76:021802.
13. Lee, G. M., B. Johnstone, K. Jacobson, and B. Caterson. 1993. The dynamic structure of the pericellular matrix on living cells. J. Cell Biol. 123:1899-1907.
14. Baranova, N. S., S. Attili, P. M. Wolny, and R. P. Richter. 2011. The sweet coat of living cells-from supramolecular structure and dynamics to biological function. Int. J. Mater. Res. 102:3.
15. Yamagata, M., S. Saga, M. Kato, M. Bernfield, and K. Kimata. 1993. Selective distributions of proteoglycans and their ligands in pericellular matrix of cultured

fibroblasts. Implications for their roles in cell-substratum adhesion. J. Cell Sci. 106 (Pt 1):55-65.

16. Zimmerman, E., B. Geiger, and L. Addadi. 2002. Initial stages of cell-matrix adhesion can be mediated and modulated by cell-surface hyaluronan. Biophys. J. 82:1848-1857.
17. Cohen, M., Z. Kam, L. Addadi, and B. Geiger. 2006. Dynamic study of the transition from hyaluronan- to integrin-mediated adhesion in chondrocytes. EMBO J 25:302-311.
18. Cohen, M., D. Joester, I. Sabanay, L. Addadi, and B. Geiger. 2007. Hyaluronan in the pericellular coat: an additional layer of complexity in early cell adhesion events. Soft Matter 3:327-332.
19. Tammi, R., and M. Tammi. 1991. Correlations between hyaluronan and epidermal proliferation as studied by [3H]glucosamine and [3H]thymidine incorporations and staining of hyaluronan on mitotic keratinocytes. Exp. Cell Res. 195:524-527.
20. Itano, N., F. Atsumi, T. Sawai, Y. Yamada, O. Miyaishi, T. Senga, M. Hamaguchi, and K. Kimata. 2002. Abnormal accumulation of hyaluronan matrix diminishes contact inhibition of cell growth and promotes cell migration. Proc. Natl. Acad. Sci. USA 99:3609-3614.
21. Toole, B. P. 1997. Hyaluronan in morphogenesis. Journal of Internal Medicine 242:35-40.
22. Chen, W. Y. J., and G. Abatangelo. 1999. Functions of hyaluronan in wound repair. Wound Repair Regen. 7:79-89.
23. Savani, R. C., C. Wang, B. Yang, S. Zhang, M. G. Kinsella, T. N. Wight, R. Stern, D. M. Nance, and E. A. Turley. 1995. Migration of bovine aortic smooth muscle cells after wounding injury. The role of hyaluronan and RHAMM. J. Clin. Invest. 95:1158-1168.
24. Han, Y., S. C. Cowin, M. B. Schaffler, and S. Weinbaum. 2004. Mechanotransduction and strain amplification in osteocyte cell processes. Proc. Natl. Acad. Sci. USA 101:16689-16694.
25. Vincent, T. L., C. J. McLean, L. E. Full, D. Peston, and J. Saklatvala. 2007. FGF-2 is bound to perlecan in the pericellular matrix of articular cartilage, where it acts as a chondrocyte mechanotransducer. Osteoarthr. Cartilage 15:752-763.
26. Clarris, B. J., J. R. Fraser, and S. Rodda. 1974. Effect of cell-bound hyaluronic acid on infectivity of Newcastle disease virus for human synovial cells in vitro. Ann. Rheum. Dis. 33:240-242.
27. Macri, L., D. Silverstein, and R. A. F. Clark. 2007. Growth factor binding to the pericellular matrix and its importance in tissue engineering. Adv. Drug Delivery Rev. 59:1366-1381.
28. Alexopoulos, L. G., G. M. Williams, M. L. Upton, L. A. Setton, and F. Guilak. 2005. Osteoarthritic changes in the biphasic mechanical properties of the chondrocyte pericellular matrix in articular cartilage. J. Biomech. 38:509-517.
29. Itano, N., T. Sawai, O. Miyaishi, and K. Kimata. 1999. Relationship between Hyaluronan Production and Metastatic Potential of Mouse Mammary Carcinoma Cells. Cancer Res. 59:2499-2504.
30. Simpson, M. A., C. M. Wilson, L. T. Furcht, A. P. Spicer, T. R. Oegema, and J. B. McCarthy. 2002. Manipulation of hyaluronan synthase expression in prostate

adenocarcinoma cells alters pericellular matrix retention and adhesion to bone marrow endothelial cells. J. Biol. Chem. 277:10050-10057.

31. Hayen, W., M. Goebeler, S. Kumar, R. Riessen, and V. Nehls. 1999. Hyaluronan stimulates tumor cell migration by modulating the fibrin fiber architecture. J. Cell Sci. 112:2241-2251.
32. Zhang, L., C. B. Underhill, and L. Chen. 1995. Hyaluronan on the surface of tumor cells Is correlated with metastatic behavior. Cancer Res. 55:428-433.
33. Zhou, R., H. Zhou, B. Xiong, Y. He, and E. S. Yeung. 2012. Pericellular matrix enhances retention and cellular uptake of nanoparticles. J. Am. Chem. Soc. 134:13404-13409.
34. Turley, E. A., and J. Torrance. 1985. Localization of hyaluronate and hyaluronate-binding protein on motile and non-motile fibroblasts. Exp. Cell Res. 161:17-28.
35. Brecht, M., U. Mayer, E. Schlosser, and P. Prehm. 1986. Increased hyaluronate synthesis is required for fibroblast detachment and mitosis. Biochem J 239:445-450.
36. Horwitz, A. R., and J. T. Parsons. 1999. Cell migration-movin' on. Science 286:1102-1103.
37. Bader, D. L., T. Ohashi, M. M. Knight, D. A. Lee, and M. Sato. 2002. Deformation properties of articular chondrocytes: a critique of three separate techniques. Biorheology 39:69-78.
38. Alexopoulos, L. G., L. A. Setton, and F. Guilak. 2005. The biomechanical role of the chondrocyte pericellular matrix in articular cartilage. Acta Biomater. 1:317-325.
39. Nijenhuis, N., D. Mizuno, J. A. E. Spaan, and C. F. Schmidt. 2012. High-resolution microrheology in the pericellular matrix of prostate cancer cells. J. R. Soc. Interface.
40. Ng, L., H.-H. Hung, A. Sprunt, S. Chubinskaya, C. Ortiz, and A. Grodzinsky. 2007. Nanomechanical properties of individual chondrocytes and their developing growth factor-stimulated pericellular matrix. J. Biomech. 40:1011-1023.
41. IyerS, R. M. Gaikwad, V. Subba Rao, C. D. Woodworth, and I. Sokolov. 2009. Atomic force microscopy detects differences in the surface brush of normal and cancerous cells. Nature Nanotech. 4:389-393.
42. Attili, S., and R. P. Richter. 2012. Combining colloidal probe atomic force and reflection interference contrast microscopy to study the compressive mechanics of hyaluronan brushes. Langmuir 28:3206-3216.
43. Baranova, N. S., E. Nilebäck, F. M. Haller, D. C. Briggs, S. Svedhem, A. J. Day, and R. P. Richter. 2011. The Inflammation-associated Protein TSG-6 Cross-links Hyaluronan via Hyaluronan-induced TSG-6 Oligomers. J. Biol. Chem. 286:25675-25686.
44. Freeman, P. M., R. N. Natarajan, J. H. Kimura, and T. P. Andriacchi. 1994. Chondrocyte cells respond mechanically to compressive loads. J. Orth. Res. 12:311-320.
45. Knight, M. M., S. A. Ghori, D. A. Lee, and D. L. Bader. 1998. Measurement of the deformation of isolated chondrocytes in agarose subjected to cyclic compression. Medical Engineering & Physics 20:684-688.

46. Trickey, W. R., F. P. T. Baaijens, T. A. Laursen, L. G. Alexopoulos, and F. Guilak. 2006. Determination of the Poisson's ratio of the cell: recovery properties of chondrocytes after release from complete micropipette aspiration. J. Biomech. 39:78-87.
47. Darling, E. M., R. E. Wilusz, M. P. Bolognesi, S. Zauscher, and F. Guilak. 2010. Spatial Mapping of the Biomechanical Properties of the Pericellular Matrix of Articular Cartilage Measured In Situ via Atomic Force Microscopy. Biophys. J. 98:2848-2856.
48. Choi, J. B., I. Youn, L. Cao, H. A. Leddy, C. L. Gilchrist, L. A. Setton, and F. Guilak. 2007. Zonal changes in the three-dimensional morphology of the chondron under compression: The relationship among cellular, pericellular, and extracellular deformation in articular cartilage. J. Biomech. 40:2596-2603.
49. Zhang, H., S. L. Baader, M. Sixt, J. Kappler, and U. Rauch. 2004. Neurocan–GFP fusion protein. J. Histochem. Cytochem. 52:915-922.
50. Scrimgeour, J., J. K. Cho, V. Breedveld, and J. Curtis. 2011. Microfluidic dialysis cell for characterization of macromolecule interactions. Soft Matter 7:4762-4767.
51. Ashkin, A., J. M. Dziedzic, J. E. Bjorkholm, and S. Chu. 1986. Observation of a single-beam gradient force optical trap for dielectric particles. Opt. Lett. 11:288-290.
52. Neuman, K. C., and S. M. Block. 2004. Optical trapping. Rev. Sci. Instrum. 75:2787-2809.
53. Crocker, J. C., and D. G. Grier. 1996. Methods of digital video microscopy for colloidal studies. J. Colloid Interface Sci. 179:298-310.
54. Polin, M., K. Ladavac, S.-H. Lee, Y. Roichman, and D. Grier. 2005. Optimized holographic optical traps. Opt. Express 13:5831-5845.
55. McLane, L. T., K. M. Carroll, J. Scrimgeour, M. D. Bedoya, A. Kramer, and J. E. Curtis. 2010. Force measurements with a translating holographic optical trap. K. Dholakia, and G. C. Spalding, editors. SPIE, San Diego, California, USA. 77621J-77610.
56. Dai, J., and M. P. Sheetz. 1995. Mechanical properties of neuronal growth cone membranes studied by tether formation with laser optical tweezers. Biophys. J. 68:988-996.
57. Kultti, A., K. Rilla, R. Tiihonen, A. P. Spicer, R. H. Tammi, and M. I. Tammi. 2006. Hyaluronan synthesis induces microvillus-like cell surface protrusions. J. Biol. Chem. 281:15821-15828.
58. Milner, S. T., T. A. Witten, and M. E. Cates. 1988. Theory of the grafted polymer brush. Macromolecules 21:2610-2619.
59. de Gennes, P. G. 1987. Polymers at an interface; a simplified view. Adv. Colloid Interface Sci. 27:189-209.
60. Rubinstein, M., Colby R.H. 2003. Polymer Physics. Oxford University Press, New York.
61. Potter-Perigo, S., P. Y. Johnson, S. P. Evanko, C. K. Chan, K. R. Braun, T. S. Wilkinson, L. C. Altman, and T. N. Wight. 2010. Polyinosine-polycytidylic acid stimulates versican accumulation in the extracellular matrix promoting monocyte adhesion. Am. J. Respir. Cell Mol. Biol. 43:109.

62. Simpson, R. M. L., S. Meran, D. Thomas, P. Stephens, T. Bowen, R. Steadman, and A. Phillips. 2009. Age-related changes in pericellular hyaluronan organization leads to impaired dermal fibroblast to myofibroblast differentiation. The American Journal of Pathology 175:1915-1928.
63. Kim, A. J., V. N. Manoharan, and J. C. Crocker. 2005. Swelling-Based Method for Preparing Stable, Functionalized Polymer Colloids. J. Am. Chem. Soc. 127:1592-1593.
64. Valentine, M. T., Z. E. Perlman, M. L. Gardel, J. H. Shin, P. Matsudaira, T. J. Mitchison, and D. A. Weitz. 2004. Colloid surface chemistry critically affects multiple particle tracking measurements of biomaterials. Biophys. J. 86:4004-4014.
65. Hardingham, T. E. 1979. The role of link-protein in the structure of cartilage proteoglycan aggregates. Biochem. J 177:237-247.
66. Mörgelin, M., M. Paulsson, T. E. Hardingham, D. Heinegård, and J. Engel. 1988. Cartilage proteoglycans. Assembly with hyaluronate and link protein as studied by electron microscopy. Biochem. J 253:175-185.
67. Franzén, A., S. Björnsson, and D. Heinegård. 1981. Cartilage proteoglycan aggregate formation. Role of link protein. Biochem. J 197:669-674.
68. Shi, S., S. Grothe, Y. Zhang, M. D. O'Connor-McCourt, A. R. Poole, P. J. Roughley, and J. S. Mort. 2004. Link Protein Has Greater Affinity for Versican than Aggrecan. J. Biol. Chem. 279:12060-12066.
69. Oshannessy, D. J., M. Brighamburke, K. K. Soneson, P. Hensley, and I. Brooks. 1993. Determination of Rate and Equilibrium Binding Constants for Macromolecular Interactions Using Surface Plasmon Resonance: Use of Nonlinear Least Squares Analysis Methods. Anal. Biochem. 212:457-468.
70. Itano, N., T. Sawai, M. Yoshida, P. Lenas, Y. Yamada, M. Imagawa, T. Shinomura, M. Hamaguchi, Y. Yoshida, Y. Ohnuki, S. Miyauchi, A. P. Spicer, J. A. McDonald, and K. Kimata. 1999. Three Isoforms of Mammalian Hyaluronan Synthases Have Distinct Enzymatic Properties. J. Biol. Chem. 274:25085-25092.
71. Pummill, P. E., and P. L. DeAngelis. 2003. Alteration of Polysaccharide Size Distribution of a Vertebrate Hyaluronan Synthase by Mutation. J. Biol. Chem. 278:19808-19814.
72. Christine, S.-U., Y. Pernille, B.-S. Kirstine, and B. O. Lene. 2009. Variety in intracellular diffusion during the cell cycle. Phys. Bio. 6:025015.
73. Daniels, B. R., B. C. Masi, and D. Wirtz. 2006. Probing single-cell micromechanics in vivo: the microrheology of C. elegans developing embryos. Biophys. J. 90:4712-4719.
74. Deng, L., X. Trepat, J. P. Butler, E. Millet, K. G. Morgan, D. A. Weitz, and J. J. Fredberg. 2006. Fast and slow dynamics of the cytoskeleton. Nat. Mater. 5:636-640.
75. Lau, A. W. C., B. D. Hoffman, A. Davies, J. C. Crocker, and T. C. Lubensky. 2003. Microrheology, stress fluctuations, and active behavior of living cells. Phys. Rev. Lett. 91:198101.
76. Wei, M.-T., A. Zaorski, H. C. Yalcin, J. Wang, M. Hallow, S. N. Ghadiali, A. Chiou, and H. D. Ou-Yang. 2008. A comparative study of living cell

micromechanical properties by oscillatory optical tweezers. Opt. Express 16:8594-8603.

77. Ashkin, A., J. M. Dziedzic, J. E. Bjorkholm, and S. Chu. 1986. Observation of a Single-Beam Gradient Force Optical Trap for Dielectric Particles. Opt. Lett. 11:288-290.
78. Lang, M. J., and S. M. Block. 2003. Resource Letter: LBOT-1: Laser-based optical tweezers. American Journal of Physics 71:201-215.
79. Grier, D. G. 2003. A Revolution in Optical Manipulation. Nature 424:810-816.
80. Svoboda, K., and S. M. Block. 1994. Biological applications of optical forces. Annu. Rev. Biophys. Biomolec. Struct. 23:247-285.
81. Hénon, S., G. Lenormand, A. Richert, and F. Gallet. 1999. A New Determination of the Shear Modulus of the Human Erythrocyte Membrane Using Optical Tweezers. 76:1145-1151.
82. Dai, J., and M. P. Sheetz. 1995. Mechanical properties of neuronal growth cone membranes studied by tether formation with laser optical tweezers. 68:988-996.
83. Kellermayer, M. S. Z., S. B. Smith, H. L. Granzier, and C. Bustamante. 1997. Folding-Unfolding Transitions in Single Titin Molecules Characterized with Laser Tweezers. Science 276:1112-1116.
84. Liesener, J., M. Reicherter, T. Haist, and H. J. Tiziani. 2000. Multi-Functional Optical Tweezers Using Computer-Generated Holograms. Opt. Commun. 185:77-82.
85. Curtis, J. E., B. A. Koss, and D. G. Grier. 2002. Dynamic holographic optical tweezers. Optics Communications 207:169-175.
86. Merenda, F., J. Rohner, J.-M. Fournier, and R.-P. Salathé. 2007. Miniaturized high-NA focusing-mirror multiple optical tweezers. Opt. Express 15:6075-6086.
87. Schmitz, C., J. Spatz, and J. Curtis. 2005. High-precision steering of multiple holographic optical traps. Opt. Express 13:8678-8685.
88. van der Horst, A., B. P. B. Downing, and N. R. Forde. 2009. Position and intensity modulations in holographic optical traps created by a liquid crystal spatial light modulator.
89. Agarwal, R., K. Ladavac, Y. Roichman, G. Yu, C. Lieber, and D. Grier. 2005. Manipulation and assembly of nanowires with holographic optical traps. Opt. Express 13:8906-8912.
90. Graham, G., and et al. 2008. Holographic assembly workstation for optical manipulation. Journal of Optics A: Pure and Applied Optics 10:044009.
91. Kress, H., J.-G. Park, C. O. Mejean, J. D. Forster, J. Park, S. S. Walse, Y. Zhang, D. Wu, O. D. Weiner, T. M. Fahmy, and E. R. Dufresne. 2009. Cell stimulation with optically manipulated microsources. Nat Meth 6:905-909.
92. Akselrod, G. M., W. Timp, U. Mirsaidov, Q. Zhao, C. Li, R. Timp, K. Timp, P. Matsudaira, and G. Timp. 2006. Laser-Guided Assembly of Heterotypic Three-Dimensional Living Cell Microarrays. 91:3465-3473.
93. Curtis, J. E., and D. G. Grier. 2003. Modulated optical vortices. Opt. Lett. 28:872-874.
94. Thoumine, O., P. Kocian, A. Kottelat, and J.-J. Meister. 2000. Short-term binding of fibroblasts to fibronectin: optical tweezers experiments and probabilistic analysis. European Biophysics Journal 29:398-408.

95. Yu-Long, S., L. Zong-Ping, F. Andrzej, and A. Kai-Nan. 2004. Stretching type II collagen with optical tweezers. Journal of biomechanics 37:1665-1669.

96. Bustamante, C., Z. Bryant, and S. B. Smith. 2003. Ten years of tension: single-molecule DNA mechanics. Nature 421:423-427.

97. Bennink, M. L., S. H. Leuba, G. H. Leno, J. Zlatanova, B. G. de Grooth, and J. Greve. 2001. Unfolding individual nucleosomes by stretching single chromatin fibers with optical tweezers. Nat Struct Mol Biol 8:606-610.

98. Qian, F., S. Ermilov, D. Murdock, W. E. Brownell, and B. Anvari. 2004. Combining optical tweezers and patch clamp for studies of cell membrane electromechanics. Review of Scientific Instruments 75:2937-2942.

99. Dao, M., C. T. Lim, and S. Suresh. Mechanics of the human red blood cell deformed by optical tweezers. Journal of the Mechanics and Physics of Solids 51:2259-2280.

100. Kress, H., E. H. Stelzer, D. Holzer, F. Buss, G. Griffiths, and A. Rohrbach. 2007. Filopodia act as phagocytic tentacles and pull with discrete steps and a load-dependent velocity. Proc. Natl. Acad. Sci. USA 104:11633-11638.

101. Mejean, C. O., A. W. Schaefer, E. A. Millman, P. Forscher, and E. R. Dufresne. 2009. Multiplexed force measurements on live cells with holographic optical tweezers. Opt. Express 17:6209-6217.

102. Allioux-Guérin, M., D. Icard-Arcizet, C. Durieux, S. Hénon, F. Gallet, J.-C. Mevel, M.-J. Masse, M. Tramier, and M. Coppey-Moisan. 2009. Spatiotemporal Analysis of Cell Response to a Rigidity Gradient: A Quantitative Study Using Multiple Optical Tweezers. 96:238-247.

103. van der Horst, A., and N. R. Forde. 2008. Calibration of dynamic holographic optical tweezers for force measurements on biomaterials. Opt Express 16:20987-21003.

104. Farre, A., A. van der Horst, G. A. Blab, B. P. Downing, and N. R. Forde. 2010. Stretching single DNA molecules to demonstrate high-force capabilities of holographic optical tweezers. J Biophotonics 3:224-233.

105. Astumian, R. D. 2007. Equilibrium theory for a particle pulled by a moving optical trap. The Journal of Chemical Physics 126:111102-111104.

VITA

Louis was born in 1983 to Martha and Kevin McLane in Austin, Texas. After spending his early years in Texas, his family moved to the greener pastures of Maryland where he graduated from Severna Park High School. In 2006 Louis received a B.S. in Physics from Bucknell University in Lewisburg, Pennslyvania. He then traveled to Georgia Tech to pursue a doctorate in Physics, landing in Jennifer Curtis' biophysics group. Aside from science, he enjoys cycling, watching movies, cooking, and spending time with his wife and dog.